UNIVERSITÀ DI PARMA

UNIVERSITA' DEGLI STUDI DI PARMA

DOTTORATO DI RICERCA IN
"SCIENZA E TECNOLOGIA DEI MATERIALI"

CICLO XXXI

Design and development of bio-hybrid multifunctional materials for regenerative medicine

Coordinatore:
Chiar.mo Prof. Enrico Dalcanale

Tutore:
Dott.ssa Monica Sandri

Dottorando: Elisabetta Campodoni

Anni 2015/2018

3. Bio-hybrid composite for dentin regeneration

4. Bio-hybrid composite for soft and hard tissue regeneration

5. Superparamagnetic hybrid nanoparticles as drug delivery system

6. Innovative bio-hybrid composites as booster for sunscreen formulations

AIM OF THE WORK

Since the beginning nature has always inspired the research. In nature are present excellent examples of efficient mechanisms and materials with impressive advantages that can represent solutions for human problems. In this contest, the bio-based polymers are receiving high interest from researchers all over the world, because advanced materials from renewable resources are becoming more and more in demand. The reason is that biomaterials play an engaging role in the field of regenerative medicine where biomimicry has today become a driving concept. The close reproduction of the physico-chemical, morphological and mechanical features of targeted tissues like bone provide biomaterials with ability to exchange information with cells and trigger, for example, the bone regenerative cascade.

Bio-inspired materials have been proposed as excellent candidates in several fields such as cosmetic field, medical devices and tissue engineering. In particular, tissue engineering emerged as a viable therapeutic solution to regenerate diseased tissues. Associated to the concept of tissue engineering, the material science was involved and aimed at designing new custom-made scaffolds, offering ideal environment for cell adhesion and migration and regulating cellular proliferation and function by providing proper biochemical signals. Scaffolds are porous, degradable structures fabricated from either natural or synthetic polymers or other many kinds of inorganic materials. The optimization of their properties to support cells and the ability to be degraded in response to matrix remodeling enzymes released by the cells is the key to the uniform regeneration of tissues.

The research activity described in this thesis is devoted to the design and development of bio-hybrid multifunctional materials addressed to regeneration of hard and soft tissues, to delivery of nano-platform loaded with drugs or to the creation of innovative product in cosmetic field. The research was mainly carried out at the Institute of Science and Technology for Ceramics, belonging to the National Research Council of Italy (ISTEC-CNR), during my Ph.D. in in Materials Science and Technology.

This PhD thesis had the aim to study natural processes and materials and mimic them to develop new bio-inspired and multifunctional materials capable to answer specific need regarding tissue engineering, nanomedicine and cosmetic. In particular, I developed four different materials that have highlighted the powerful of biomineralization process, allowing the development of multifunctional materials capable to be exploited in different fields.

The first material developed during thr PhD project was a hybrid composite for dentin regeneration. In this study by following a biomimetic approach we synthetized a hybrid composite in which the mineral phase, magnesium-doped hydroxyapatite nanoparticles (MgHA) wereare nucleated on a biopolymeric matrix (gelatin) resembling the chemico-physical features of the natural mineralized tissue.

The second material was a polymeric blend conveniently cross-linked for soft and hard tissue regeneration. In this study, blending and cross-linking processes were are designed to combine the best properties of two bio-polymers and to obtain hybrid materials with improved mechanical performances without losing biocompatibility, chemical stability and flexibility. Finally, the biomineralization process was studied too evaluate the possibility to use this material not only in soft tissue, but also in hard tissue regeneration.

The third material developed was a drug delivery nanosystems that allows to improve the drug efficacy, increasing the drug's concentration that goes to the target site and lowering the collaterals effects. In particular, magnetic hybrid nanobeads (MHNs) were composed by alginate and Fe-hydroxyapatite nanoparticles that are both biocompatible and bioresorbable.

Finally, the last material developed during PhD project was a hybrid composites used in sunscreen formulation composed of iron- and titanium-doped hydroxyapatite and gelatin (GelFeTiHA) or titanium-doped hydroxyapatite and gelatin (GelTiHA) capable together to protect by UVA and UVB ray avoiding the whitening effect and the photocatalytic effect which can damage the tissues provoking skin disease.

1. Introduction

1.1. A tool for regenerative medicine: Tissue Engineering.

Tissues can be damaged or lost due to age, losses, congenital diseases; regenerative medicine is the process in which that tissues can be repaired thank to the stimulation of previously irreparable organs.[1] Principles of engineering and life sciences are combined to enhance the comprehension of the fundamental biological mechanisms in regenerative medicine. Furthermore, in this contest the structure-function relationships in physiologic and pathologic tissues was underlined and accomplished alternatives strategies for developing substitutes which are able to restore, maintain, or improve tissue and organ function.[2,3] One of the tools for regenerative medicine is Tissue Engineering, which has the aim to regenerate, engineer and promote the restoration of tissues or organs to renew their biological function.[4,5]

Tissue Engineering designs and develops bioreactors for tissue regeneration where cells are seeded on scaffolds, 3D materials composed of different materials to promote the cell architecture; these scaffolds have to be biocompatible and functionalized to promote cell adhesion and proliferation determining the final shape and composition of tissues or organs (Figure 1.1).[5,6]

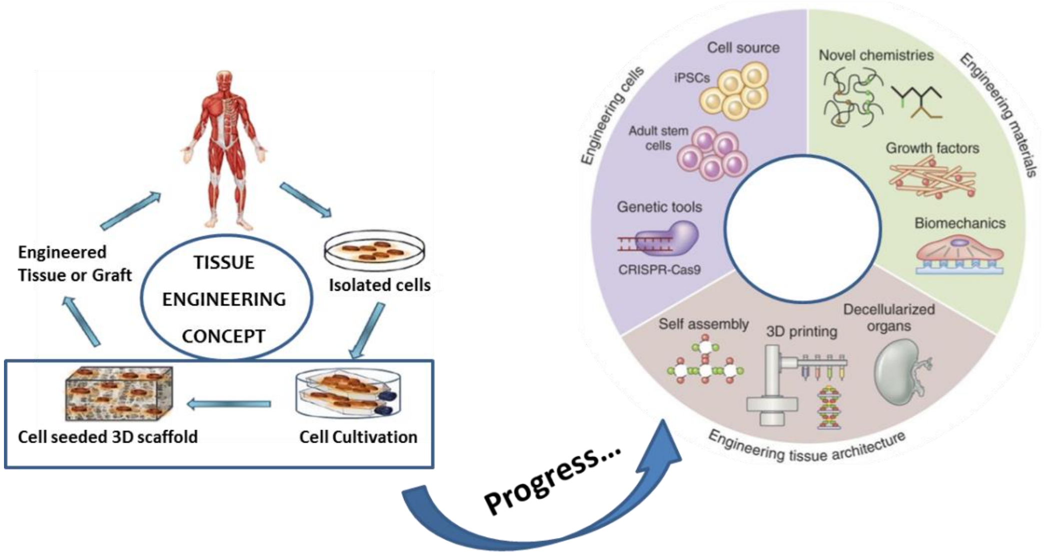

Figure 1.1. A schematic representation of Tissue Engineering concept and its progress.

In the last decade, the research has paid more attention in developing of 3D scaffold composed of biomaterials conveniently combined between them to design composites that are more efficient.[7,8]

A biomaterial was defined in 2009 as "a material that has been developed alone or as a part of complex system and it is used to instruct, by monitoring of living systems, the course of any therapeutic or diagnostic procedure in human or veterinary medicine".[9,10] The evolution of biomaterials has highlighted three different generations; in 1960s the first generation was born capable to mimic the properties of replaced tissue with very low toxic response[11]: it was defined non-toxic and inert. In 1980s , the second generation was born capable to stimulate a controlled reaction by the biological tissue.[12] In this period, resorbable materials were born able to degrade during the regenerative process letting place to newly tissue formed. Finally the third-generation was born, capable to elicit specific reactions up to molecular scale promoting cell colonization and differentiation that led to the regeneration of living tissues.[13] To stimulate specific reactions at the molecular level, it is fundamental to understand in detail and mimic tissue properties up to the nanoscale.

1.1.1. The challenge of imitating Nature

Biomimicry is the examination of nature, its models, systems, processes, and elements to emulate or take inspiration from, in order to solve human problems. The core idea is that nature has already solved many of the problems we are grappling with.[3,14,15] Animals, plants, and microbes are the consummate engineers. After billions of years of research and development, failures are fossils, and what surrounds us is the secret to survival. The newer researches take inspiration from nature always more frequently, trying to mimic complex and flawless phenomena; in particular, new synthesis methods enabling controlled crystal growth and organized structures at the multi-scale levels are attracting.[16,17] The beauty and power of nature that we want to emulate is that it creates natural structures in a slow but extremely efficient way, starting from the optimization of the microstructure according to the specific physiological function, up to develop materials with brilliant performances.[18] In 1957, Otto H. Schmitt developed a small apparatus capable to mimic the electrical action of nerve promoting the first bio-inspired process and so, introducing the term "Biophysics" on which based the "Biomimetics" and, later, it changed in "Biomimesis", "Biomimicry" and "Biological inspired design".[9]

Always in nature some solutions have been observed that maximize functionality using low energy and zero impact on environment; for this reason, biologically inspired approaches have particularly fascinated in several application..[19–21] Biomimicry has engaged several fields creating smart materials to solve those problems that nature has already solved. There are some examples of biologically inspired materials such as spider web glass to avoid the high-speed headaches of birds, in fact they recognize the spider web because it reflects ultraviolet ray and, thus, can recognize also the glass.[22] As well, gecko feet are thoroughly studied to develop biomimetic materials useful for replacing the sutures and staples in the hospital or to create gloves to scale down the wall. Geckos have the ability to scale smooth walls thanks to millions of macroscopic hairs on the bottom of their paws that are able to create a powerful grip that can be instantly broken just changing the direction of the setae composing them. [23] Those are only some examples. The use of this materials widely increased in the past fifty years, some bioinspired technologies were developed such as bone-like materials based on wood, tough ceramics based on mother-of-pearl, self-cleaning structures based on flowers, underwater glues based on mussel adhesive and drug reduction based on dermal riblet on shark skin(Figure 1.2).[24–27]

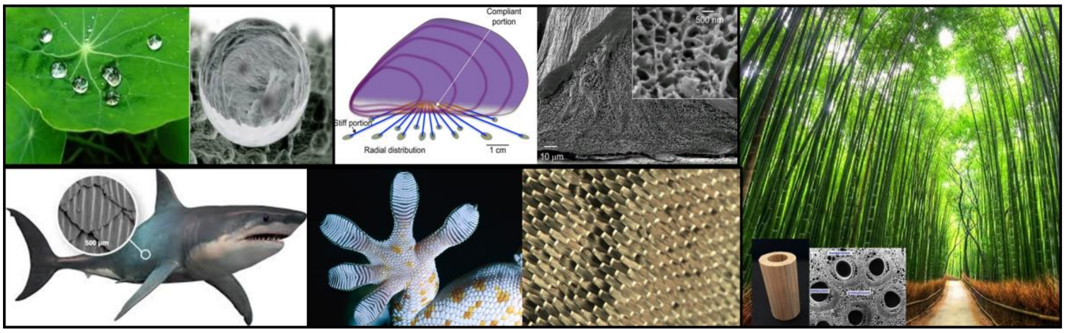

Figure 1.2. Some example where Nature inspires research.

Nevertheless, the Nature study is not limited to develop biomimetic materials, but nature is also studied to mimic natural process to create new materials.[28] In biomedical field, one of the most interesting natural process is the biomineralization process useful to create highly biocompatible materials with low environmental impact that are recognized by cells as very similar to natural bone.[29–31] Biomineralization is a natural process by which organisms form minerals and consists in a complex cascade of phenomena generating hybrid nano-structured materials hierarchically organized from the nano-scale to the macroscopic scale. This process is at the basis of load-bearing structures such as bones, shells, exoskeletons and allows designing biocomposite with unique properties, not obtainable with any conventional approach as with the information exchange with cells and the trigger of the bone regenerative cascade.

1.2. Soft and hard human tissues

In biology, a tissue is a cellular organizational level between cells and a complete organ. It can be mineralized or not. The first, called also hard tissue, is a biological tissue that incorporates minerals into soft matrix to create a protective shield or a structural support such as bone, teeth, cartilage. The non-mineralized tissue, called also soft tissue, can be connective, muscular, nervous or epithelial.[32,33] Nevertheless, Extracellular matrix (ECM), made of collagen as major, surrounds cells which compose all biological tissues. Cells are the tissue building blocks and are present in the majority of mammalian organs. A proper substratum endowed by suitable chemical and structural properties is essential for cells which can’t feel well in suspension. Their proliferation is deeply affected to the support and to the properties of the surrounding environment. Soluble and physically bound signals compose the ECM as well as signals arising from cell-cell interactions. These signaling can provoke complex intracellular signaling cascades that control gene expression and instruct tissue formation, homeostasis and regeneration.[34,35]

1.2.1. Cartilage structure

Cartilage is a specific connective tissue provided to support function. It is composed of particular cells, chondrocytes surrounded by ECM in which fibers are immersed in an amorphous and gelatinous matrix. The mineral phase is absent in cartilage as well as blood vessel and nerves thus the nutrition in cartilage happens for diffusive transport from blood vessels nearby (Figure 1.3).[36]

ECM is composed of:

- Amorphous molecules such as water (60-80% of cartilage weight), gas, small proteins, metabolites.
- Structural macromolecules (20-40% of cartilage weight):
    1. collagen (60%),
    2. proteoglycans (25-35%)
    3. glycoproteins (10-15%).

Collagen is uniformly distributed in tissues and it is responsible for the tissue shape and mechanical strength, while proteoglycans and glycoproteins are linked to collagen and promote the water uptake into the matrix. Proteoglycans are organized in complex molecular aggregates formed of glycosaminoglycans (GAGs) covalently attached to the core proteins. Glycosaminoglycans are the most abundant heteropolisaccharides in the body. They are long unbranched molecules containing repeating disaccharide units containing a derived from amino-sugar as N-Acetylglucosamine or N-Acetylgalactosamine. On the fiber core, that is composed of hyaluronic acid (disaccharide polymer constituted by glucuronic acid and N-Acetylglucosamine), are linked 100 proteoglycans, each distance of 30 nm through binding proteins. This aggregate forms the protein-based nucleus that link 80 chain of gliycosaminoglycans containing sulfate groups (chondroitin sulfate and keratin sulfate) by means of serine and threonine residues.[34,36,37] GAGs are highly negatively charged and bind a lot of calcium ions and this is essential for their function to create a gelatinous matrix promoting cell cohesion and holding high amount of water in interstitial spaces, modulating the hydration of cartilage and the capacity to absorb shock as well as compression.

There are three different cartilages:

- Hyaline cartilage
- Fibrous cartilage
- Elastic cartilage.

The hyaline cartilage is present near the articulations and responsible for their lubrication. It is found in the nose, ribs, trachea and bronchi. This cartilage has an essential biomechanics function: i) it is capable to absorb shocks despite of its low thickness, ii) it can share the loads reducing stress above the subchondral bone, iii) it minimizes the friction providing a god scrolling's surface to articulations.[38]

The articular cartilage is subdivided in three different layers: top layer, also known as lamina splendens, and middle layer are composed of organic phase, while the bottom layer, very closed to subchondral bone, is partially calcified. Trauma or degenerative diseases can damage all layers of articular cartilage and its self-repair capability is low due to a lack of blood vessel and to reduced ability of chondrocytes cells to replicate.[39]

1.2.2. Bone Structure

The structural and supporting connective tissue that is mainly present in the body is the Bone tissue, made of an organic matrix reinforced by deposits of calcium salts, forming the mineral phase. In the organic matrix several ions can be found, in particular calcium and phosphate ions are present, forming a crystalline salt called hydroxyapatite $Ca_{10}(PO_4)_6(OH)_2$.[32] Bone tissue is made of organic matrix (about 30 wt%) and hydroxyapatite (about 70 wt%). Collagen fibers principally compose the organic phase, and the residual (5-10 wt%) is ECM, that favor the nucleation and growth of mineral phase. There are two different bone types, both composed of osteon:

- A dense bone that surround the marrow space: cortical bone.
- A honeycombed trabecular plates and rods dispersed in the bone marrow compartment: trabecular bone.

The ratio between cortical an trabecular is not the same in human bone and skeleton; it depends of type of bone (vertebrae, femoral heads) or human age (e.g. adult human skeleton is 80% cortical bone and 20% trabecular bone).[40] Bone tissue is organized in a complex and hierarchic way from molecular to the macroscopic scale. At molecular level, ECM made of type I collagen fibrils surrounds cells (~300 nm long, ~1.5 nm in diameter) and along collagen fibrils nano-apatitic crystals are present (plate-shaped, 50 nm × 25 nm in size, 1.5–4 nm thick). The nano-apatitic crystals are preferentially oriented along c axis of the collagen fibrils and arranged in a periodic staggered array along the fibrils (Figure 1.3).[41,42] The material produced is firm but light and flexible, self-healing and multifunctional; it has a high fracture resistance thanks to a multitude of deformations and reinforcement mechanisms happening at many size scales, varying from the nano-structural level to the macroscopic physiological level.[40,43,44]

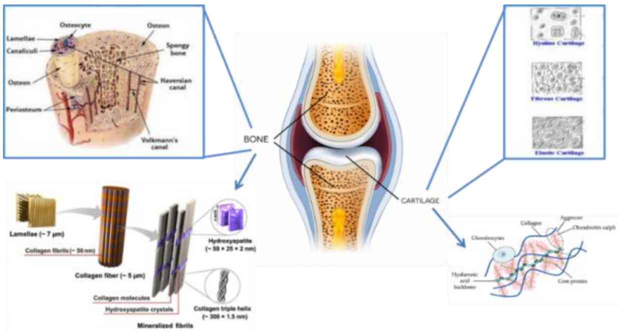

Figure 1.3. Schematic representation of bone and cartilage structures.

1.2.2.1. The role of bone cells in modeling and remodeling processes

Bone is a metabolically active tissue composed of several types of cells, acting to adapt and conserve the chemical-physical structure through a remodeling process. In the bone tissue continuously happens a self-resorbable and recontraction to reach the suitable morphology to sustain stresses change or to repair bone fracture.[45] Bone cells are divided in osteoblasts, osteocytes and osteoclasts, differentiating for the specific functions of bone formation, conservation and removal respectively. Osteoblasts and osteocytes are derived from osteoprogenitor cells, but osteoclasts are derived from the same cells that differentiate to form macrophages and monocytes.[46,47] Within the marrow of the bone there are also hematopoietic stem cells. These cells give rise to other cells, including white blood cells, red blood cells, and platelets.[45,47–49]

- Osteoblasts: they play the role to synthetize and extrude the organic matrix, collagen, suitable for the following mineralization (nucleation of mineral phase on collagen fibrils) to create the bone tissue. Osteoblasts have a cubic shape and arrange on the bone tissue surface very close between them, producing around them bone matrix that, at the end, entraps the same osteoblasts; osteoblast entrapped turned into osteocytes.
- Osteocytes: they persist in the bone matrix until the bone portion dies or degrades. They are present in bone holes, in the matrix, between two plates, with a flattened shape with thin cytoplasmic extensions. Osteocytes function is to provide nutritious substances for surrounding tissue through cytoplasmic interconnected channels called canaliculi. They cannot produce or destroy the bone tissue, but detecting mechanical stresses through cytoplasmic extensions, they can stimulate other cells to modulate the deposition or reabsorption of mineral phase.
- Osteoclasts: they are large and moving cells, endowed with more nuclei formed in bone marrow. They are able to degrade the mineralized bone tissue, isolating it in microenvironments and acidifying it until bone tissue is dissolved in the organic and inorganic matrices. Their activity is regulated by chemical signals (hormones, low calcium levels) or mechanical signals that promote the osteoclasts activity to destroy some lamellae to deposit new differently oriented lamellae to stabilize the applied stress.

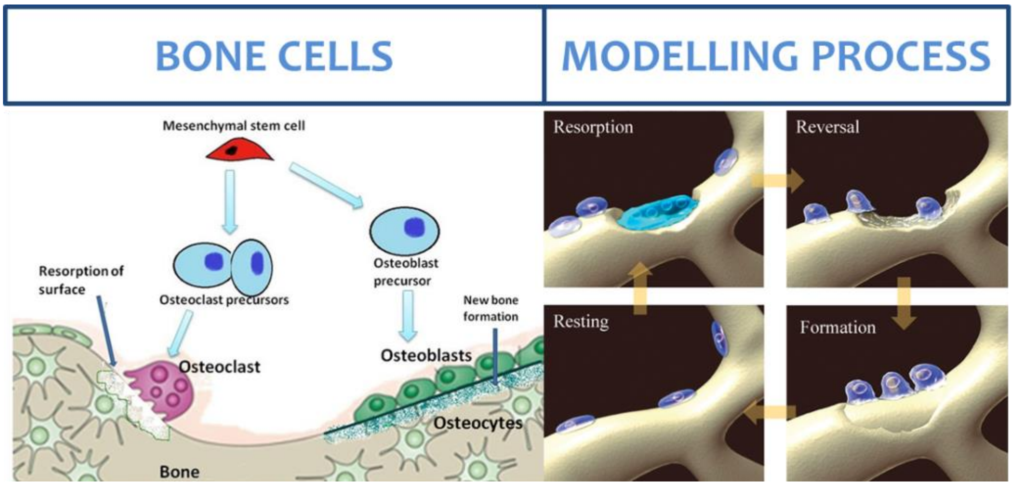

Figure 1.4. Representation of bone cells and modelling process of new bone.

In conclusion, due to the regular metabolic and structural demands, bone is defined a complex and living tissue. Processes of deposition, nutrition and reabsorption of bone tissue allow bone cells to model and remodel all characteristic of bones in term of dimension and shape in response to mechanical loading or wounding.[45,46] The complete turnover of bone tissue forming the skeleton happens about each 10 years, the younger the skeleton, the shorter the turnover. Observing a bone transverse section can be recognized three different elements: i) mature osteons where the deposition of mineral phase is concluded; ii) newly formed osteons identifiable from wide Haversian canal and osteoblast aligned on the bone surface of the Haversian canal; iii) resorption lacunas surrounded by osteoclasts. In young people there are a lot of newly formed osteon together with mature osteon and resorption lacunas because the modelling and remodelling processes are dynamic; in adults there are more mature osteons and less resorption lacunas conferring firmness to the bone. Instead, in old people, there are more resorption lacunas and few newly formed osteons, due to more resorption than deposition of mineral phase. This condition, also called osteoporosis, is characterized by a bone tissue thickness and following increase of bone brittleness and it can be due to age progress or to diseases, hormonal defects and eating disorders.[50,51]

1.2.2.2. Biomineralization process

Biomineralization refers to the processes by which organisms form minerals and consists in a complex cascade of phenomena generating hybrid nano-structured materials hierarchically organized from the nano-scale to the macroscopic scale. This process is at the basis of load-bearing structures such as bones, shells, exoskeletons.[16,52] Both inorganic and organic components play a key role in the process: the first one brings hardness and pressure resistance, essential for the existence of larger living animals, but alone it is very brittle; the second one, instead, gives elasticity and tensile strength that combined with the other characteristics bestow on biominerals amazing and fascinating properties, otherwise difficult to find in synthetic analogues.[8,18] Furthermore, since organic matrix is composed of structural macromolecules that are insoluble and serve as support and acid macromolecules that provide the functional groups needed to its interaction with inorganic component, it controls the nucleation and growth of the inorganic component in a strict manner. The organic component exerts a control on the formation of the bio-hybrid construct by multiple mechanisms: i) chemical, by coordinating the ion transport and molecular-based inhibitors and promotors; ii) spatial, as macromolecules can influence the mineral shape, size and deposition; iii) structural, by promoting the nucleation of a specific crystal face through molecular recognition at the interface; iv) morphological, promoting the assembly into a series of higher-order structures.[52,53] The nucleation phase of apatitic crystals starts in the less sense regions of the collagen fibril and they growth with c-axis elongated in parallel to the axis of collagen fibrils. After that, simultaneously in different nucleation sites, starts the growth phase (calcification phase) taking to a distribution of crystals formed in several low-density regions divided by non-mineralized regions. The increase of mineral phase is due to an increase of nucleation site and not to an increase of crystal size, because the organic phase allows to maintain the reduced crystals size. A well-mineralized collagen fibril is the result of this process representing the building block of bone tissue (Figure 1.5).[8,16,29]

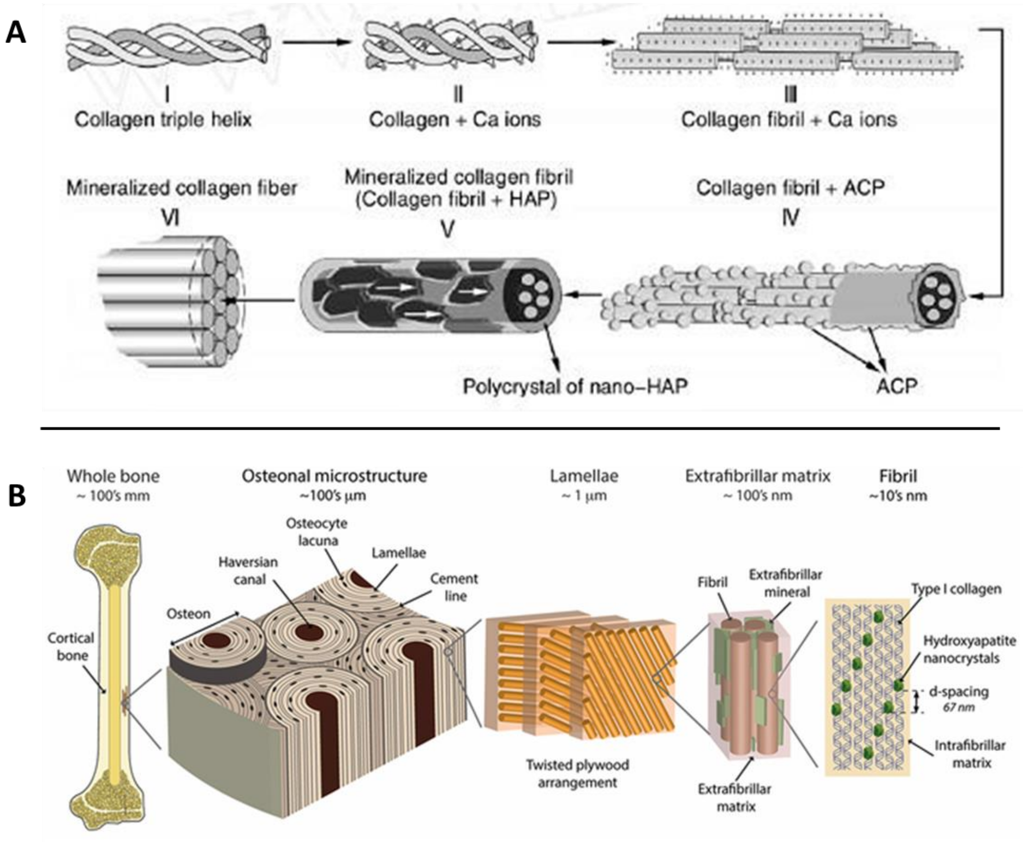

Figure 1.5. A) Mineralization of hydroxyapatite on collagen fibers, the biomineralization process forming bone; B) from macro to nano-representation of bone tissue.

Biomineralization is thus able to generate 3-D constructs with chemical, physical and structural complexity and outstanding properties giving to the Nature the capability to intelligently respond to environmental stimuli and the ability of self-renewal / self-regeneration upon limited damages.[18] Looking in detail at the biomineralization process, the functional groups of organic matrix act as sites of heterogeneous nucleation for the mineral phase through the precipitation of the ions like Ca^{2+}, PO_4^{3-}, Na^+, K^+, Mg^{2+}, that are present in the surrounding extra-cellular matrix (ECM).[54–58] Progressively, the mineral phase grows under strict physical constrains that restrict not only the crystal size but also its development along specific crystallographic directions and morphology. These features confer specific affinity for protein adhesion.[54,59] Finally, the matrix-mediated control acts at increasing scale size, thus the resulting hybrid assumes a complex architecture that is strictly dependent on the combination of the various phenomena described above. In a macroscopical view, during the biomineralization process the bone changes from soft and flexible material to a dense and tough one, with mechanical properties close to metals.[43,60,61]

1.3. Biomaterials for tissue engineering

A biomaterial is a material that has been designed to interact with biological systems for a medical purpose, either a therapeutic (heal, increase, repair or substitute a tissue function of the body) or a diagnostic one.[11,13,34] The efficacy of a biomaterial depends on its ability to create a response of biological systems. For this reason, any material implanted in tissues results inert because it stimulates a reaction by tissues. In particular, four different reactions can be obtained:

1. A toxic material produces the death of the tissue.
2. A non-toxic material and biologically inert produces a fibrous tissue with variable thickness.
3. A non-toxic material and biologically active produces a bond in the interface tissue-material.
4. A non-toxic material and bioresorbable produces, in time, a substitution of material with newly tissue formed.

Saving first material, the other three are all biocompatible meaning that materials is capable to provoke a positive reaction in a biological system when interacts with it, and it is able to support its function during all material life. Furthermore, a bio-inert material means that no reactions are provoked with tissues being in contact. Nowadays, the most interesting material is a bioresorbable material that is designed to stimulate regeneration reactions producing the formation of new tissue and to gradually degrade while new tissue is formed and substitutes the material. This material is the ideal solution only if it is endowed with the hardness and mechanical strength required.[62] The critical point in this material design is to create a stable tissue-material interface during tissue regeneration and modulate the degradation rate with tissue formation to maintain intact the biomaterial during the regeneration process. The ideal material is also bioactive because stimulate a specific biological response producing a bond between material and tissue. In particular, bioactive ceramics are capable to nucleate the organic matrix in bone tissue, generating a chemical bond between tissue and material without the presence of fibrous tissue.[8] Some materials are bioactive such as bio-glass, calcium phosphates and composites between hydroxyapatite and glass or polymers. A bioactive material can stimulate two different responses because it can be an osteoconductive or osteoinductive material. An osteoconductive material is able to be colonized by the host tissue cells before implant and after it promotes the bone formation thanks to cells colonizing material and the ions required for mineralization. However, an osteconductive material is not able to induce a cell differentiation. This capability is instead typical of an osteoinductive material, which is able to recruit immature cells and stimulate them to differentiate in osteoblasts promoting, bone formation.[63] However, the mechanical properties of these materials are lower than natural bone. They are not exploited as structural materials but as fillers or superficial materials deposited on other bio-inert materials to guide the bone regeneration processes. In conclusion, to design a material suitable for bone regeneration, some characteristics are taken into account, such as the biocompatibility, bioactivity, bioresorbability and the biodegradation rate. For this reason, materials that satisfy these parameters without being endowed with good mechanical performance can be considered for the tissue regeneration.[8,64]

The process of tissue regeneration consists in the following step:

1. restoration of the structure;
2. restoration of the function;
3. restoration of the metabolic and biochemical functions;
4. restoration of biomechanics performances.

1.3.1. Natural polymers

Polymer from natural sources can be exploiting in tissue engineering due to its biomimesis and this have to be an excellent challenge for global industries in order to promote a green chemistry and the innovation. Bio-based polymers can be produced from renewable biogenic resources and represent excellent candidates for their low cost, biocompatibility, biodegradability and eco-sustainability often difficult to obtain in laboratory. The US Congress in the Farm Security and Rural Investment Act defines "bio-based products as commercial or industrial products that are composed, in whole or in a significant part, of biological products or renewable domestic agricultural materials (including plant, animal, and marine materials) or forestry materials in 2002".[65,66] Furthermore, another important feature of this kind of materials is the capability to be modified by physical, chemical or enzymatic methods to create new application of materials and meet specific industrial applications.[67,68]

Bio-polymers could be originated from several resources:

- From microorganisms' fermentation (like polyhydroxyalkanoate, bacterial cellulose, etc.);
- from bio-derived monomers (i.e. polylactic acid);
- from plant (Alginate) and animals (Collagen, Gelatin);
- from biomasses producing oils (soybeans, corn and wheat oil) and polysaccharides (Starch and cellulose).

Collagen is a fibrous structural protein and it is the main structural protein in the extracellular space in the various connective tissues in animal bodies. Collagen consists of amino acids wound together to form triple-helices, which form elongated fibrils and occurs in many places throughout the body. There are 10 different types of Collagen in animal body (Table 1.1); all of them own triple-helix, but they have different length of helix and no-helicoid portions; however, over 90% of the collagen in the human body is type I, that is present in tendon and bone tissues.[69]

Table 1.1 List of different Collagen type and their distribution.

Type	Class	Distribution
I	Fibrillar	Dermis, bone, tendon
II	Fibrillar	Cartilage, vitreous
III	Fibrillar	Blood vessels
IV	Network	Basement membranes
V	Fibrillar	Dermis, bone, tendon
VI	Filaments, 100 nm	Dermis, bone, tendon
VII	Fibers with antiparallel dimers	Dermis, bladder
VIII	Hexagonal matrix	Membrane
IX	Fibrils-associated collagens with interrupted triple helices	Cartilage, vitreous
X	Hexagonal matrix	Cartilage
XI	Fibrillar	Cartilage
XII	Fibril-associated collagens with interrupted triple helices	Tendon

Collagen molecule consists in three polypeptides chains arranged in a helix, where the Gly-X-Y amino acidic unit are repeated and in X and Y often are present proline and hydroxyproline, that confer stiffness at the molecule. Amino acids are linked between them through peptide bond, specific bond between amino and carboxylic functional groups. This is partially a double bond that constrains the mobility of the chain and together with inter-chain hydrogen bonds and other interactions between residues confer stability to the α-helix collagen structure (Figure 1.6).[70,71]

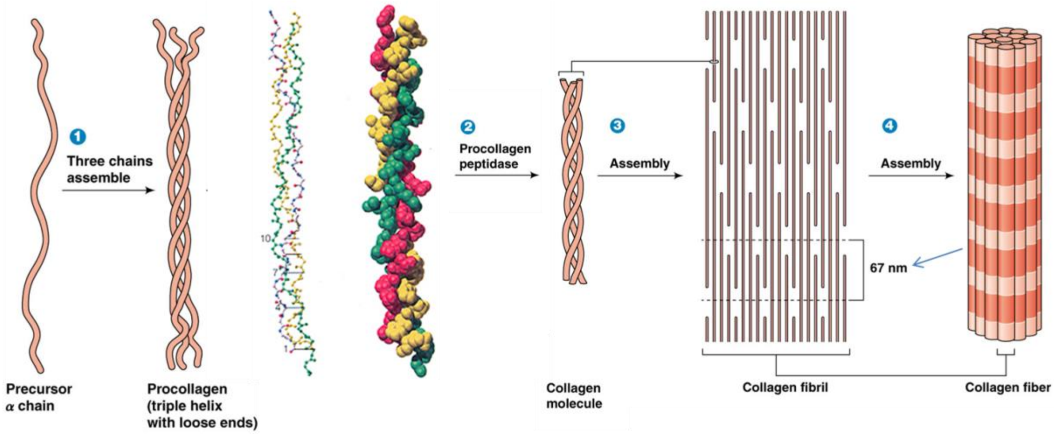

Figure 1.6. Assembling and final structure of Collagen fibers.

In the type I collagen, two chain have same composition of 1056 residues, while the last chain is made of 1038 different residues. Only 1014 residues for each chain is involved in the triple-helix structure. The amino acid remaining without helicoid configuration are called telopeptides. A collagen microfibril is composed of the repetition of triple-helix structure and the repetition of microfibrils form the fibrils in which microfibrils are separated by 1.3 nm. This distance allows to create more or less dense zone detectable at the microscope. Finally, the aggregation of fibrils forms the collagen fibers.[69] Collagen isn’t a hydro-soluble protein thanks to its specific 3D structure. Amino acids presented in collagen owning amino (-NH2), carboxylic (-COOH) and hydroxyl (-OH) functional groups together with peptide bond represent the active site of molecule for chemical interaction. Due to its specific amino acid composition, the isoelectric point (pI) of collagen is 5.5, pH in which the net electrical charge of amino acid is zero and the precipitation of fibres is shown.[72,73] According to biomimetic processes, collagen is the ideal material for tissue regeneration, however, the use of animal-derived collagen could present some limitations regarding its quality and purity, the possibility of immunological reactions that influence the final properties and applications. For this reasons, scientists have also tested various different macromolecules like cellulose, chitosan, gelatin, alginate, fibroin coming from natural sources.[62,74]

Gelatin derives from denaturation of collagen and retains chemical features similar to collagen and excellent bio-compatibility. There are two different type of gelatin: Type A, deriving from collagen of pig skin by acid pretreatment and Type B, deriving from collagen of beef hides or bone by an alkaline process.[75] Amino acid composition of gelatin depend on raw materials and treatment, however, the major components are glycine, proline and lysine. Gelatin is widely used in foods, cosmetics, pharmaceuticals and medical fields thanks to its exceptional characteristics like biocompatibility and biodegradability, allowing the creation of a suitable environment for the cells.[76,77] Gelatin naturally forms reversible gel when temperature slows under gelation transition temperature of 30ºC, below this temperature molecules change the conformation from random coil to triple helix (Figure 1.7). This aggregation is reversible if the temperature is increased, but, gel can be made irreversible using a cross-linking agent which block the conformation creating bridges between gelatin molecules.[78,79]

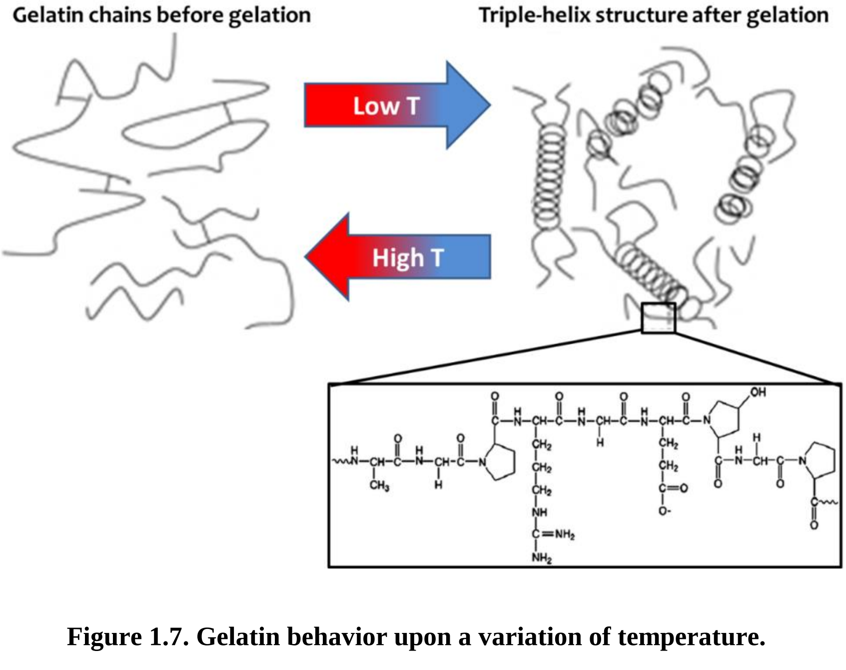

Figure 1.7. Gelatin behavior upon a variation of temperature.

Alginates, as well, are a family of linear binary co-polymers extracted from marine brown algae and their plant-derived source provides a micro-environment very close to extracellular envoronment.[80] Polymers composing alginate are D-mannuronate (M) and

L-guluronate (G) covalently linked through –β 1,4 and –α 1.4 glycosidic bond in different way, exactly, monomers can appear in homopolymeric blocks of consecutive G-blocks, consecutive M-blocks or alternating M and G-blocks. The different ratio between G and M defines different alginate. [81] The sodium-salt alginate is soluble in water and form a solution similar to a hydrogel that, in presence of bivalent ions, link the L-guluronate residue forming insoluble hydrogel through an egg-box model (Figure 1.8).[82]

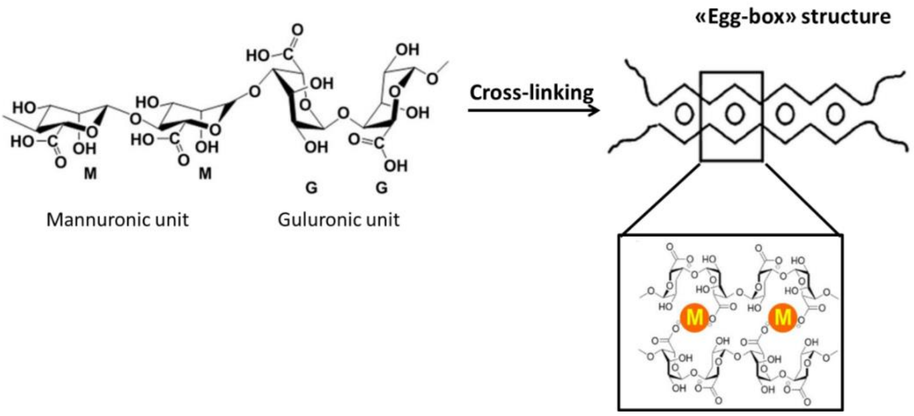

Figure 1.8. Alginate's structure before and after cross-linking.

Chitosan derives from the partial deacetylation of chitin that is the structural element of crustoceans' exoskeleton. It is a cationic polymer endowed by biocompatibility and biodegradability. Chitosan is a polysaccharide composed of randomly distributed β-(1-4)-linked D-glucosamine (deacetylated unit) and N- acetyl-D-glucosamine (acetylated unit) (Figure 1.9).[83,84] Chitosan has been used in the agricultural, industrial and biomedical application for wound healing and bone induction, drug and gene delivery and in scaffolds for cell growth and encapsulation. Chitosan is safe, hemostatic, osteoconductive and it has an antimicrobial activity and a structure very sensitive to change of pH due to amino groups that are deprotonated above the pH range of 6.2-7. Although insoluble in water, below pH of 6.2 chitosan is dissolved (e.g. Acetic acid) making the amino- and hydroxyl groups of chitosan available for cross-linking.[85,86]

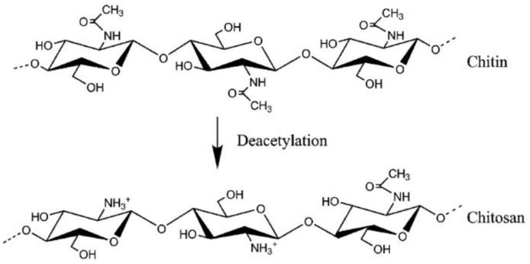

Figure 1.9. Structure of Chitosan.

Cellulose is the most widespread polymeric material in nature. It is biocompatible, low-cost and exhibits good mechanical performance. Nanocellulose is its subset with nanometric size that can be extracted from cellulose by various physical/chemical/enzymatic approaches to isolate the fibrils from plants (NFC and NCC) and the bottom-up production from glucose by bacteria (BC). [87,88] Nanocelluloses have many advantageous properties, such as the high strength and the ability to self-assembly, useful for various purposes, e.g. nanocomposites, thin films with high strength and barrier against oxygen and with added functionality such as antimicrobial activity. During the last years, breakthroughs in the production of nanocellulose have been achieved and production of cellulose nanofibrils varying in fibril diameter and with neutral, polyanionic and polycationic surfaces are enabled. The properties on molecular, nano- and microscale will influence the properties of the nanocellulose and the final products.[89,90] Furthermore, nanocellulose displays self-assembling ability by establishing weak or strong hydrogen bonds and offers the possibility to chemically or physically modify its functional groups. The possibility to functionalize its surface bestow it the possibility to be customized, exploiting it like injectable or strong hydrogel as well as 3D conveniently cross-linked scaffold. The surface of cellulose nanofibrils (CNF) can be modified to improve the bioactivity and the capability to link some active molecules essential for tissue engineering. In particular, CNF can be treated with (2,2,6,6-tetramethyl-piperidine-1-yl)oxyl radical (TEMPO) mediated oxidation and sodium hypochlorite as an oxidant, to introduce aldehyde and carboxyl groups on fibrils surface. It is composed of individual nanofibrils, typically with widths of 3.5 - 20 nm and length in the µm range that can be obtained as reversible or permanent gels through ionic or covalent linkages. This type of cellulose nanofibrils expose on their surface a significant number of aldehyde (211 ± 60 µmol/g) and carboxyl (764 ± 60 µmol/g) groups that are responsible of increasing its hydrophilicity. [90,91]

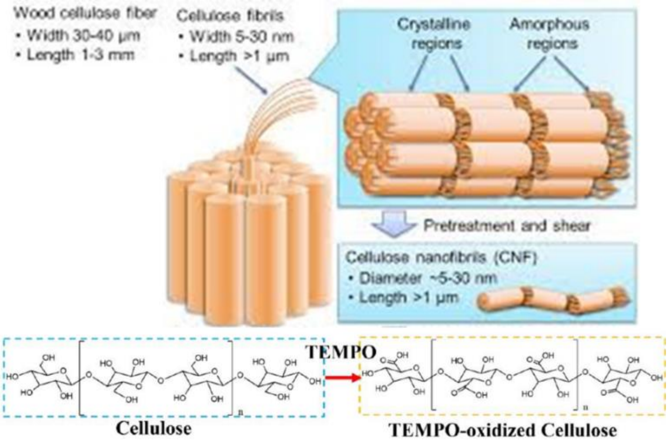

Figure 1.10. Structure of cellulose nanofibers extracted by wood and their oxidation with TEMPO.

1.3.2. Hydroxyapatite

Apatites constitute a large class of mineral phases exploited in several applications in different fields (e.g. biomedical and environmental). The general composition of apatites is $M_{10}(XO_4)_6Z_2$ where:

- M is a bivalent cation;
- XO4 is a trivalent anion;
- Z is a monovalent anion.

Changing types of ions, several apatites are obtained with different properties. The ratio M/X is used to recognized each apatite. The most common apatite is hydroxyapatite (HA), a basic calcium phosphate characterized by the following composition: $Ca_{10}(PO_4)_6(OH)_2$, whit a Ca/P ratio of 1.667 and a weight percentage of 39.84% (Ca), 56.77% (PO4), 3.39% (OH). In 1930, Naray-Szabo defined for the first time the structure of apatite and the adoption of P63/m symmetry was confirmed.[92] The calcium ions, are present into two crystallographically different symmetry sites, 4f for Ca(I) and 6h for Ca(II). The Ca(I) ions are identified in columns along the three-fold axes and each is nine-coordinated with O atoms. The Ca(II) ions are seven-coordinated, with six O atoms and one OH– ion (figure 1.11).[93–95] The solubility of HA was largely studied to understand better the bone and teeth physiology in terms of deposition and resorption processes. Different values of solubility constant of HA are reported, all around 10-49-10-59 and different solubility mechanisms are proposed such as:

- The different rates of the deposition and dissolution of an intermediate solid phases as $CaHPO_4*2H_20$ (brushite) and $CaHPO_4$ (monetite) can change the HA solubility.
- The solubility is influenced by powder weight and liquid volume ratio; the dissolution and precipitation processes can change the amount of superficial ions modifying the solubility constant.
- The solubility increases decreasing pH.
- Superficial ions are less constrained than inner ions, thus, more movable. HA with high superficial area has major solubility than those with low superficial area.
- Crystalline defects influence the dissolution process, crystalline solid with less defects and high crystal size are less soluble.

For many years, the stoichiometric HA described above has been considered very close to the apatite present in the human hard tissues, but the biological apatites is very different in term of composition and crystallinity from stoichiometric calcium hydroxyapatite.[58,96,97]

The most important difference between stoichiometric and biological HA is the chemical composition; stoichiometric HA is composed of Ca, PO_4 and OH while biologic one includes in its structure also several ions through ionic substitution or superficial adsorption (Figure 1.11).

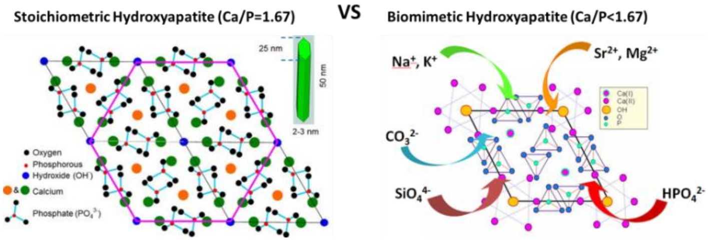

Figure 1.11. Cristal structure of stoichiometric (on the left) and biomimetic (on the right) hydroxyapatite

This incorporation of doping ions modifies several structural and chemical-physical HA parameters, without significantly changing the crystalline structure such as reticular constant, crystal's morphology and size, crystallinity, thermal stability and solubility.[55,97] Furthermore, biologic HA has a low crystallinity and is able to modify its crystalline structure when is undergone to external and internal stimuli. Especially the crystalline degree increases with age and with the presence of carbonate ion promoting the metabolic activity of tissue. Carbonate ion is detected in bone as 3-8 weight % depending on human age, it can substitute hoxydryl ion (carbonate-HA type A) or phosphate ion (carbonate-HA type B) changing the crystalline properties. Especially, type B carbonate-HA are present in young bones endowed them with higher reactivity and lower crystallinity, while type A carbonate HA are present in mature bones endowed with lower reactivity and higher crystallinity.[98] Also magnesium ion plays an important role in the HA biological activity, calcium substitution with magnesium ions increase the HA nucleation and inhibits the HA crystallization reducing Ca/P ratio and the crystal size. Furthermore, the magnesium presence modifies the crystal morphology and solubility. In vivo studies showed as high Mg^{2+} levels are detectable in young bone where osteogenesis steps starts, to disappear in mature bones.[58]

1.3.3. Biomineralization process

As above described during the natural bone formation, biomineralization process is the crystallization of inorganic phases on natural template, self-assembly and self-organization. In the early 2000s, researches exploited this process to generate macroscopically porous device composed of nano-building blocks as a new concept for bone scaffolding obtaining 3D constructs that strongly mimic the features of hard human tissues.[70,96,99] The process exploited the chemical-physical and topological complex information stored into the ultrastructure of collagen to induce self-assembling at increasing size scale and mineralization with biological-like hydroxyapatite.[31,97] Exactly as it happen in nature, collagen molecules promote a 3D complex arrangement and a low crystalline hydroxyapatite also due to the biological incorporation of foreign ions into the apatite phase. In details, to mimic in-lab the biomineralization process, a neutralization method was exploited where the acid solution containing PO_4^{3-} ions is mixed with collagen gel and then is dropped into a basic solution containing the Ca^{2+} ions. The pH of the suspension is increased up to neutral pH where two different mechanisms are simultaneously triggered. On one hand, the collagen fibers reach the isoelectric point leading to their assembly into a 3D network; on the other hand, the mineral nucleation starts in correspondence to the carboxylic groups exposed by the collagen molecule that bind calcium ions.[73,100] When the process is carried out in the presence of foreign ions, these can be introduced in the forming apatite phase, in order to obtain a hybrid material mimicking natural mineralized tissues. In particular, CO_3^{2-} ions can occupy two different sites of the apatite lattice. B-substitution occurs at the PO_4^{3-} site improving the osteoblasts' adhesion and is typical of young and immature bones. Conversely, carbonation in site A refers to partial substitution of OH^-, which increases the stability of mineral phase and it is more typical of mature bones. Mg^{2+} ions decrease the crystallinity and promote the nucleation and the apatite bioavailability. The aptitude of the apatite lattice to host several isovalent and heterovalent ion substitutions permits to synthesize apatite nanocrystals with multiple substitutions that can be used in different applications in regenerative medicine and nanomedicine.[59,96] The polymer mostly used in biomineralization process is collagen. However, the use of animal-derived collagen could present some limitations regarding its quality and purity, the possibility of immunological reactions that influence the final properties and applications. For this reasons, scientists have also tested various different macromolecules like cellulose, chitosan, gelatin, alginate, fibroin coming from natural sources, that exploit their electrically-charge surface groups for the nucleation of calcium phosphate, producing composites that can promote the cells adhesion and colonization (Figure 1.12).[101,102] These versatile materials may comply with specific goals tailoring relevant properties such as physical stability, mechanical strength, stiffness and hydrophilicity. Furthermore, thanks to functional groups able to bind Ca^{2+} ions, one of the precursors of biomineralization process, these biopolymers are excellent candidates for several applications including regenerative medicine (Figure 1.12).

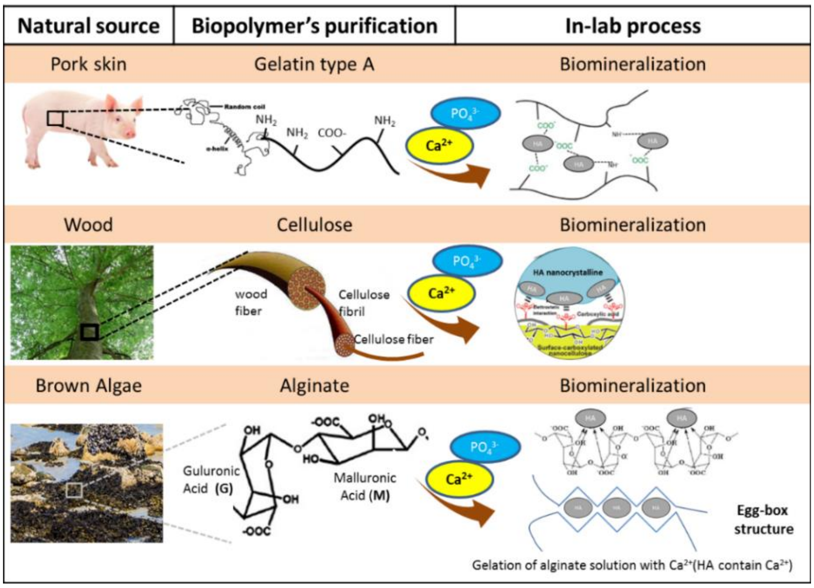

Figure 1.12. Scheme of the in-lab biomineralization process exploiting different polymers.

1.3.4. Magnetic material

Magnetic materials can be classified in paramagnetic and ferromagnetic. A paramagnetic material becomes magnetized upon exposure to a magnetic field, but when this field is switch off it does not show any permanent magnetization. Instead, a ferromagnetic material maintains its own magnetic field after the removal of magnetic field previously applied.[103] Furthermore, materials classified as "superparamagnetic" can be magnetized upon exposure to a magnetic field, highlighting a higher saturation magnetism without hysteresis and losing the magnetization when the magnetic field is turned off.[104,105] The use of magnetic materials have revolutionized different sectors of healthcare, due to many applications including non-invasive medical imaging, hyperthermia-based therapies, targeted delivery of therapeutic agents, radionuclide therapy, magnetic cell-seeding procedures, controlled cell proliferation and differentiation and tissue engineering.[106,107] This represents a very interesting and promising tool for new custom-made therapies. The superparamagnetic behaviour enables remote activation by weak magnetic field with possibility of magnetic driving *in vivo* and targeted release of therapeutics *on demand*, and besides their null remnant magnetization prevents their aggregation due to NPs mutual magnetic attraction.[108–111] Among the several applications of magnetic materials, cancer therapy is a 'hot topic' that exploits them to achieve a hyperthermia effect or as drug delivery systems.[57,106] Hyperthermia effect allow to damage the health cell in reversible way, while the cancer cell in irreversible way thanks to a temperature increase up to 41-45 °C. An alternative magnetic field allow to release energy in a form of heat also known as magnetic hyperthermia that provides an interesting and promising strategies in cancer therapies. Beside the use of magnetic nanoparticles in therapeutic and imaging field, an emerging concept in regenerative medicine is now the development of scaffolds that enhance bone regeneration by external magnetic fields. Previous research demonstrated that bone fracture healing, spinal fusion and bone ingrowth can be promoted by weak magnetic or pulsed electromagnetic fields (Figure 1.13).[112,113]

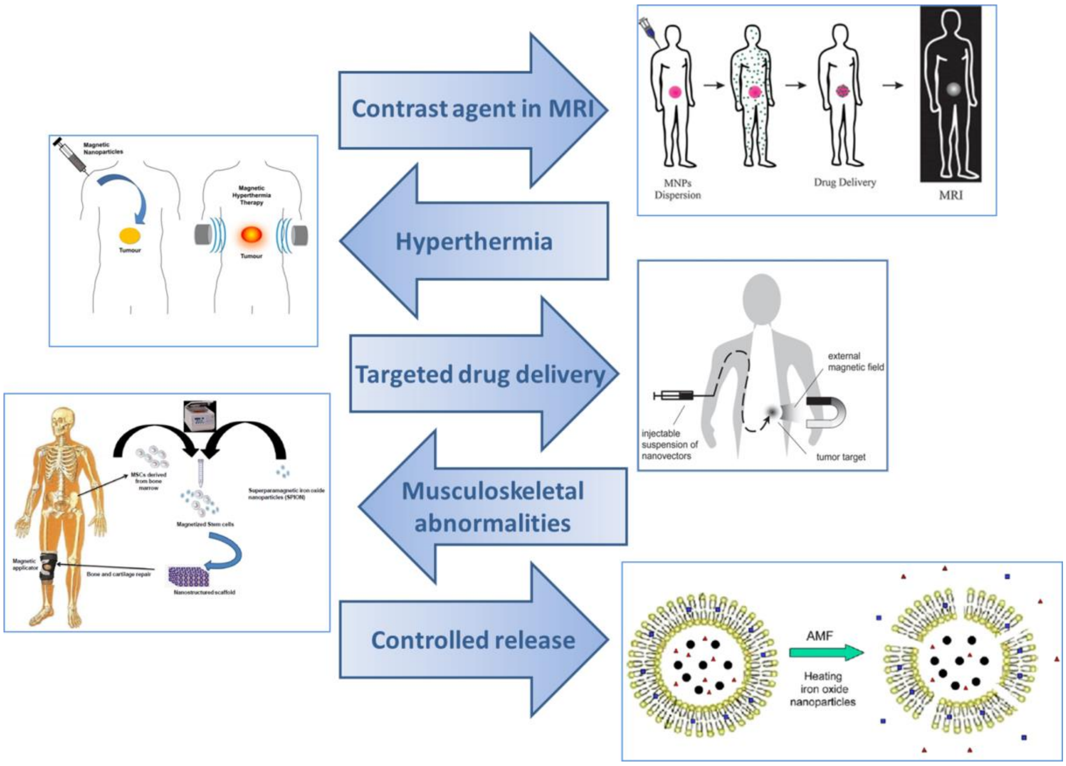

Figure 1.13. An overview about the different applications in which magnetic materials can be exploited.

Finally, magnetic nanoparticles (MNPs) showed magnetic properties and the ability to be incorporated at cellular and molecular levels, suggesting their use as drug delivery and imaging *in vitro* and *in vivo*. MNPs are prepared through different methods, such as physical methods by using colloidal routes and nanoparticles condensation of precursors from a gas or liquid phase or by laser ablation/evaporation to obtain nanoparticles with a diameter of 20-30 nm.[103] Wet chemical methods can be also used, such as co-precipitation, reaction environmentally constrained, hydrothermal and sol-gel reaction, all enabling tight control of the particle size.

Among magnetic nanoparticles, superparamagnetic iron oxide nanoparticles (SPIONs) are widely used in biomedical fields due to their easy to synthetize, low production cost, superparamagnetic nature and zero residual magnetization.[103] SPIONs maintain the chemical and colloidal stability and reduce the adverse reaction of drugs. They are used as drug delivery systems due to their ability to be guided to a specific tissue or organ by an external magnetic field.[103] The use of polymeric coating, combined to SPIONs is attractive due to: i) increased local drug concentrations reducing toxic effects on healthy cells or tissues, that provided new perspectives for drug delivery systems; ii) polymeric coatings can protect drug and prevent aggregation of SPIONs while preserving the mobility of the systems by using external magnetic field; iii) avoid that SPIONs is recognized as foreign particles and removed from the circulation by monocytes and macrophages.[109,114] On the other hand, especially in Magnetic Resonance Imaging, nanosystems have to own a longer half-life time in the blood circulation to improve the detection efficiency, the diagnosis and the therapeutic management of tumors. In the last decade, new applications for SPIONs have widely gained ground, such as cell internalization and related use in regenerative medicine. Biocompatible MNPs increase cell survival *in vitro* and for this reason, they can be also used in musculoskeletal abnormalities such as joint capsules, bone and ligaments. However, the use of SPIONs without any kind of coating is affected by several concern on their toxicity. Some researches highlighted as uncoated SPIONs induced redox cycling and catalytic chemistry via the Fenton[100], the most prevalent source of reactive oxygen species (ROS) in biological system and several studies demonstrated their body accumulation revealing a significantly toxicity.[105,115] For this reason, researches began to investigate the possibility to introduce in the apatitic latex, foreign ions just like happen in biological environment. In particular, previous research was dedicated to introduce iron ions in both two crystal sites of calcium in the apatite lattice and create a new biocompatible and bio-resorbable superparamagnetic apatite nanoparticles (FeHA), characterized by multiple functionality and high safety (Figure 1.14).[57] This new phase exhibits excellent properties such as:

- high magnetization under external fields, exhibiting excellent biocompatibility and bioresorbability;[116]
- Enhanced ability to induce cell proliferation and osteogenic differentiation both *in vitro* and *in vivo*, if compared to iron-free hydroxyapatite NPs;[110,111]
- Interacting with some drugs adsorbed on its surface, it becomes the nano-carrier that guides and releases the drug only into the target site exploiting an external magnetic field;[104]
- Coating with a polymeric phase, a building block material is obtained for the preparation of magnetic scaffolds for hard tissue regeneration or as drug delivery system to be guided inside the body by an external magnetic field.[117,118]

FeHA can represent a possible breakthrough in the current scenario of NPs used in medicine thanks to its biodegradability, biocompatibility and no toxicity of degradation by-products, overcoming side effects related to long-term cytotoxicity.[119,120] Finally, tailoring the amount of HA, crystal size and chemical-physical properties, FeHA can be modulate and adapt to specific needs in mediacal application.

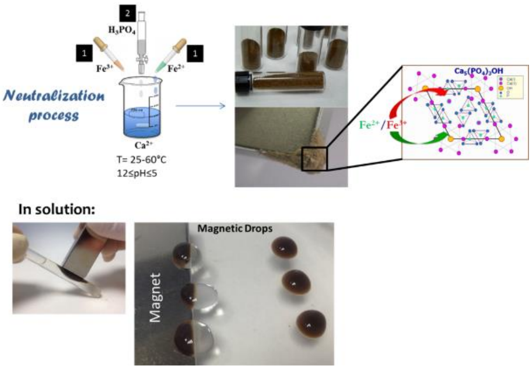

Figure 1.14. Synthesis of iron-doped hydroxyapatite (FeHA), a superparamagnetic bio-active phase.

1.4. Scaffold design for tissue engineering

Scaffold materials and fabrication technologies play a crucial role in tissue regeneration. Nowadays, the need of a 3D architecture is a key point in the design of a biomaterial able to promote tissue regeneration.[70,121] Thanks to 3D porous architecture, biomaterials support cell attachment and migration, vital cell nutrition diffusion and behavior modification of the cell phase. In fact, scaffolds act as templates in guiding the development of new tissues; especially scaffolds can be modulated to customize physical-chemical properties, the structure and the biological properties to achieve a desired material capable to efficiently answer the clinical need.[72,73] The design of the 3D architecture of a scaffold refers not only to macro-scale level corresponding to porosity, size and shape to reproduce a specific tissue, but also to the nano-level corresponding to cellular and molecular signals different in specific tissues.[31,122]

3D biomaterial scaffold requires specific need to support and promote tissue regeneration such as (Figure 1.15):

1. High and interconnected macroporosity to provide sufficient space for cellular activity;
2. Morphology able to host cells and close to specific tissue to regenerate;

3. Active surface capable to interact with cells giving their differentiation and deposition of mineral phase to regenerate new tissue;
4. High mechanical performance close to natural tissue to bear the changes of stress typical to natural tissue;
5. High biocompatibility and biodegradability; it has to be a stable 3D template during initial stages of tissue regeneration degrading only when newly formed tissue can replace it.[64,123]

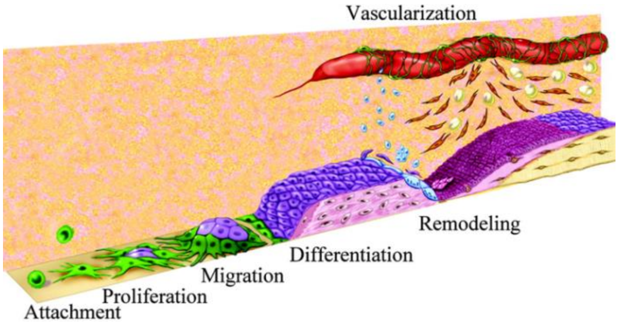

Figure 1.15. Schematic illustration of cellular integration and growing on a new support.

Nowadays several biomaterials such as collagen, hydroxyapatite (HA), calcium-phosphate cements, glass etc. are exploited to develop scaffolds as synthetic bone substitutes. However, the design of a mineralized scaffold composed of bioactive biomaterials and endowed by 3D hierarchically structure is still a challenge.[64] For this reason, research wants to find new natural structures featured by excellent properties capable to create innovative and smart biomimetic devices.

1.4.1. Scaffolds fabrication's technologies

Several approaches to the fabrication of scaffolds have been developed capable to create material with different properties, with the aim to produce porous biodegradable polymer scaffolds for several applications. Several techniques are nowadays present ranging from cheap and simple processes, giving relatively poor control over microstructure, to labored processes that give excellent control over micro-structure but often very expensive in term of money and time.

Gas-foaming. 3D scaffold has been developed using carbon dioxide as foaming agent. In this technology, the viscosity increase entrapping into structure gas bubbles that directly growth in the material matrix. (Figure 1.16).[8,124]

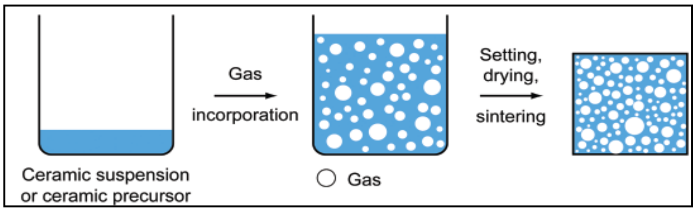

Figure 1.16. Schematic illustration of gas foaming technique.

Solvent casting. In this technique solid particles are embedded into the principal material solution, in this way particles form pores in the bulk. When solvent evaporates particles are still incorporated into material that solidified, afterwards particles are removed by using distilled water, an organic solvent or through degradation. This technique is always combined with other method, for example, with particulate leaching. (Figure 1.17).[125]

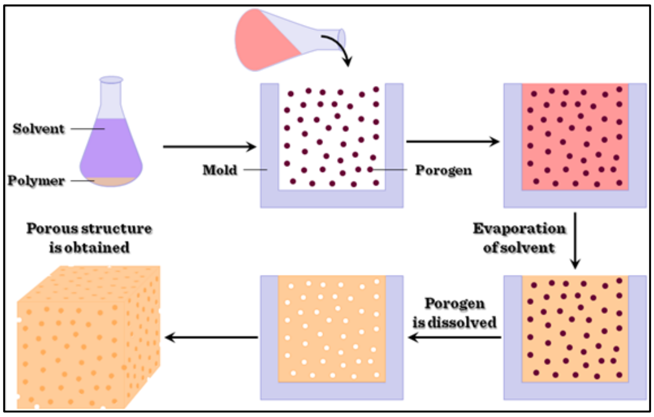

Figure 1.17. Schematic illustration of solvent casting technique.

Peptide self-assembling. Some peptides are able to assemble in α-helixes or β-sheets thanks to non-covalent bonds and interactions. This technique exploits this behavior alleviating problems inevitably associated with materials handling and solvent using. This process is reversible, pH-dependent and monitored by peptide type and concentration (Figure 1.18).[71]

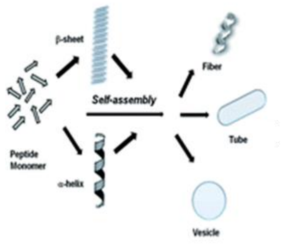

Figure 1.18. Schematic illustration of peptide self-assembling technique.

Electrospinning. It is a versatile technology able to develop highly porous nonwoven mats of micro-nanometric fibers. A metallic capillary ejecting the material solution represent the metallic collector of machinery and when a high voltage is applied between capillary and collector and the electrostatic force overcomes the cohesive force of the solution. An accelerated and stretched flux of material emerges from the needle directed to the collector. Before injection, the electrostatic repulsions cause a convective motion of the sample which leads to dry continuous solid fibers formation. Fiber size and morphology of sheets can be monitored varying features of the solution and the spinning variables (Figure 1.19).[126,127]

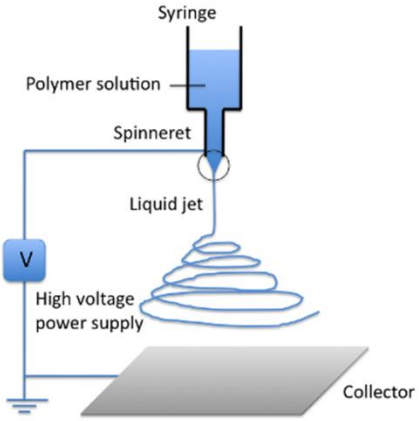

Figure 1.19. Schematic illustration of electrospinning technique.

Freeze-drying process. In this process a highly porous scaffold can be developed during two different steps: the freezing of the material (solution/dispersion) usually realized by a vertical cooling and the drying of the material by means of solvent sublimation applying a low vacuum and a very slow warming rate. When solvent is removed by sublimation, it leaves lacks that determine the porous morphology, so the freezing step is very important in order to produce desirable structures. There are many factors, which influence the morphology of the pores during freeze-drying process, the freezing temperature, rate and solute concentration strongly influence pore structure of the material. For example, a fast freezing produces a quick formation and a small growth of ice crystals, which leads to a material with small pores and in the opposite case using slow freezing a material with big pores is obtained (Figure 1.20).[99,128]

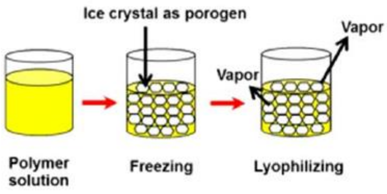

Figure 1.20. Schematic illustration of freeze-drying technique.

Rapid prototyping. It is widely exploited especially three-dimensional printing (3D printing) to design large and complex 3D porous matrices. Thanks to a control by computer, a layer by layer deposition allow to obtain a material with a proper and specific geometry (Figure 1.21).[121,129]

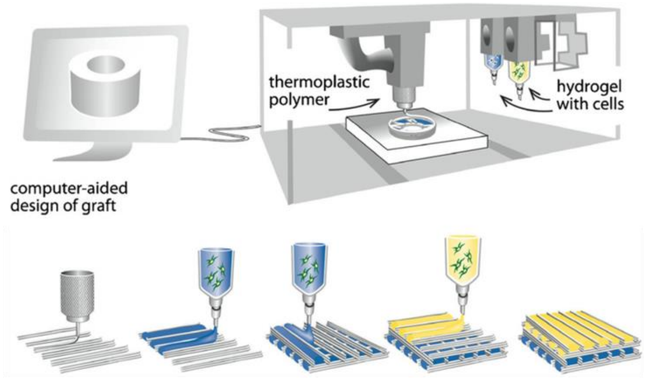

Figure 1.21. Schematic illustration of freeze-drying technique.

1.4.2. Cross-linking technologies

Scaffold stability is a crucial point in the design of the scaffold because it has to maintain its 3D structure during cell adhesion and proliferation and degrade when the newly tissue formed is ready to replace scaffold. Natural polymers due to high biodegradability, are often characterized by a fast degradation. To overcome this issue, cross-linking strategies are exploited.[130,131] Cross-linking agent can be chemical or natural molecules or physical treatment able to create strong intermolecular bond as bridges between polymer fibers improving molecule packaging and reducing polymer mobility.[78,85] Therefore, cross-linking techniques have been explored to modulate thermal resiliency, decrease solubility in high humidity condition and physiological environment, as well as modulate mechanical strength. Among several cross-linker methods, in this PhD thesis, two different cross-linking methods are studied: i) using cross-linking molecules as 1,4-

Butanediol diglycidyl ether (BDDGE), genepin and hexamethylendiamine (HMDA); ii) using physical cross-linking such as dehydrothermal treatment.

1.4.2.1. Chemical cross-linking

Chemical cross-linking is featured by several functional side groups within its structure which easily undergoes chemical linkage promoting a higher cross-linking degree. Usually the chemical cross-linkers are bi-functional agents such as glutaraldehyde (GTA), 1,4-butanediol diglycidyl ether (BDDGE), hexamethylenediamine (HMDA), 1-ethyl-3-(3-dimethylamino propyl) carbodiimide hydrochloride (EDC) and genipin.

1,4-butenediol diglycidyl ether (BDDGE) is a diepoxy cross-linking agent and it is widely used to cross-link materials which have amine or carboxylic acid groups in their structure. It is exploited in biomedical field due to its lower toxicity in comparison with other ether-bond cross-linking. Furthermore, BDDGE is biodegradability and capable to increase stability of final biomaterials which readily react with the epoxide groups present at both ends of molecules. Depending on solution pH, BDDGE prefers to react with different functional groups: alcohol or carboxylic acids in basic condition and primary amino groups in acid condition (Figure 1.22).[132]

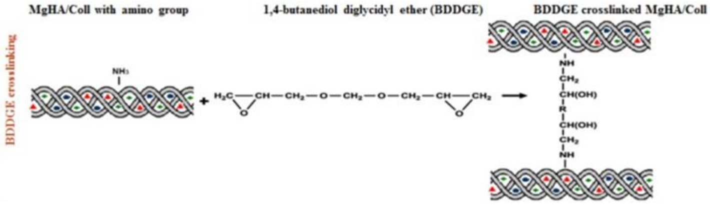

Figure 1.22. Reaction mechanism involving BDDGE and amino functional groups of Collagen.

Genipin derives from Gardenia fruit (Gardenia Jasminoides Ellis) and it is a natural water soluble cross-linking agent. Genipin cytotoxicity is much lower compared to glutaraldehyde or other cross-linkers as reported in many studies. Genipin spontaneously bind with biopolymers such as collagen, gelatin, chitosan where amino groups are present in their structures. Thanks to the reaction above-described a new amide bound is revealing through color changing passing from clear meaning no bond to blue meaning a spontaneous reaction between amino acids and protein. The cross-linking of genipin is promoted at pH bigger or equal to 5.5 as Figure 1.23 shows.[85,133]

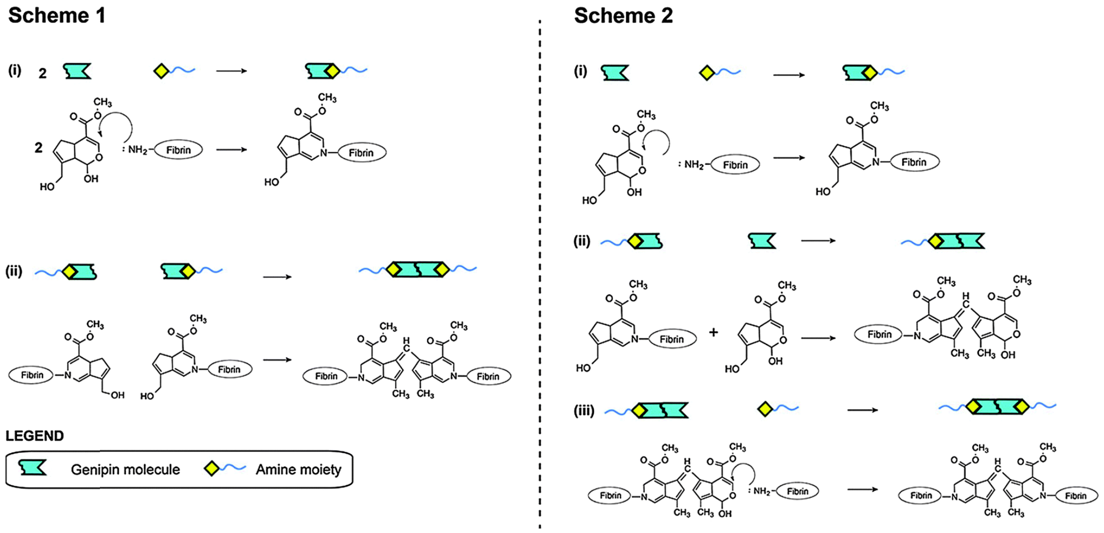

Figure 1.23. Different reaction mechanism involving genipin and amino functional groups of polymers.[133]

Hexamethylenediamine is a diamine organic compound used to stabilize polymers with free carboxylic or carbonyl groups due to its structure consisting of a hexamethylene hydrocarbon chain terminated with amine functional groups. Among the diamines, those characterized by long carbon chains allow the creation of covalent amide bonds even between the fibers far apart (Figure 1.25).[90]

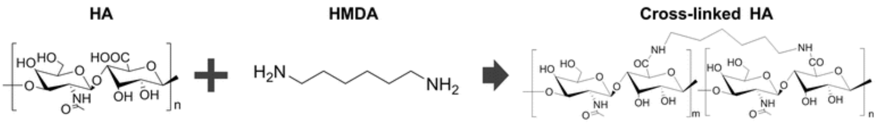

Figure 1.25. reaction mechanism involving HMDA and carboxylic group of hyaluronic acid (HA).

1.4.2.2. Physical cross-linking

The physical cross-linking methods include the dehydrothermal (DHT), ultraviolet (UV) and gamma irradiation that is considered excellent non-toxic cross-linking. However, the dehydration of the scaffold surface reduces the wettability of material and confer it less favorable for cell culture application.

Dehydrothermal treatment (DHT) is specific treatment where temperature and vacuum is exploited to cross-link the biomaterial (160 °C under vacuum). Intermolecular linkages are formed between functional group through esterification or amide formation due to the increase of temperature that avoid bound water molecules. Typically, when amine and carboxyl groups are present in the biomaterial, DHT occurs.[134] This technique is widely used, but it is necessary that functional groups are close to each other so that the reaction happens. However, DHT method does not reported any kind of toxicity, for this reason it is exploited in tissue engineering applications.[135] However, a drawback of DHT is due to the effect of water removal on the hydrophilicity, because the removal of bound water molecules results in a reduction of swelling ratio due to a low hydropholicity.[134]

1.5. Fields of interest in the thesis

Biomaterials are widely engaged in biomedical and in cosmetic field with different applications able to answer clinical needs of patients and to improve their life quality with several successful devices (Figure 1.26).

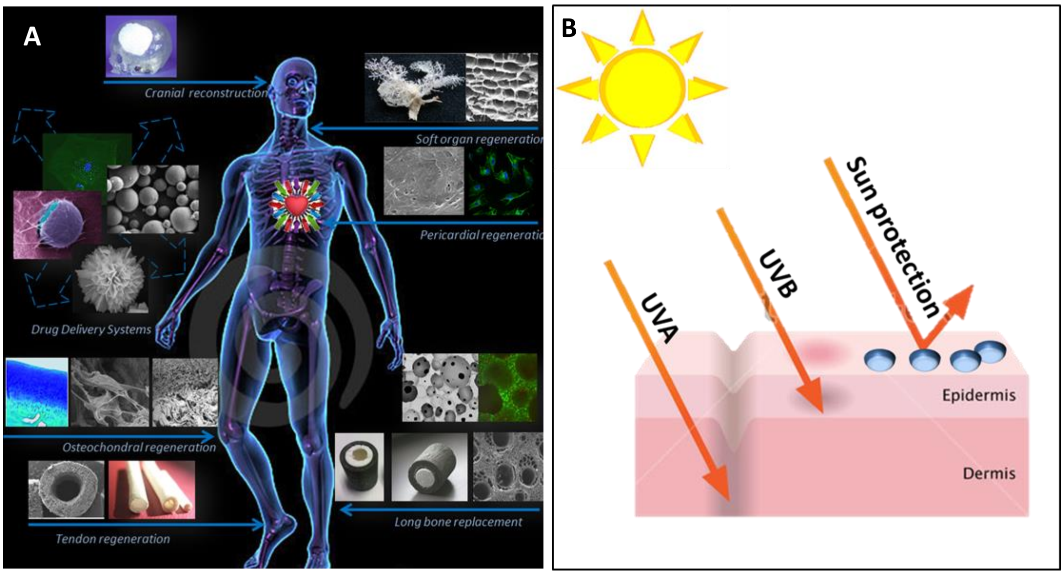

Figure 1.26. Schematic illustration of several application of biomaterials in A) biomedical and B) cosmetic fields.

Orthopedic field. Several issues can lead to an orthopedic prosthetic implant such as arthrosis (damage of articular cartilage), trauma events, aging disease (osteoporosis), bone cancer and bone tissue necrosis.[63] Its main goal is to preserve the integrity and functionality of bone tissue, ensuring that stress was very similar to physiological one. The preservation of bone-implant interface is due to many factors such as stress characteristics, changing in tissue anatomy, reaction between implant and surrounding tissues, trauma during surgery, implant surface as well as bone-implant movement that can limit new tissue formation. All parameters are responsible for the long-term implant success and stability.[136,137] Polymeric materials are also used as coating of metal implants to obtain an interaction implant-tissue with similar properties such as young modulus able to distribute better the stress. Furthermore, the coating with a porous polymeric material such as polysulfone and polyethylene, promotes osseointegration of implant and the growth of new bone tissue inside pores. Finally, biodegradable and bioresorbable polymeric polylactic and polyglicol acid-based materials are exploited in the development of plates and intramedullary nails for the regeneration of fractures subjected to low stress. In this case, after bone regeneration, these materials are not removed by surgery, but by resorption of natural tissue. In the last decades some biomaterials completely biodegradable and bioresorbable are commercially developed for bone and osteochondral regeneration (MaioRegen® and RegenOss®).[31,72,73,138] The advantages to use that materials are many, such as: (i) behave as a template for tissue re-growth, (ii) is used as a medium to transport nutrients and metabolic products, (iii) promote a faster tissue regeneration and (iv) degrades completely in harmless by-product during regeneration.

Cosmetic field. Frequent exposure to solar ultraviolet (UV) radiation is well known to cause damage to exposed surfaces. Fading and ageing of paints, fabrics and plastic coatings as well as sun-related skin cancer are major industrial, environmental and health concerns. The sun emits non-ionizing electromagnetic radiation (EMR) composed of UV (100-400 nm), visible (400-780 nm) and infrared (780-5000 nm) radiation. With regard to human health, the most relevant and concerning form of EMR is UVR composed of wavelengths UVC (100-290 nm), UVB (290-320 nm) and UVA (320-400 nm). UVC are absorbed by atmospheric ozone and do not reach the earth surface, while the exposure to UVA and UVB radiation is considered largely unavoidable because can lead to sunburn, photocarcinogenesis, photoimmunosuppression and photoaging.[139] Several researches have highlighted the relation between the risk of developing melanoma with the increased numbers of acquired melanocytic nevi, while the use of sunscreen was demonstrated to diminish the incidence of nevi on sun-exposed areas of the body in children providing important evidence for the preventive effect of sunscreens against the development of this risk factor for melanoma.[140,141] Sunscreens are divided into two major classes: i) chemical or organic sunscreen, in which the light-active components are organic molecules capable of adsorbing UVR; ii) physical or inorganic UV filters (i.e., titanium dioxide (TiO_2) and zinc oxide (ZnO)) composed by physical barriers reflecting radiation.[141] However, while the occurrence of skin cancers is universally recognized to be in direct relation with UVR exposure, the beneficial of using sunscreens to minimize adverse health effects are still controversial. For example, photocatalytic activity generating by organic UV filters and TiO_2 and ZnO nanoparticles, is not a desirable feature of any sunscreen since it could lead to the generation of free radicals and other reactive species that can cause some of the health problems associated with UV exposure.[141,142] To overcome this issue, the research of new biocompatible physical filters preventing safety issues connected with the use of TiO_2 and ZnO has led to the development of hydroxyapatite (HA) NPs with appropriate absorption in the UV region as active components of physical sunscreen. The hexagonal HA lattice easily incorporates foreign ions, inducing modifications in lattice parameters, crystal size and shape, particles morphology, thermal stability and crystallinity. Ions employed for HA doping reported in the literature are Fe^{3+}, Fe^{2+}, Ti^{4+} and Zn^{2+}, some of them allow to confer UV-reflectance properties in order to exploit this biomaterials in cosmetic field.[143,144]

Drug delivery field. Drug delivery is the method or process for transporting a pharmaceutical compound in the body as needed to safely achieve its desired therapeutic effect. It may involve scientific site-targeting within the body, or it might involve facilitating systemic pharmacokinetics. In any case, it is typically concerned with both quantity and duration of drug presence. Drug delivery is often approached via a drug chemical formulation, but it may also involve medical devices or drug-device combination products. Drug delivery is a concept heavily integrated with dosage form and route of administration, the latter sometimes even being considered part of the definition.[145] For this purpose, several drug delivery systems have been formulated and are being investigated. These include liposomes, microspheres, gels, prodrugs, polymeric nanoparticles, cyclodextrins, among others. Nanoparticles are widely studied because their application is expected to change the scenery of pharmaceutical and biotechnological industries. In fact, the clinical application of newer and more effective drugs is still constrained due to the presence of several barriers and blocks between the site of introduction and the target site such as reticulo-endothelial system, membrane barriers and blood-brain barrier, or the possibility to be inactivated or degraded. Besides, systemic drug delivery limits the therapeutic effectiveness and more easily provoke undesired secondary effects. Today, the development of carriers with smart multifunctional properties and ability of release along defined spatial-temporal profiles and under specific stimulus is a particularly hot topic in materials research.[36,108,146]

REFERENCES

1. Gomes, M. E., Rodrigues, M. T., Domingues, R. M. A. & Reis, R. L. Tissue Engineering and Regenerative Medicine: New Trends and Directions—A Year in Review. *Tissue Eng. Part B Rev.* **23,** 211–224 (2017).

2. Wegst, U. G. K., Bai, H., Saiz, E., Tomsia, A. P. & Ritchie, R. O. Bioinspired structural materials. *Nat. Mater.* **14,** 23–36 (2015).

3. Ma, P. X. Biomimetic materials for tissue engineering. *Adv. Drug Deliv. Rev.* **60,** 184–198 (2008).

4. Loh, Q. L. & Choong, C. Three-Dimensional Scaffolds for Tissue Engineering Applications: Role of Porosity and Pore Size. *Tissue Eng. Part B Rev.* **19,** 485–502 (2013).

5. Dvir, T., Timko, B. P., Kohane, D. S. & Langer, R. Nanotechnological strategies for engineering complex tissues. *Nat. Nanotechnol.* **6,** 13–22 (2011).

6. Tampieri, A., Sprio, S., Sandri, M. & Valentini, F. Mimicking natural bio-mineralization processes: A new tool for osteochondral scaffold development. *Trends Biotechnol.* **29,** 526–535 (2011).

7. Uchida, N. *et al.* Nanometer-sized extracellular matrix coating on polymer-based scaffold for tissue engineering applications. *J. Biomed. Mater. Res. Part A* **104,** 94–103 (2015).

8. Sprio, S. *et al.* Bio-inspired assembling/mineralization process as a flexible approach to develop new smart scaffolds for the regeneration of complex anatomical regions. *J. Eur. Ceram. Soc.* **36,** 2857–2867 (2016).

9. Iouguina, A., Dawson, J., Hallgrimsson, B. & Smart, G. *Biologically informed disciplines: A comparative analysis of bionics, biomimetics, biomimicry, and bio-inspiration among others*. *International Journal of Design & Nature and Ecodynamics* **9,** (2014).

10. Vincent, J. F. V., Bogatyreva, O. A., Bogatyrev, N. R., Bowyer, A. & Pahl, A. K. Biomimetics: Its practice and theory. *J. R. Soc. Interface* **3,** 471–482 (2006).

11. Hench, L. L. Biomaterials. *Science (80-.).* **208,** 826 LP-831 (1980).

12. L Hench, L. & Wilson, J. W. *Surface Active Biomaterials*. *Science (New York, N.Y.)* **226,** (1984).

13. Hench, L. L. & Polak, J. M. Third-Generation Biomedical Materials. *Science (80-.).* **295,** 1014 LP-1017 (2002).

14. Raghvendra, K. M. Nanostructured biomimetic, bioresponsive, and bioactive biomaterials. *Fundam. Biomater. Met.* 35–65 (2018). doi:10.1016/B978-0-08-102205-4.00002-7

15. Roveri, N., Palazzo, B. & Iafisco, M. The role of biomimetism in developing nanostructured inorganic matrices for drug delivery. *Expert Opin. Drug Deliv.* **5,** 861–877 (2008).

16. Mann, S., Heywood, B. R., Rajam, S. & Wade, V. J. in *Mechanisms and Phylogeny of Mineralization in Biological Systems: Biomineralization {\textasciiacutex}90* (eds. Suga, S. & Nakahara, H.) 47–55 (Springer Japan, 1991). doi:10.1007/978-4-431-68132-8_8

17. Gower, L. B. *et al.* Biomimetic Approach Toward the Development of Bone-Graft. *Acta biomateralia* **7,** 3158–3169 (2012).

18. Baino, F. & Ferraris, M. Learning from Nature: Using bioinspired approaches and natural materials to make porous bioceramics. *International Journal of Applied Ceramic Technology* **14,** 507–520 (2017).

19. Kolle, M. & Lee, S. Progress and Opportunities in Soft Photonics and Biologically Inspired Optics. *Adv. Mater.* **30,** 1702669 (2018).

20. Fontana, G., Delgado, L. M. & Cigognini, D. in *Extracellular Matrix for Tissue Engineering and Biomaterials* 113–147 (Springer, 2018).

21. Power, J. & Bernabei, R. in *Advances in Manufacturing and Processing of Materials and Structures* 51–72 (CRC Press, 2018).

22. Yang, J. *et al.* Functional Polymeric Materials Inspired by Geckos, Mussels, and

Spider Silk. *Macromol. Chem. Phys.* **219,** 1800051 (2018).

23. Sun, J. & Bhushan, B. Nanomanufacturing of bioinspired surfaces. *Tribol. Int.* **129,** 67–74 (2019).

24. Park, K. H., Seong, K.-Y., Yang, S. Y. & Seo, S. Advances in medical adhesives inspired by aquatic organisms' adhesion. *Biomater. Res.* **21,** 16 (2017).

25. Schroeder, T. B. H., Houghtaling, J., Wilts, B. D. & Mayer, M. It's Not a Bug, It's a Feature: Functional Materials in Insects. *Adv. Mater.* **30,** 1705322 (2018).

26. Lenau, T. A., Metze, A.-L. & Hesselberg, T. Paradigms for biologically inspired design. in *Bioinspiration, Biomimetics, and Bioreplication VIII* **10593,** 1059302 (International Society for Optics and Photonics, 2018).

27. Elbaz, A. *et al.* Recent biomedical applications of bio-sourced materials. *Bio-Design Manuf.* **1,** 26–44 (2018).

28. Egan, P., Sinko, R., Leduc, P. R. & Keten, S. The role of mechanics in biological and bio-inspired systems. *Nat. Commun.* **6,** 1–12 (2015).

29. Mann, S. in *Biomineralization: Principles and Concepts in Bioinorganic Materials Chemistry* (2001).

30. Beniash, E. Biominerals—hierarchical nanocomposites: the example of bone. *Wiley Interdiscip. Rev. Nanomedicine Nanobiotechnology* **3,** 47–69 (2011).

31. Tampieri, A. *et al.* Biologically inspired synthesis of bone-like composite: Self-assembled collagen fibers/hydroxyapatite nanocrystals. *J. Biomed. Mater. Res. - Part A* **67,** 618–625 (2003).

32. Wingender, B., Bradley, P., Saxena, N., Ruberti, J. W. & Gower, L. Biomimetic organization of collagen matrices to template bone-like microstructures. *Matrix Biol.* **52–54,** 384–396 (2016).

33. Rnjak-Kovacina, J. *et al.* Lyophilized Silk Sponges: A Versatile Biomaterial Platform for Soft Tissue Engineering. *ACS Biomater. Sci. Eng.* **1,** 260–270 (2015).

34. Thomas Pashuck, E. & Stevens, M. M. Designing regenerative biomaterial

therapies for the clinic. *Sci. Transl. Med.* **4,** 1–12 (2012).

35. Tong, Z. *et al.* Towards a defined ECM and small molecule based monolayer culture system for the expansion of mouse and human intestinal stem cells. *Biomaterials* **154,** 60–73 (2018).

36. del Mercato, L. L. *et al.* Design and characterization of microcapsules-integrated collagen matrixes as multifunctional three-dimensional scaffolds for soft tissue engineering. *J. Mech. Behav. Biomed. Mater.* **62,** 209–221 (2016).

37. Craddock, R. J. *et al.* Extracellular matrix fragmentation in young, healthy cartilaginous tissues. *Eur. Cells Mater.* **35,** 34–53 (2018).

38. Featherall, J. *et al.* In vivo formation of stable hyaline cartilage by transplantation of naive human bone marrow stromal cells. *Osteoarthr. Cartil.* **26,** S135–S136 (2018).

39. Simon, T. M. & Jackson, D. W. Articular cartilage: injury pathways and treatment options. *Sports Med. Arthrosc.* **26,** 31–39 (2018).

40. Stegen, S. & Carmeliet, G. The skeletal vascular system–Breathing life into bone tissue. *Bone* **115,** 50–58 (2018).

41. Bose, S., Tarafder, S. & Bandyopadhyay, A. Effect of chemistry on osteogenesis and angiogenesis towards bone tissue engineering using 3D printed scaffolds. *Ann. Biomed. Eng.* **45,** 261–272 (2017).

42. Olszta, M. J. *et al.* Bone structure and formation: A new perspective. *Materials Science and Engineering R: Reports* **58,** 77–116 (2007).

43. Boskey, A. L. Mineralization of Bones and Teeth. *Elements* **3,** 385 LP-391 (2007).

44. Gordeladze, J. O., Haugen, H. J., Lyngstadaas, S. P. & Reseland, J. E. Bone tissue engineering: state of the art, challenges, and prospects. *Tissue Eng. Artif. Organs Regen. Med. Smart Diagnostics Pers. Med.* **2,** 525–551 (2017).

45. Bartl, R. & Bartl, C. in (eds. Bartl, R. & Bartl, C.) 21–30 (Springer International Publishing, 2017). doi:10.1007/978-3-319-29182-6_3

46. Katsimbri, P. The biology of normal bone remodelling. *Eur. J. Cancer Care (Engl).* **26,** e12740 (2017).

47. Pacifici, R. T cells, osteoblasts, and osteocytes: interacting lineages key for the bone anabolic and catabolic activities of parathyroid hormone. *Ann. N. Y. Acad. Sci.* **1364,** 11–24 (2015).

48. Mizuno, H., Kikuta, J. & Ishii, M. In vivo live imaging of bone cells. *Histochem. Cell Biol.* **149,** 417–422 (2018).

49. Florencio-silva, R. *et al.* Mechanobiology of bone tissue.pdf. **2015,** (2015).

50. Bonfield, W. in *Natural and living biomaterials* 43–60 (CRC Press, 2018).

51. Milovanovic, P. *et al.* Multi-level characterization of human femoral cortices and their underlying osteocyte network reveal trends in quality of young, aged, osteoporotic and antiresorptive-treated bone. *Biomaterials* **45,** 46–55 (2015).

52. Addadi, L., Raz, S. & Weiner, S. Taking Advantage of Disorder: Amorphous Calcium Carbonate and Its Roles in Biomineralization. *Adv. Mater.* **15,** 959–970 (2003).

53. Gómez-Morales, J., Delgado-López, J. M., Iafisco, M., Hernández-Hernández, A. & Prat, M. Amino Acidic Control of Calcium Phosphate Precipitation by Using the Vapor Diffusion Method in Microdroplets. *Cryst. Growth Des.* **11,** 4802–4809 (2011).

54. Lei, Y. *et al.* Strontium hydroxyapatite/chitosan nanohybrid scaffolds with enhanced osteoinductivity for bone tissue engineering. *Mater. Sci. Eng. C* **72,** 134–142 (2017).

55. Iafisco, M., Ruffini, A., Adamiano, A., Sprio, S. & Tampieri, A. Biomimetic magnesium-carbonate-apatite nanocrystals endowed with strontium ions as anti-osteoporotic trigger. *Mater. Sci. Eng. C* **35,** 212–219 (2014).

56. Sprio, S. *et al.* Nature-Inspired Nanotechnology and Smart Magnetic Activation: Two Groundbreaking Approaches Toward a New Generation of Biomaterials for Hard Tissue Regeneration. *Adv. Tech. Bone Regen.* (2016). doi:10.5772/63229

57. Tampieri, A. *et al.* Intrinsic magnetism and hyperthermia in bioactive Fe-doped hydroxyapatite. *Acta Biomater.* **8,** 843–851 (2012).

58. Landi, E. *et al.* Biomimetic Mg-substituted hydroxyapatite: from synthesis to in vivo behaviour. *J. Mater. Sci. Mater. Med.* **19,** 239–247 (2008).

59. Ramírez-Rodríguez, G. B. *et al.* Biomimetic mineralization of recombinant collagen type I derived protein to obtain hybrid matrices for bone regeneration. *J. Struct. Biol.* (2016). doi:10.1016/j.jsb.2016.06.025

60. Roy, R., Boskey, A. & Bonassar, L. J. Processing of type I collagen gels using nonenzymatic glycation. *J. Biomed. Mater. Res. - Part A* **93,** 843–851 (2010).

61. Fratzl, P. & Weinkamer, R. Nature’s hierarchical materials. *Progress in Materials Science* **52,** 1263–1334 (2007).

62. Nair, L. S. & Laurencin, C. T. Biodegradable polymers as biomaterials. *Progress in Polymer Science (Oxford)* **32,** 762–798 (2007).

63. Martin, V. & Bettencourt, A. Bone regeneration: Biomaterials as local delivery systems with improved osteoinductive properties. *Mater. Sci. Eng. C* **82,** 363–371 (2018).

64. Sprio, S. *et al.* Biomimesis and biomorphic transformations: New concepts applied to bone regeneration. *J. Biotechnol.* **156,** 347–355 (2010).

65. Schmid, O., Padel, S. & Levidow, L. *The Bio-Economy Concept and Knowledge Base in a Public Goods and Farmer Perspective. Bio-based and Applied Economics* **1,** (2012).

66. Savini Elisa. Design and development of biomineralized nanostructured devices from natural sources for biomedical applications. (University of Bologna, 2016).

67. Yue, K. *et al.* Synthesis, properties, and biomedical applications of gelatin methacryloyl (GelMA) hydrogels. *Biomaterials* **73,** 254–271 (2015).

68. Boanini, E., Rubini, K., Panzavolta, S. & Bigi, A. Chemico-physical characterization of gelatin films modified with oxidized alginate. *Acta Biomater.*

6, 383–388 (2010).

69. Grigore, M., Grumezescu, A., Holban, A., Mogoşanu, G. & Andronescu, E. Collagen-Nanoparticles Composites for Wound Healing and Infection Control. *Metals (Basel).* **7,** 516 (2017).

70. Gostynska, N. *et al.* 3D porous collagen scaffolds reinforced by glycation with ribose for tissue engineering application. *Biomed. Mater.* **12,** (2017).

71. Luo, T. & Kiick, K. L. Collagen-like peptides and peptide-polymer conjugates in the design of assembled materials. *Eur. Polym. J.* **49,** 2998–3009 (2013).

72. Sandri, M. *et al.* Fabrication and Pilot In Vivo Study of a Collagen-BDDGE-Elastin Core-Shell Scaffold for Tendon Regeneration. *Front. Bioeng. Biotechnol.* **4,** 1–14 (2016).

73. Tampieri, A. *et al.* Design of graded biomimetic osteochondral composite scaffolds. *Biomaterials* **29,** 3539–3546 (2008).

74. Tillet, G., Boutevin, B. & Ameduri, B. Chemical reactions of polymer crosslinking and post-crosslinking at room and medium temperature. *Prog. Polym. Sci.* **36,** 191–217 (2011).

75. Hoque, M. E., Nuge, T., Yeow, T. K., Nordin, N. & Prasad, R. G. S. V. Gelatin Based Scaffolds for Tissue Engineering – a Review. *Polym. Res. J.* **9,** 1935–2530 (2015).

76. Naidu, B. V. K. & Paulson, A. T. A new method for the preparation of gelatin nanoparticles: Encapsulation and drug release characteristics. *J. Appl. Polym. Sci.* **121,** 3495–3500 (2011).

77. Sobhana, S. S. L., Sundaraseelan, J., Sekar, S., Sastry, T. P. & Mandal, A. B. Gelatin-Chitosan composite capped gold nanoparticles: A matrix for the growth of hydroxyapatite. *J. Nanoparticle Res.* **11,** 333–340 (2009).

78. Prasertsung I., M. R. & Damrongsakkul S., W. C. Surface modification of dehydrothermal crosslinked gelatin film using a 50 Hz oxygen glow discharge. *Surf. Coatings Technol.* **205,** 133–138 (2010).

79. Bigi, A., Cojazzi, G., Panzavolta, S., Roveri, N. & Rubini, K. Stabilization of gelatin films by crosslinking with genipin. *Biomaterials* **23,** 4827–4832 (2002).

80. Bidarra, S. J., Barrias, C. C. & Granja, P. L. Injectable alginate hydrogels for cell delivery in tissue engineering. *Acta Biomater.* **10,** 1646–1662 (2014).

81. Daemi, H. & Barikani, M. Synthesis and characterization of calcium alginate nanoparticles, sodium homopolymannuronate salt and its calcium nanoparticles. *Sci. Iran.* **19,** 2023–2028 (2012).

82. Mandal, S., Kumar, S. S., Krishnamoorthy, B. & Basu, S. K. Development and evaluation of calcium alginate beads prepared by sequential and simultaneous methods . *Brazilian J. Pharm. Sci. (Impresso); Vol 46, No 4 (2010)DO - 10.1590/S1984-82502010000400021* (2010).

83. Mao, J. S., Zhao, L. G., Yin, Y. J. & Yao, K. De. Structure and properties of bilayer chitosan-gelatin scaffolds. *Biomaterials* **24,** 1067–1074 (2003).

84. De, S. & Robinson, D. P olymer relationships during preparation of chitosan – alginate and poly-l-lysine – alginate nanospheres. **89,** 101–112 (2003).

85. Yan, L. P. *et al.* Genipin-cross-linked collagen/chitosan biomimetic scaffolds for articular cartilage tissue engineering applications. *J. Biomed. Mater. Res. - Part A* **95 A,** 465–475 (2010).

86. Pulieri, E. *et al.* Chitosan/gelatin blends for biomedical applications. *J. Biomed. Mater. Res. - Part A* **86,** 311–322 (2008).

87. Andresen, M., Johansson, L.-S., Tanem, B. S. & Stenius, P. Properties and characterization of hydrophobized microfibrillated cellulose. *Cellulose* **13,** 665–677 (2006).

88. Vlaia, L., Coneac, G., Olariu, I., Vlaia, V. & Lupuleasa, D. Cellulose-Derivatives-Based Hydrogels as Vehicles for Dermal and Transdermal Drug Delivery. *Emerg. Concepts Anal. Appl. Hydrogels* (2016). doi:10.5772/63953

89. Lin, N. & Dufresne, A. Nanocellulose in biomedicine: Current status and future prospect. *Eur. Polym. J.* **59,** 302–325 (2014).

90. Syverud, K., Pettersen, S. R., Draget, K. & Chinga-Carrasco, G. Controlling the elastic modulus of cellulose nanofibril hydrogels---scaffolds with potential in tissue engineering. *Cellulose* **22,** 473–481 (2015).

91. Rashad, A., Mustafa, K., Heggset, E. B. & Syverud, K. Cytocompatibility of Wood-Derived Cellulose Nanofibril Hydrogels with Different Surface Chemistry. *Biomacromolecules* **18,** 1238–1248 (2017).

92. Nabay-Szabo. The structure of Apatite (CaF)Ca4(PO4)3. *Zeit. Krist.* **75,** 387–398 (1930).

93. Ran, J. *et al.* Comparisons among Mg, Zn, Sr, and Si doped nano-hydroxyapatite/chitosan composites for load-bearing bone tissue engineering applications. *Mater. Chem. Front.* **1,** 900–910 (2017).

94. Marchegiani, F. *et al.* Hydroxyapatite synthesis from biogenic calcite single crystals into phosphate solutions at ambient conditions. *J. Cryst. Growth* **311,** 4219–4225 (2009).

95. Jokić, B. *et al.* Synthesis and characterization of monetite and hydroxyapatite whiskers obtained by a hydrothermal method. *Ceram. Int.* **37,** 167–173 (2011).

96. Krishnakumar, G. S. *et al.* Ribose mediated crosslinking of collagen-hydroxyapatite hybrid scaffolds for bone tissue regeneration using biomimetic strategies. *Mater. Sci. Eng. C* **77,** 594–605 (2017).

97. Tampieri, A., Celotti, G. & Landi, E. From biomimetic apatites to biologically inspired composites. *Anal. Bioanal. Chem.* **381,** 568–576 (2005).

98. Landi, E., Tampieri, A., Celotti, G., Vichi, L. & Sandri, M. Influence of synthesis and sintering parameters on the characteristics of carbonate apatite. *Biomaterials* **25,** 1763–1770 (2004).

99. Arora, A., Kothari, A. & Katti, D. S. Pore orientation mediated control of mechanical behavior of scaffolds and its application in cartilage-mimetic scaffold design. *J. Mech. Behav. Biomed. Mater.* **51,** 169–183 (2015).

100. Menale, C. *et al.* MSC-Seeded Biomimetic Scaffolds as a Factory of Soluble

RANKL in Rankl-Deficient Osteopetrosis. *Stem Cells Transl. Med.* 1–13 (2018). doi:10.1002/sctm.18-0085

101. Tampieri, A. *et al.* HA/alginate hybrid composites prepared through bio-inspired nucleation. *Acta Biomater.* **1,** 343–351 (2005).

102. Panseri, S. *et al.* Biomimetic Scaffold with Aligned Microporosity Designed for Dentin Regeneration. *Front. Bioeng. Biotechnol.* **4,** 48 (2016).

103. Mohammed, L., Gomaa, H. G., Ragab, D. & Zhu, J. Magnetic nanoparticles for environmental and biomedical applications: A review. *Particuology* **30,** 1–14 (2017).

104. Iafisco, M. *et al.* Superparamagnetic iron-doped nanocrystalline apatite as a delivery system for doxorubicin. *J. Mater. Chem. B* **4,** 57–70 (2016).

105. Singh, N., Jenkins, G. J. S., Asadi, R. & Doak, S. H. Potential toxicity of superparamagnetic iron oxide nanoparticles (SPION). *Nano Rev.* **1,** 5358 (2010).

106. Feuser, P. E. *et al.* Encapsulation of magnetic nanoparticles in poly(methyl methacrylate) by miniemulsion and evaluation of hyperthermia in U87MG cells. *Eur. Polym. J.* **68,** 355–365 (2015).

107. Thomas, S. Iron Oxide Biomagnetic Nanoparticles (IO-BMNPs); Synthesis, Characterization and Biomedical Applicationâ“A Review. *Journal of Nanomedicine & Nanotechnology* **8,** 1–9 (2017).

108. Campodoni, E. *et al.* Development of innovative hybrid and intrinsically magnetic nanobeads as a drug delivery system. *Nanomedicine (Lond)* **11,** 2119–2130 (2016).

109. Mohammed, L. & Gomaa, D. R. and H. Bioactivity of Hybrid Polymeric Magnetic Nanoparticles and Their Applications in Drug Delivery. *Current Pharmaceutical Design* **22,** 3332–3352 (2016).

110. Panseri, S. *et al.* Intrinsically superparamagnetic Fe-hydroxyapatite nanoparticles positively influence osteoblast-like cell behaviour. *J. Nanobiotechnology* **10,** 32 (2012).

111. Panseri, S. *et al.* Magnetic labelling of mesenchymal stem cells with iron-doped hydroxyapatite nanoparticles as tool for cell therapy. *J. Biomed. Nanotechnol.* **12,** 909–921 (2016).

112. Grace, K. L., Revell, W. J. & Brookes, M. The effects of pulsed electromagnetism on fresh fracture healing: osteochondral repair in the rat femoral groove. *Orthopedics* **21,** 297–302 (1998).

113. Assiotis, A., Sachinis, N. P. & Chalidis, B. E. Pulsed electromagnetic fields for the treatment of tibial delayed unions and nonunions. A prospective clinical study and review of the literature. *J. Orthop. Surg. Res.* **7,** 24 (2012).

114. Hassan, E. E., Parish, R. C. & Gallo, J. M. Optimized Formulation of Magnetic Chitosan Microspheres Containing the Anticancer Agent, Oxantrazole. *Pharmaceutical Research: An Official Journal of the American Association of Pharmaceutical Scientists* **9,** 390–397 (1992).

115. Liu, G., Gao, J., Ai, H. & Chen, X. Applications and potential toxicity of magnetic iron oxide nanoparticles. *Small* **9,** 1533–1545 (2013).

116. Iannotti, V. *et al.* Fe-Doping-Induced Magnetism in Nano-Hydroxyapatites. *Inorg. Chem.* **56,** 4446–4458 (2017).

117. Iafisco, M. *et al.* Magnetic Bioactive and Biodegradable Hollow Fe-Doped Hydroxyapatite Coated Poly(l-lactic) Acid Micro-nanospheres. *Chem. Mater.* **25,** 2610–2617 (2013).

118. De Santis, R. *et al. Towards the Design of 3D Fiber-Deposited Poly(-caprolactone)/Iron-Doped Hydroxyapatite Nanocomposite Magnetic Scaffolds for Bone Regeneration*. *Journal of Biomedical Nanotechnology* **11,** (2015).

119. Fernandes Patr??cio, T. M., Panseri, S., Sandri, M., Tampieri, A. & Sprio, S. New bioactive bone-like microspheres with intrinsic magnetic properties obtained by bio-inspired mineralisation process. *Mater. Sci. Eng. C* **77,** 613–623 (2017).

120. Tampieri, A. *et al.* Magnetic bioinspired hybrid nanostructured collagen-hydroxyapatite scaffolds supporting cell proliferation and tuning regenerative

process. *ACS Appl. Mater. Interfaces* **6,** 15697–15707 (2014).

121. Lewis, P. L., Green, R. M. & Shah, R. N. 3D-printed gelatin scaffolds of differing pore geometry modulate hepatocyte function and gene expression. *Acta Biomater.* **69,** 63–70 (2018).

122. Sprio, S., Sandri, M., Panseri, S., Cunha, C. & Tampieri, A. Hybrid scaffolds for tissue regeneration: Chemotaxis and physical confinement as sources of biomimesis. *J. Nanomater.* **2012,** (2012).

123. Montesi, M. & Panseri, S. in *Bio-Inspired Regenerative Medicine* 283–304 (Pan Stanford, 2016). doi:doi:10.1201/b19914-12

124. Eiselt, P., Yeh, J., Latvala, R. K., Shea, L. D. & Mooney, D. J. Porous carriers for biomedical applications based on alginate hydrogels. *Biomaterials* **21,** 1921–1927 (2000).

125. Mondragon, G., Peña-Rodriguez, C., González, A., Eceiza, A. & Arbelaiz, A. Bionanocomposites based on gelatin matrix and nanocellulose. *Eur. Polym. J.* **62,** 1–9 (2015).

126. Anjaneyulu, U., Priyadarshini, B., Nirmala Grace, A. & Vijayalakshmi, U. Fabrication and characterization of Ag doped hydroxyapatite-polyvinyl alcohol composite nanofibers and its in vitro biological evaluations for bone tissue engineering applications. *J. Sol-Gel Sci. Technol.* **81,** 750–761 (2017).

127. Gomes, S. R. *et al.* In vitro and in vivo evaluation of electrospun nanofibers of PCL, chitosan and gelatin: A comparative study. *Mater. Sci. Eng. C* **46,** 348–358 (2015).

128. Campodoni, E. *et al.* Polymeric 3D scaffolds for tissue regeneration: Evaluation of biopolymer nanocomposite reinforced with cellulose nanofibrils. *Mater. Sci. Eng. C* **94,** 867–878 (2019).

129. Zhang, Y. S. *et al.* 3D Bioprinting for Tissue and Organ Fabrication. *Ann. Biomed. Eng.* **45,** 148–163 (2017).

130. Zhang, H., Dicker, K. T., Xu, X., Jia, X. & Fox, J. M. Interfacial bioorthogonal

cross-linking. *ACS Macro Lett.* **3,** 727–731 (2014).

131. Yuan, Y. *et al.* The effect of cross-linking of chitosan microspheres with genipin on protein release. *Carbohydr. Polym.* **68,** 561–567 (2007).

132. Nicoletti, A. *et al.* Effects of different crosslinking conditions on the chemical-physical properties of a novel bio-inspired composite scaffold stabilised with 1,4-butanediol diglycidyl ether (BDDGE). *J. Mater. Sci. Mater. Med.* **24,** 17–35 (2013).

133. Ninh, C., Iftikhar, A., Cramer, M. & Bettinger, C. J. Diffusion–reaction models of genipin incorporation into fibrin networks. *J. Mater. Chem. B* **3,** 4607–4615 (2015).

134. Haugh, M. G., Jaasma, M. J. & O'Brien, F. J. The effect of dehydrothermal treatment on the mechanical and structural properties of collagen-GAG scaffolds. *J. Biomed. Mater. Res. - Part A* **89,** 363–369 (2009).

135. Madaghiele, M. *et al.* Assessment of collagen crosslinking and denaturation for the design of regenerative scaffolds. *J. Biomed. Mater. Res. - Part A* **104,** 186–194 (2016).

136. Geng, Z. *et al.* Incorporation of silver and strontium in hydroxyapatite coating on titanium surface for enhanced antibacterial and biological properties. *Mater. Sci. Eng. C* **71,** 852–861 (2017).

137. Li, Y. *et al.* The effect of strontium-substituted hydroxyapatite coating on implant fixation in ovariectomized rats. *Biomaterials* **31,** 9006–9014 (2010).

138. Russo, A. *et al.* Bone regeneration in a rabbit critical femoral defect by means of magnetic hydroxyapatite macroporous scaffolds. *J. Biomed. Mater. Res. - Part B Appl. Biomater.* **106,** 546–554 (2018).

139. Stavros, V. G. Photochemistry: A bright future for sunscreens. *Nat. Chem.* **6,** 955–956 (2014).

140. Gasparro, F. P., Mitchnick, M. & Nash, J. F. A Review of Sunscreen Safety and Efficacy. *Photochem. Photobiol.* **68,** 243–256 (1998).

141. Serpone, N., Dondi, D. & Albini, A. Inorganic and organic UV filters: Their role and efficacy in sunscreens and suncare products. *Inorganica Chim. Acta* **360,** 794–802 (2007).

142. Shen, B., Scaiano, J. C. & English, A. M. Zeolite Encapsulation Decreases TiO2-photosensitized ROS Generation in Cultured Human Skin Fibroblasts†. *Photochem. Photobiol.* **82,** 5 (2006).

143. Piccirillo, C. *et al.* A hydroxyapatite-Fe2O3based material of natural origin as an active sunscreen filter. *J. Mater. Chem. B* **2,** 5999–6009 (2014).

144. De Araujo, T. S., De Souza, S. O. & De Sousa, E. M. B. Effect of Zn2+, Fe3+and Cr3+addition to hydroxyapatite for its application as an active constituent of sunscreens. *J. Phys. Conf. Ser.* **249,** (2010).

145. Janib, S. M., Moses, A. S. & MacKay, J. A. Imaging and drug delivery using theranostic nanoparticles. *Adv. Drug Deliv. Rev.* **62,** 1052–1063 (2010).

146. Sun, W. *et al.* Biodegradable Drug-Loaded Hydroxyapatite Nanotherapeutic Agent for Targeted Drug Release in Tumors. *ACS Appl. Mater. Interfaces* **10,** 7832–7840 (2018).

2. Materials&Methods

2.1. Materials

In this Ph.D. research several reagents and polymers were used as reported below. Type I collagen (Coll) extracted from equine tendon, purified and telopeptide-free, and supplied as acetic gel (an aqueous acetic buffer solution with pH = 3.5 containing 1 wt% of pure collagen) was purchased from Opocrin S.p.A., Italy. Type A Gelatin was received by Italgelatine (Italy), it was extracted form pig skin and produced with mesh 4 and bloom 280. Cellulose nanofibrils (CNF) were produced form PFI (Trondheim, Norway) and received as about 1 wt% aqueous suspension. Calcium hydroxide ($Ca(OH)_2$; ≥95.0% pure), sodium hydroxide (NaOH; ≥98% pure), chloridric acid (HCl; 37% pure), solforic acid (H_2SO_4; 95-98% pure), acetic acid (CH_3COOH; ≥99.7% pure), nitric acid (HNO_3; 65% pure), magnesium chloride hexahydrate ($MgCl_2{\cdot}6H_2O$; ≥99% pure), iron(III) chloride hexahydrate ($FeCl_3{\cdot}6H_2O$; 97% pure), iron(II) chloride tetrahydrate ($FeCl_2{\cdot}4H_2O$; ≥99% pure), calcium chloride ($CaCl_2$; ≥97% pure), phosphate buffered saline (PBS; pH 7.4), 4-butanediol diglycidyl ether (BDDGE; 95 wt.% pure) and 2,4,6-trinitrobenzenesulfonic acid (TNBS; 1 M in H2O) were all provided by Sigma-Aldrich. Low molecular weight chitosan (degree of deacetylation between 80-85%), medium molecular weight chitosan (degree of deacetylation between 75-85%), high molecular weight chitosan (>75% deacetylated), sodium alginate were purchased from Sigma-Aldrich. Genipin (98 wt.% pure) was purchased from Wako Chemicals (USA).

2.2. Materials processing

Freeze-drying techniques. All synthetized materials were manufactured by unidirectional freeze-drying technology (see chapter 1.4). If do no differently mentioned, the freezing ramp was 50 °C/min until -40 °C and heating ramps were performed from -40 °C to -10°C at 5 °C/h and from -10 °C to 15 °C at 2 °C/h under vacuum conditions (at least P = 0.1 mbar). The equipment employed in the present work was a 5Pascal LIO-1000P.

2.3. Analytical techniques

All analytical techniques exploited in this Ph.D. research are the same of a thesis previously published. The principles of techniques and the sample preparation are reported below according to previous thesis.[1]

2.3.1. X-Ray Diffraction (XRD)

X-ray diffraction (XRD) is a non-destructive analytical technique primarily used for phase identification of a crystalline material. The material is finely ground, homogenized and the average bulk phase composition is analysed.

An X-ray beam hit a sample and the scattered intensity was evaluated as a function of incident and scattered angle, polarization and wavelength or energy. X-ray wavelength is comparable with inter-atomic distances (~150 pm) and thus is an excellent probe for this length scale. This technique is commonly used to evaluate heterogeneous solid mixed substance to determine their relative amount or to recognize unknown substances, by comparing diffraction data against a database of International Center for Diffraction Data (ICDD). Powder diffraction is also a common method for determining strains in crystalline materials. A simple preparation, a fast analysis on single or mixed phase are the advantages of this technique.

The X-ray wavelength (λ between 10 nm and 1 pm) is generated by a cathode ray tube, filtered to produce monochromatic radiation, collimated to concentrate that hits the sample. When it hits an atom, the electrons around the atom start to oscillate with the same frequency as the incoming beam. As consequence of the oscillation the electrons will diffuse the incidence radiation in all the directions; this phenomenon is known as the Rayleigh scattering (or elastic scattering). These kind of radiations interfere with each other destructively in the most of the directions, but also in a constructive way if some atoms are arranged in a regular pattern (crystalline cell) and a diffracted ray is produced because the Bragg’s law is satisfied (Figure 2.1). Miller indices (hkl) were usually used to indicate which of the various intersection planes of the mineral’s crystal cell refers the constructive interference (dhkl: interplanar distance).

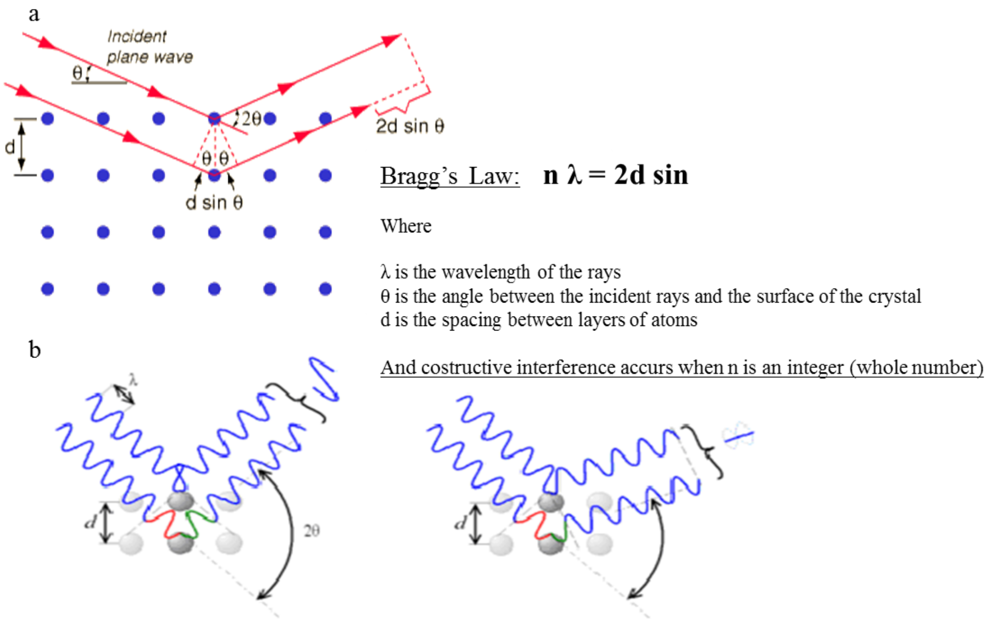

Bragg's Law: **n λ = 2d sin**

Where

λ is the wavelength of the rays
θ is the angle between the incident rays and the surface of the crystal
d is the spacing between layers of atoms

And costructive interference accurs when n is an integer (whole number)

Figure 2.1. a) Bragg's law and constructive interference; b) difference between constructive (on the left) and destructive interference in Rayleigh scattering of X-rays.

The overlapping waves will give rise a well-defined scattered X-ray beams leaving the sample at various directions. In the diffraction analysis, the wave interference pattern was shown as diffracted intensity in function of diffraction angle (2θ), each single phase or materials show a typical pattern with specific positions and relative intensity of the lines. In contrast to a crystalline pattern consisting of a series of sharp peaks, amorphous materials produce a broad background signal. Many polymers, organic molecules or inorganic glasses usually exhibit this kind of pattern, but often also inorganic nanostructured crystalline phases can contain also an amorphous fraction. X-ray diffractometers is composed by three basic elements:

- X-ray tube: a cathod tube generates X-ray by heating a filament and producing electrons. A voltage applied accelerates electron toward a target that reach and hit material (Figure 2.2);

- a sample holder;

- X-ray detector. The most focusing geometry used in powder diffractometers is the Bagg-Brentano were the incident beam produced and the detector move on a circle where sample in the center.

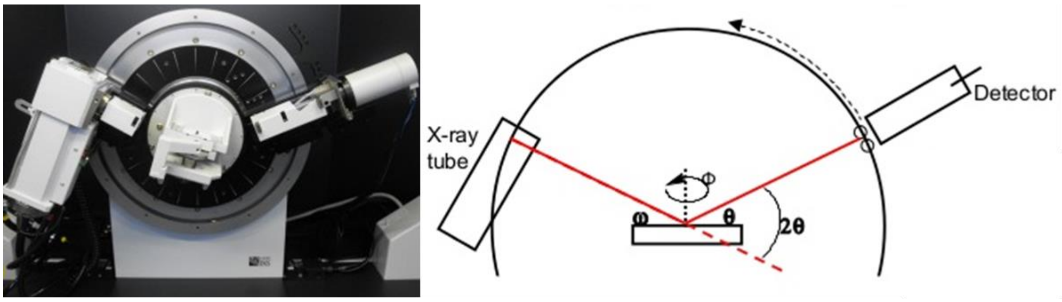

Figure 2.2. D8 Advance diffractometer (on the left) and a typical scheme of a Bragg-Brentano type diffractometer (on the right).

The model of diffractometer employed in this activity is a D8 Advance diffractometer (CuKα radiation) working with Bragg-Brentano configuration, equipped with a LINXEYE detector (Bruker, Karlsruhe, Germany). The XRD patterns were recorded in the 2θ range 10°-80°, scan step 0.02° and step time 0.5 seconds.[1]

2.3.2. Fourier-Transform Infrared Spectroscopy (FTIR)

Among spectroscopy techniques, Infrared spectroscopy deals with the region of the electromagnetic spectrum ranging from 14000 to 10 cm^{-1} (from near to far-IR). The signal is acquired in the time domain, and through the Fourier transform it's possible to obtain the spectrum in function of frequencies.

Infrared spectroscopy exploits the fact that at specific frequencies the interaction with the radiation causes vibrational transitions (Figure 2.3). The strength of the bond, the mass of the atoms and also its around determine different absorption frequencies. Thus, each particular bond type shows a specific frequency and intensity of absorption and can be used for the characterization of very complex mixtures.

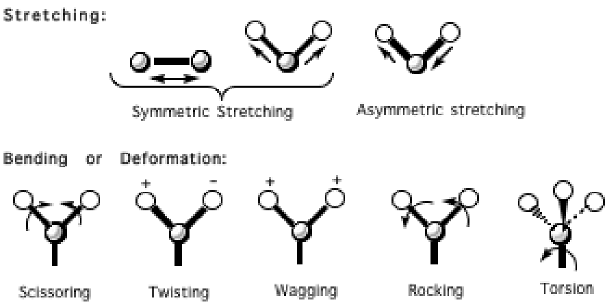

Figure 2.3. Possible vibrations detected by infrared spectroscopy.

In the FTIR instrument a beam of infrared light goes through an interferometer and onto the sample absorbing all the different wavelengths characteristic of its spectrum at once. Instead, in standard IR spectrometer with a monochromater the source radiation is separated into its different wavelengths limiting the amount of signal which can be obtained at a particular resolution. In FTIR instrument, all wavelengths are simultaneously reported thank to the beam splitter which send the light through moving and stationary mirrors the beam passing through the sample (Figure 2.4).

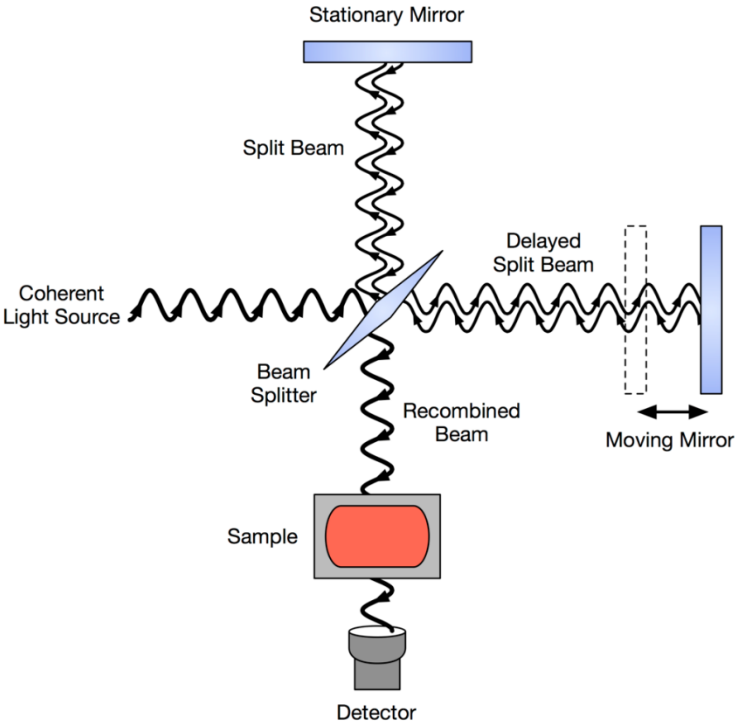

Figure 2.4. Scheme of FTIR spectrometer.

During preparation about 2 mg of the sample is ground finely with 100 mg of anhydrous potassium bromide (KBr) to remove scattering effects from large crystals. This powder mixture is then pressed at 8000 psi into 7 mm diameter disc to form a translucent pellet through which the beam of the spectrometer can pass through. All the spectra are the average of 64 spectra, acquired at room temperature in the range of 400-4000 cm^{-1} at a resolution of 4 cm^{-1}; potassium bromide is used as control.

The equipment employed in the present work was a Thermo Nicolet-Avatar 320 FT-IR (Thermo Fisher Scientific Inc., Waltham, MA, USA). [1]

2.3.3. Inductively Coupled Plasma Optical Emission Spectroscopy (ICP-OES)

The Inductively Coupled Plasma Optical Emission Spectroscopy (ICP-OES) is one of the most powerful and popular analytical tools for the determination of trace elements. A spontaneous emission of photons from atoms and ions that have been excited in a radiofrequency (RF) discharge is the source of this technique where the sample can be directly injected in liquid or gas form. Instead, solid samples require extraction or acid digestion so that the analytes will be present in a solution. Standard solutions allow to create a calibration curve in order to evaluate the concentration of the elements that are proportional to the intensity of the radiation. A torch that is composed of three concentric tubes, usually made of quartz, keeps the plasma. The end of this torch is placed inside an induction coil supplied with a radio-frequency electric current. A flow of argon gas is introduced between the two outermost tubes of the torch and an electrical spark is applied for a short time and free electrons are introduced into the gas stream (Figure 2.5).

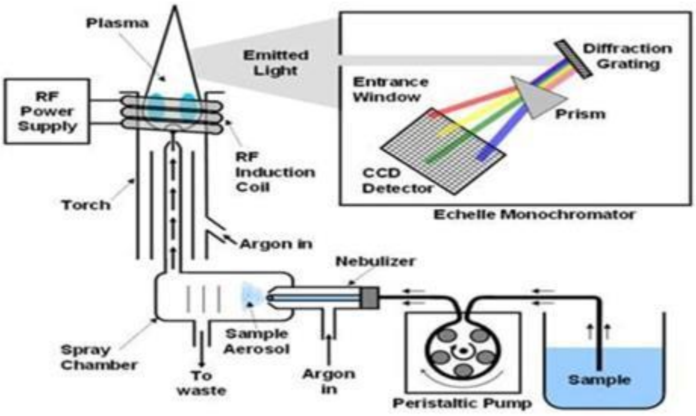

Figure 2.5. Schematic view of ICP-OES spectrometer.

Before entering in middle channel of plasma, the sample solution is converted into an aereosol and after is quickly vaporized due to the inductively coupled plasma (ICP) kept a temperature of approximately 10000K. In this way, sample is converted in free atoms in the gaseous state. Further collisional excitation within the plasma imparts additional energy to the atoms, promoting them to excited states. Sufficient energy is often available to convert the atoms to ions and subsequently promote the ions to excited states. Both the atomic and ionic excited species may then relax to the ground state via the emission of photons. These photons have characteristic energies that are determined by the quantized energy level structure for the atoms or ions. Elaborating the wavelength of the photons, the starting elements can be recognized and their concentrations is directly proportional to the amount of photon.

The equipment employed in the present work was a Liberty 200, Varian (Clayton South, Australia); 20 mg of sample was dissolved in 2 mL of nitric acid (HNO_3) and deionized water was added up to 100 mL. Standard solutions of investigated atoms was used as reference solutions and an equally diluted solution of nitric acid was also analysed and the corresponding spectrum subtracted by the experimental one.[1]

2.3.4. Thermogravimetric analysis (TGA)

Thermogravimetric analysis is a useful test to determine changes in weight in relation to change in temperature. Such analysis relies on a high degree of precision in three measurements: weight, temperature, and temperature change. As many weight loss curves look similar, the weight loss curve may require transformation before results may be interpreted. A derivative weight loss curve can be used to tell the point at which weight loss is most apparent. The instrument is composed of a high-precision balance with a pan loaded with the sample. The sample is placed in a small electrically heated oven with a thermocouple to accurately measure the temperature. Different gas can be used such as air, argon, nitrogen to prevent oxidation or other undesired reactions. During analysis, temperature is gradually increased and weight is measured and plotted against temperature. After the data is obtained, some tools can be used to elaborated curves. The equipment employed in the present work was the Simultaneous Thermal Analyser (STA 409C, Netsch, Germany).[1]

2.3.5. Scanning Electron Microscopy (SEM)

The scanning electron microscope is a device able to provide high magnification images of a sample (up to 200000X) with both resolution and field depth higher than the conventional optical microscope. The characteristic of the instrument is to explore the surface of the sample with a beam of high-energy electron, while a real-time monitoring of the intensity of the emitted secondary electrons is performed. Afterward, several signals are detected from the interaction of the incident electrons with the sample's surface (Figure 2.6).

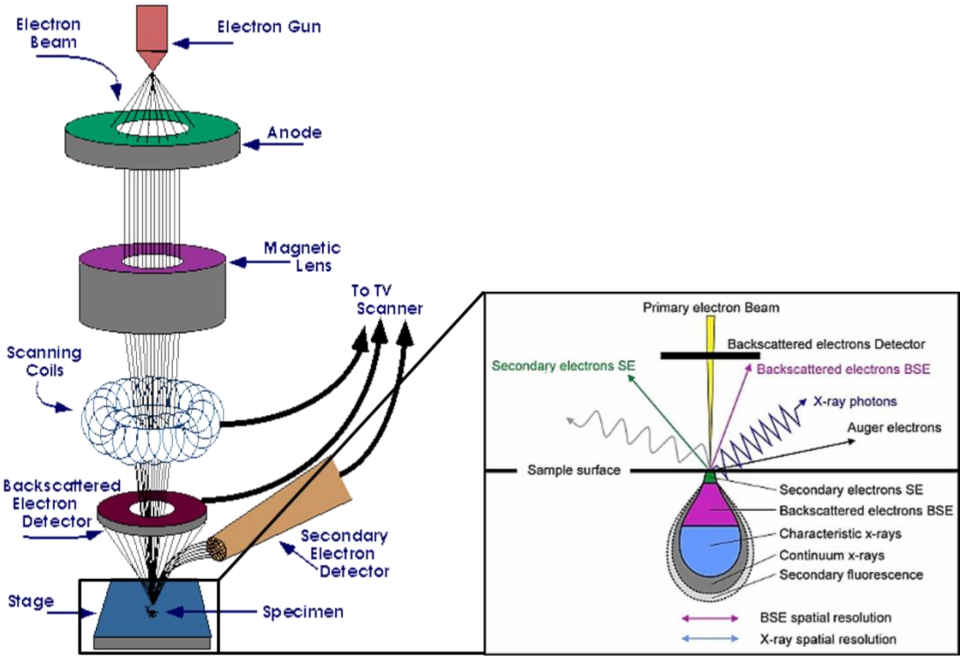

Figure 2.6. Schematic view of a SEM; in the inset, the electron-matter interaction was shown.

Part of the incident electron beam (primary electrons) is reflected without decreasing the initial energy, giving rise to backscattered electrons. Secondary electrons are specific electron which escape outside of the sample because they are able to diffuse toward the surface thank to the energy received by primary electrons. In particular, only primary electrons that are not reflected; and the secondary electron escape with a low energy (energy < 50 eV). Furthermore, characteristic x-ray photons are emitted when the primary beam causes the expulsion of inner shell electrons from the sample and are used to investigate the elemental composition of the sample. Finally, back-scattered electrons emitted from the sample may be used alone to form an image or in conjunction with the characteristic x-rays as atomic number contrast clues to the elemental composition of the sample.

In a typical SEM, the source is a tungsten cathode (electron gun), used because has high melting point and low vapour pression, that generates electrons and it is accelerated towards an anode. Before hitting the sample, the electron beam is focused by condenser lenses and passes through pairs of scanning coils or pairs of deflector plates in the electron optical column and it is endowed by a fine focal spot sized 0.4 nm to 5 nm and an energy of few hundred eV up to 100 KeV. Electron beam, the atomic number of the specimen and its density determines the interaction volume. The secondary electrons, due to their low energy, are detected by a scintillator photomultiplier device and the resulting signal is rendered into a two-dimensional intensity distribution that can be viewed and saved as a digital image. The number of electrons secondary in the detector and the size of the electron spot determine the brightness and the spatial resolution respectively. Furthermore, the size of the electron spot depends on both the wavelength of the electrons and the magnetic electron optical system which produces the scanning beam.

The equipments employed in the present work were two a FEG-SEM (Field Emission Gun Scanning Electron Microscope) for high resolution images at high magnification (FEI, Quanta 200, USA) and ESEM (Environmental Scanning Electron Microscope) for high resolution imagines at low magnification (Quanta 600 FEG, FEI Company, Hillsboro, OR). For SEM analyses the specimens were previously mounted on aluminum stubs with carbon tape and coated with Au using a coating units Polaron Sputter Coater E5100 (Polaron Equipment, Watford, Hertfordshire, UK).[1]

2.3.6. Transmission Electron Microscopy (TEM)

Transmission electron microscope (TEM) utilizes electrons instead of light as “light source” and their much lower wave length makes it possible to get a visual resolution a thousand times better than with a light microscope. TEM allows seeing objects to the order of a few angstroms (10^{-10}m) even as small as a single column of atoms. TEM is utilized in medical, biological and material science research.

A source at the top of the TEM emits electrons that travel through vacuum in the column of the microscope. Instead of glass lenses focusing the light in the light microscope, the TEM uses electromagnetic lenses to focus the electrons into a very thin beam, which then travels through the specimen. The transmission of electron beam is highly dependent on the properties of material being examined such as density, composition, etc. Porous material allows more electrons to pass through while dense material allows fewer electrons to pass through. As a result, a specimen with a non-uniform density can be examined with the help of TEM. The part that is transmitted is projected onto a fluorescent screen, which gives rise to a “shadow image” of the specimen with its different parts displayed in varied darkness according to their density. The image can be processed on a layer of photographic film, or detected by a sensor such as a CCD camera.

A TEM has four main parts: electron source, electromagnetic lens system, sample holder, and imaging system (Figure 2.7). The electron source comprises of a cathode and an anode. The cathode is a tungsten filament which emits electrons when it is heated. The beam is accelerated in the direction of the specimen by the positive anode. Electrons at the rim of the beam will fall onto the anode while the others at the center will pass through the small hole of the anode. The electron source works like a cathode ray tube.

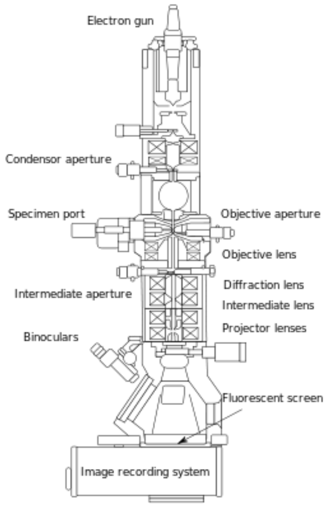

Figure 2.7. A schematic view of TEM microscope.

After leaving the electron source, electromagnetic lenses are used to accelerate and focus the electrons into a very thin beam by varying the magnetic field of electromagnetic lenses. The imaging system consists of another electromagnetic lens system and a screen. The other electromagnetic lens system is for enlarging the image and projecting it onto the screen. The screen has a phosphorescent plate which glows on being hit by electrons. The image forms in a similar manner to that of photography.

The specimen must be of such a low density that it allows electrons to travel through the tissue. There are different ways to prepare the specimen for study. Very thin slices can be cut of the specimen from a piece of the material either by fixing it in plastic or working with it as frozen material. Another way to prepare the specimen is to isolate it and study a solution (e.g. viruses or molecules) in the TEM. Materials such as powders or nanotubes, can be quickly prepared by the deposition of a dilute sample containing the specimen onto support grids. One can stain the specimen in different ways and use markers to locate specific features in the sample. It can be stained using negative staining material including heavy metals such as uranium and lead, which scatters electrons well and improves the image contrast in the microscope.

The equipment employed in the present work was a Tecnai F20 (FEI, 124 Hillsboro, USA) equipped with a Schottky emitter and operating at 120 and 200 keV.

2.3.7. Dinamic light scattering (DLS) and Z potential

Dynamic light scattering (also known as photon correlation spectroscopy (PCS) or quasi-elastic light scattering (QELS)) is one of the most popular technique used to determine the size and size distribution of molecules or particles in the submicron region. DLS can be used to measure particles in the size range from 3 nm to several microns.

Brownian motion is the random movement of particles due to the bombardment by the solvent molecules that surround them. The larger the particle, the slower the Brownian motion (Figure 2.8). In order for the Brownian motion to be considered truly random, the temperature must be stabilized to prevent convection currents from influencing the movement. Similarly, the solvent viscosity will also play a vital role and needs to be factored into the final calculation of particle diameter. DLS does not measure actual physical particle size, but rather the effective particle diameter in its local environment. This effective diameter, known as the hydrodynamic diameter, can be calculated from the following Stokes-Einstein Equation. From the Stokes-Einstein Equation, the hydrodynamic diameters dependency on the particles translational diffusion (velocity), as well as the solvent viscosity and temperature is clear. In essence the hydrodynamic diameter refers to how a perfectly spherical particle diffuses within a fluid and in cases where the particle is non-spherical an equivalent sphere of the same diffusion coefficient is assumed.

$$d(H) = \frac{kT}{3 \times \pi \times \eta \times D}$$

Stokes – Einstein Equation

where:
d(H) = hydrodynamic diameter
D = translational diffusion coefficient
k = Boltzmann’s constant
T = absolute temperature
η = viscosity

The DLS instrument comprises of a laser source, laser delivering optics, sample holder, scattered light collecting optics, photon detector, and autocorrelator (AC). A schematic diagram of the instrument is shown in figure 2.8. A monochromatic He-Ne laser of a known wavelength is passed through a dilute sample. The random movement of sample particles produces constructive and destructive interferences in the scattered laser light. This creates fluctuations in the intensity of scattered light with time. The light collecting optics collects the scattered light at a specific angle. The intensity fluctuations of the scattered light are converted into electrical pulses using an avalanche photodiode detector or photomultiplier tube. These are fed into a digital correlator, which generates the autocorrelation function, from which the appropriate data analysis is performed.

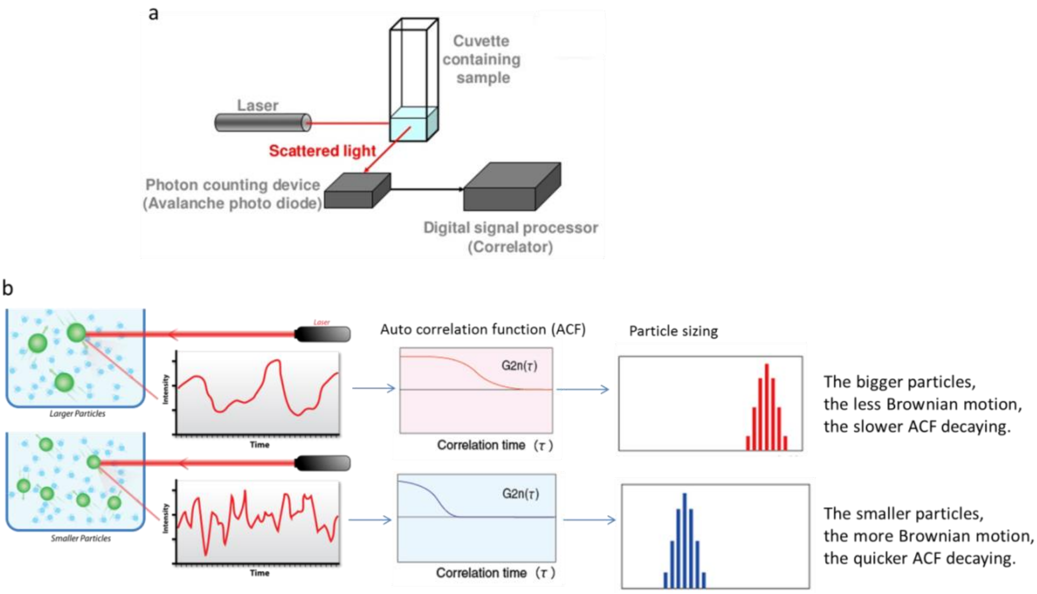

Figure 2.8. a) Schematic view of DLS; b) schematic representation of Brownian motion of different particles and respective correlation function and size particles spectra.

Several parameters such as solvent viscosity, refractive index, and sample temperature affect the measurements by DLS. Diluted samples should be used to suppress inter particulate interactions. The scattering intensity depends on the mass of the particles, its concentrations and differences in the refractive index of the particle and the solvent. Air bubbles and dust particles may be removed by ultrasonication, centrifugation, or filtration. Sample holders and cuvettes should be thoroughly cleaned and dried before placing the sample.

The equipment employed in the present work was a Zetasizer Nano ZS (Malvern Ltd., UK). Samples were suspended in water at a concentration of 0.1 mg/mL. For the measurement of the size distribution, low-volume quartz cuvettes (105.251-QS, Hellma, Germany) were used. Ten runs of 30 s each were performed for each measurement and four measurements were carried out for each sample.

Zeta potential is the measure of the stability of a colloid system. In an ionic solution, nanoparticles with a net charge will have two surrounding layers: a layer of ions of opposite charge strongly bound to their surface, and a diffuse outer layer of loosely associated ions. These two layers are collectively called the electrical double layer. As the particle moves, a distinction is created between ions in the diffuse layer that move with the nanoparticle and ions that remain with the bulk dispersant. The electrostatic potential at this “slipping plane” boundary is called the zeta potential and is related to the surface charge of the nanoparticle. In zeta potential measurements, an electrical field is applied across the sample and the electrophoretic mobility of nanoparticles is measured by laser Doppler velocimetry (Figure 2.9).

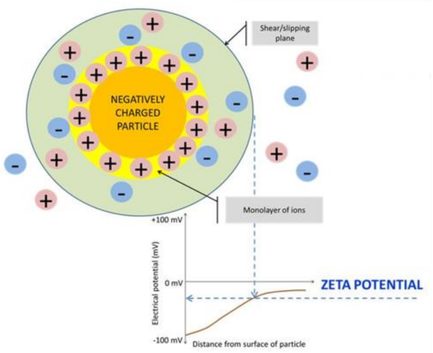

Figure 2.9. Zeta-potential scheme

In general, if all particles in suspension have a large negative or positive Z potential, they will tend to repel each other and there is no tendency to flocculate (process of reversible aggregation of particles). However, if particles have a low ZP value, there is no force to prevent the particles coming together and flocculating. The dividing line between stable and unstable suspensions is generally taken at zeta potentials of either +30mV or - 30mV. Particles with Zeta potentials more positive than +30mV or more negative than - 30mV are normally considered stable, as summarized in table 2.1.

Table 2.1 Colloidal behavior and related Zeta Potential values.

Zeta potential [mV]	**Stability behavior of the colloid**
From 0 to ± 5	Rapid coagulation or flocculation
From ± 10 to ± 30	Incipient instability
From ± 30 to ± 40	Moderate stability
From ± 40 to ± 60	Good stability
More than ± 61	Excellent stability

The equipment employed in the present work was a Zetasizer Nano ZS (Malvern Ltd., UK). Samples were suspended in water at a concentration of 0.1 mg/mL. For the measurement of the Zeta-potential a disposable electrophoretic cell (DTS1061, Malvern Ltd., UK) was used. Twenty runs of 3 s each were collected in each measurement.

2.4. Characterization methods of scaffolds

2.4.1. Pore size and porosity

Scanning electron microscopy (SEM) was exploited to evaluate the morphology of the scaffolds which are mounted onto aluminum stubs using black carbon tapes and sputter coated with gold (Sputter Coater Q150TES, Quorum, Italy). The specimen surface was examined using high resolution SEM (FEI, Quanta 200, UK) at a pressure of 0.1 m Torr at an accelerating voltage of 10 kV.

The scaffold porosity was evaluated by two different methods: the density method and the water squeezing method.

The density method measures the scaffold density with weight and volume of dried scaffold; and from the scaffold density, the porosity is calculated.[2] Firstly, the density of the scaffold (ρ) was determined with the following equation:

$$\rho = \frac{W}{V}$$

where

W is the weight of the scaffold,
V is the volume of the scaffold (depending on its shape).

The density was divided by theoretical density of the material determined from the different weight fraction (Xi) and the different theoretical density of the reagents:

$$\rho_{\text{theoretical}} = \left(\rho_{\text{theoretical(A)}} \times X_A\right) + \left(\rho_{\text{theoretical(B)}} \times X_B\right)$$

Finally, the total porosity of the scaffolds was calculated as described in the equation below.

The values were expressed as the mean ± standard error and the number of replicates (n) was three (n=3).

$$\text{total porosity (\%)} = 100 - \left(\frac{\rho}{\rho_{\text{theoretical}}} \times 100\right)$$

<u>The water squeezing method</u> measures the amount of water inside a scaffold before and after scaffold squeezing.[3] The method is based on the principle that the water is present in small and big pores inside the polymer network. The water in its latter form is relatively free and represents the porosity requirement for the cell penetration and proliferation. The method measures the macropores volume percentage with the following procedure: the scaffold was equilibrated in deionized water for one hour and weighed (M_{swollen}), subsequently; it was squeezed to remove the water filling the pores and weighed again (M_{squeezed}). Macropores volume was calculated using the following equation:

$$\text{Macropores volume percentage} = \frac{(M_{\text{swollen}} - M_{\text{squeezed}})}{M_{\text{swollen}}} \times 100$$

The values were expressed as the mean ± standard error (n=3).

2.4.2. Wettability: contact angle

Static contact angle is widely used for a good knowledge of the solid–liquid interfacial tensions and to evaluate the wetting behavior of water or other solvents on a surface.

The angle formed by a liquid at the three-phase boundary where a liquid, gas and solid intersect geometrically defines the contact angle measurement. A fixed amount of specific solvent was dropped on a solid sample and the tangent angle is directed measurement. A sample endowed with high wettability records small contact angles ($\theta<90°$), while a sample with large contact angles ($\theta>90°$) records low wettability (Figure 2.10).

The water affinity was tested using the static contact angle on the materials in the form of non-porous films that can be produced by casting wet materials on microscope slices and dried at room temperature. In our experiments, 1 µl of distilled water was dropped onto the surface of the films and the static contact angle of the drops were measured using a tensiometer Video-Based Optical Contact Angle Meter OCA 15+, Innovent (Germany). The values were expressed as the mean ± standard error (n=10). [1]

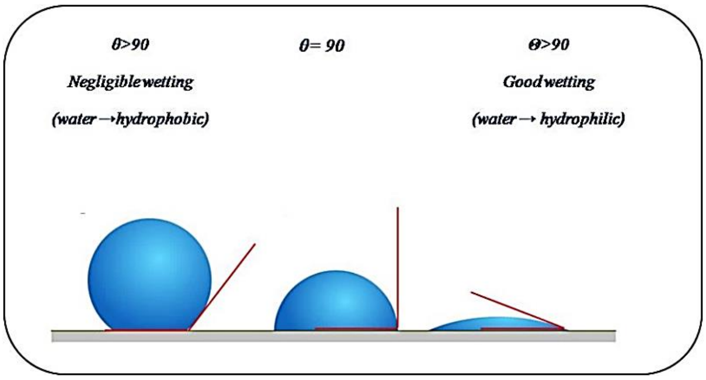

Figure 2.10. Possible contact angles formed by sessile liquid drops on a surface.

2.4.3. Swelling and degradation test

For the evaluation of the swelling degree cylindrical samples (Ø = 9 mm, h = 4mm) were weight and put in phosphate buffered saline solution (pH 7.4) at 37° in a shaking incubator.[4] At various times, samples were drained superficially by gentle contact with a filter paper and weighed again. The swelling percentage was calculated as:

$$\text{Swelling (\%)} = \left(\frac{\text{Wt} - \text{Wo}}{\text{Wo}}\right) \text{x } 100$$

where

Wi is the initial weight of dry sample
Ws is the sample weight after swelling.

For the degradation degree, at the same way, the samples were weighed and put in phosphate buffered saline solution (pH 7.4) at 37° in a shaking incubator.[5] At various times they were removed, freeze-dried and weighed again. The degradation degree, as percentage of weight remaining, was calculated as:

$$\text{Degradation (\%)} = \left(\frac{\text{Wo} - \text{Wd}}{\text{Wo}}\right) \text{x } 100$$

where

Wo is weight of dried sample before degradation test
Wd is weight of dried sample at the end of the degradation test.
The values were expressed as the mean ± standard error (n= 5). [1]

2.4.4. Amine cross-linking degree

In polymers that contain primary amine group, cross-linking degree can be evaluated measuring the primary amine residue content of a material.[5]

This method is based on the reaction of TNBS (2,4,6-trinitrobenzenesulfonic acid) with primary any primary amine compound, showed in Figure 2.11.

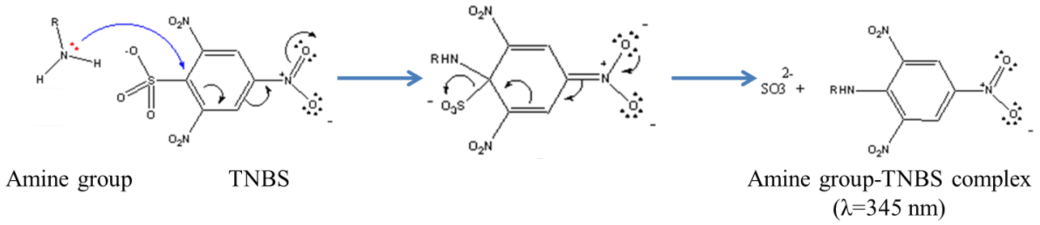

Figure 2.11. Reaction scheme of TNBS with a generic primary amine group.

TNBS undergoes a nucleophilic substitution reaction with amine compound replacing the sulphite group. TNBS reacts at alkaline pH with terminal α-amino groups as well as side-chain ε-amino groups and the reaction product strongly absorbs at 345 nm. No reaction takes place in an acidic medium, this is well suited for a blank. TNBS is added to the primary amine containing target molecule in a large excess that is respectively 10:1. Unreacted TNBS is masked by adding concentrated hydrochloric acid.

In our experiments, 5.0 mg of materials were added into 50 mL centrifuge tubes and 1 mL of $NaHCO_3$ 4 wt% was added. Afterwards, 1 mL of TNBS 0.5 wt% each were mixed and all the test tubes was shacked in a water bath at 40°C for 2 hours and then 3 mL of HCl 6M were added. Finally, all the test tubes were shacked in a water bath at 60°C for 4.5 hours and then cooled down to room temperature. The yellow solution was diluted 20 times before UV-Vis spectrometry analysis. All experiments were conducted in triplicate and blank sample was prepared in the same method without putting sample. A calibration curve allows to determine the concentration that is directly proportional to the absorbance of free primary amine. The non cross-linked material represent the 100% free amine standard while the cross-linking degree is evaluated subtracting the cross-linked sample absorbance to the non cross-linked sample absorbance.

The instrument used during this work was a Lambda 35 UV/VIS Spectrometer, Perkin Elmer Instrument (USA) and the spectra was collect from 200 to 800 nm at 240 nm/min.[1]

2.4.5. Magnetic measurements

In magnetic materials, free unpaired electrons give rise to magnetic forces which are attracted to a strong magnetic field, and the strength of these attractive forces are in direct proportion to the number of free electrons. During the magnetic susceptibility measurement, the interaction between a permanent magnet and the weight being tested is determined as a weight using a high-resolution mass comparator to estimate the magnetization vs magnetic field (M vs H) curve (Figure 2.12).

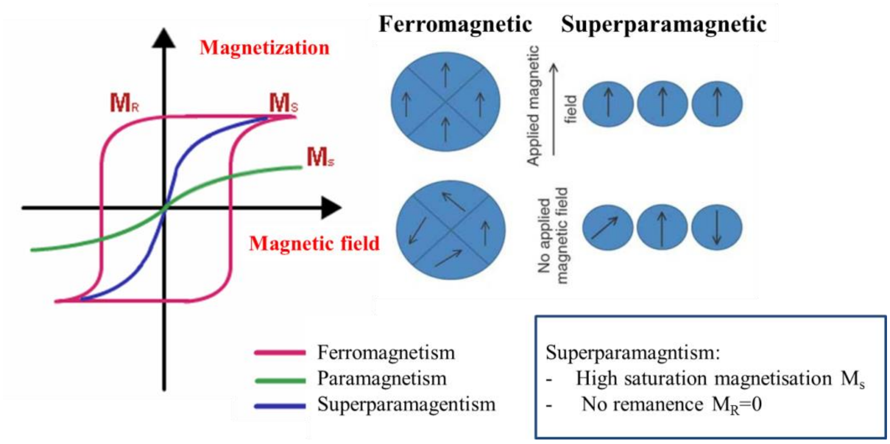

Figure 2.12 Magnetization curves for ferromagnetic, paramagnetic and superparamagnetic materials.

Magnetization measurements were performed in a Superconducting Quantum Interference Device (SQUID) magnetometer Quantum Design (San Diego, CA), operating at temperature of 1.8−350 K with a maxi-mum applied magnetic field (H) of 7T. About 20 mg of material were measured in a magnetic field cycle from −2T to +7T at temperature of 310 K (close to the physiological temperature).[1]

2.4.6. Dynamic mechanical analysis (DMA)

DMA is a simple mechanical analyser where an oscillating force is applied on to a sample and the material's response to force is measured. From the resultant mechanical behavior, the tendency to flow (viscosity) from the phase lag and the stiffness (modulus) from the sample response can be calculated. Basically, the visco-elastic properties of the materials under certain oscillating force is measured which is referred as the ability to lose energy as heat (damping) and the ability to recover from deformation (elasticity).

Several information is provided by DMA mechanical response such as elastic or Hookean behavior and viscous or Newtonian behavior. The Hooke's law states that the deformation or strain of the spring is linearly related to the constant force or stress (Figure 2.13). Which can be mathematically expressed as,

$F = k \cdot \Delta l$

where k is the spring constant. As the spring constant increases, the material becomes more stiff due to increase in the slope of the stress–strain curve, as well as the young's modulus also increases. The material's stiffness can be defined from the ratio of stress to strain.

$$E = \frac{\sigma}{\gamma}$$

where

σ is the stress that is the force applied by the instrument and related to sample's size:

$$\sigma = \frac{F}{A}$$

γ is the relative deformation (%) that is the absolute deformation divided to the initial length. $\gamma = \frac{\Delta l}{l_0} \times 100$

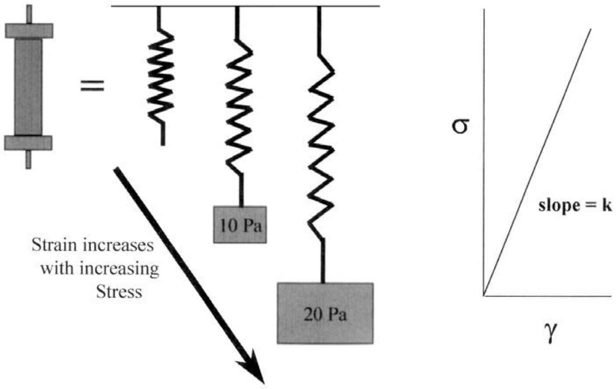

Figure 2.13. Hooke's law and stress-strain curve with slope representing the linear region to determine the young's modulus

An elastic material provides a linear response where the modulus is independent of load and of loading rate. Unfortunately, most materials are not truly elastic, for example the polymeric material in extension, the stress–strain curve is not linear instead there is curvature due to sample deformation. In cases in which stress increases and the material deforms this behavior is more clear, the curve has the initial linear region immediately followed by a nonlinear region. This characteristic feature is due to the sample necking and subsequent failure, here it is difficult to identify and calculate the young's modulus due to the limited linear portion. However, in such difficulties, the yield point of the material can be calculated which is defined as the maximum stress required for the sample failure that is called as the ultimate strength. After the sample reaches the yield strength there is an immediate deformation of the sample. The shape of this curve and its area defines whether the polymer is tough or brittle and strong or weak because energy needed to fracture sample is proportional to the area under the curve.

The oscillatory force is the principal of the DMA that causes the sinusoidal stress to be applied to the sample, which eventually creates a sinusoidal strain. The modulus (E) gives information about material stiffness and the capability to resist to the deformation and it is evaluated by the ratio between stress to strain. The slope (initial linear portion) of the stress–strain curve is known as the young's modulus a typical indicator of material behavior. The advantage of using DMA is that, a modulus value at each time is obtainable when a sine wave is applied, allowing us to sweep across a temperature or frequency range. For example, it is possible to record several modulus value during the time. Similarly, as a function of time or temperature the modulus can be recorded.[6]

However, while the classic stress-strain curve measured the classic modulus, DMA can measure three different moduli: a complex modulus (E*), an elastic modulus (E’), and an imaginary (loss) modulus (E’’) that allow to characterize better the material. This three modulus allow to calculate the ability of the material to return or store energy (E’), to its ability to lose energy (E’’), and the ratio of these effects (tanδ), which is also called damping.

In this study, the both static compression test and dynamic mechanical test were performed in compression clamp using Q800 DMTA analyser (USA).[1]

2.4.7. In vitro biological evaluation

Some of cell culture experiments illustrated in this Ph.D thesis were carried out in collaboration with the Department of Clinical Dentistry, University of Bergen, Bergen, Norway (dott. Ahmad Rashad and dott. Kamal Mustafa) and in collaboration with the biological group of Institute of Science and Technology for Ceramics, ISTEC-CNR, Faenza, Italy (dott. Samuele M. Dozio, dott. Silvia Panseri and dott. Monica Montesi).

2.4.7.1.Cell culture and Scaffold seeding

Different types of cells were used in this project such as mouse fibroblast L929 cell line (American Type Culture Collection CCL 1), mouse fibroblasts mBALB/3T3 clone A31 (American Type Culture Collection). Cells were cultured in Dulbecco Modified Eagle’s Medium high glucose (DMEM, Gibco), containing penicillin–streptomycin (100 U/mL–100 μg/mL) supplemented with 10% calf bovine serum and kept at 37°C in an atmosphere of 5% CO2. Cells were detached from culture flasks by trypsinization and centrifuged; cell number and viability were assessed with trypan blue dye exclusion test.[1]

a) Sterilized samples via γ ray were placed one per well in a 24-well plate and presoaked in culture medium for 24 h. Each scaffold was seeded by dropping 18,5 μL of cell suspension (5.0×10^4 cells) onto the upper surface, allowing cell attachment for 30 min, before addition into each well 1.5 mL of cell culture medium. The medium was changed every 3 days. All cell handling procedures were performed in a sterile laminar flow hood. All cell culture incubation steps were performed at 37°C with 5% CO_2.

b) 100 μg/ml of hybrid nanobeads suspended in the cell culture medium supplemented with citrate (0.1v/v %; Sigma-Aldrich) were added to the cell culture.

Nanobeads, sterilized by autoclave (20 minutes at 121°C, 2 bar), were sonicated before being added to the cells. Cells without addition of biomaterials were used as control group. All cell-handling procedures were performed in a sterile laminar flow hood. All cell-culture incubation steps were performed at 37°C with 5% CO2.

An indirect contact test with scaffold extracts was applied to evaluate the cytotoxicity of any leachables from the samples (8 mm in diameter and 4 mm height). The scaffolds were incubated with culture medium (3 cm2/mL) under constant shaking (60 rpm) for 24 h. Cells (200 µL suspension) were cultured in 96-well plates and incubated for 4 h before the culture medium was removed and replaced with the extract medium. The cells were then incubated with the extracts for another 24 h. Medium alone and medium containing 20 mg/ml phenol 99 % (Sigma Aldrich, Saint Louis, Missouri, USA) served as nontoxic and toxic controls, respectively.

2.4.7.2.Cell Viability Assay

Quantitative cell viability was assessed using the MTT assay. The MTT reagent (3-(4,5-dimethylthiazol-2-yl)-2,5-diphenyltetrazolium bromide) was prepared at 5 mg/mL in 1x PBS, and added at 1:10 ratio per well and kept 2h at 37°C. In this assay, the metabolically active cells react with the tetrazolium salt in the MTT reagent to produce formazan crystals.[7] Then, scaffolds were transferred to a tube containing 1mL of dimethyl sulfoxide (DMSO) that dissolved the crystals. Two hundred microliters of supernatant were transferred to a 96-well plate and the absorbance was read at 570 nm using a Multiskan FC Microplate Photometer (Thermo Scientific). The absorbance is directly proportional to the number of metabolically active cells. Six samples per time point per group (day 1, 3, and 7) were analyzed and mean values of absorbance were determined. Statistical analysis was performed by the GraphPad Prism software (version 6.0), with statistical significance set at $p \leq 0.005$.

Cell metabolic activity was evaluated using the WST-1 cell proliferation reagent (Roche, Germany). WST-1 reagent (1:10) was added to every well and incubated for 3 h. Absorbance was measured at 450 nm by a microplate reader (BMG LABTECH, Koblenz, Germany).

Qualitative cell viability was assessed using the Live/Dead assay kit (Invitrogen), performed according to manufacturer’s instructions. Briefly, scaffolds were washed with

1× PBS for 5 min and incubated with calcein acetoxymethyl (calcein AM) 2 µM, green-fluorescent dye for living cells and ethidium homodimer-1 (EthD-1) 4 µM, red-fluorescent dye for dead cells, for 15 min at 37°C in the dark. Samples were rinsed in 1× PBS. Samples' top surfaces were examined as well as their centers by previous sagittal cut. Images were acquired by an inverted Ti-E fluorescence microscope (Nikon). One sample per time point (1, 3, 7) was analyzed.[1]

2.4.7.3.Cell Morphology Analysis

Cell morphology was observed via SEM analysis, the samples were washed with 0.1 M sodium cacodylate buffer pH 7.4 and fixed in 2.5% glutaraldehyde in 0.1 M sodium cacodylate buffer pH 7.4 for 2 h at 4°C, washed in 0.1 M sodium cacodylate buffer pH 7.4 and freeze-dried. Dehydrated samples were sputter coated with gold and observed using SEM (ESEM Quanta 200, Fei).

In order to visualize actin filaments cells, after 3 days of culture, cells were washed with PBS 1x for 5 min, fixed with 4% (w/v) paraformaldehyde for 15 min and washed with PBS 1x for 5 min. Permeabilization was performed with PBS 1x with 0.1% (v/v) Triton X-100 for 5 min. FITC-conjugated Phalloidin antibody (Sigma) 8 µM in PBS 1x was added for 20 min at room temperature in the dark [31]. Cells were washed with PBS 1x for 5 min and incubated with nuclear stain DAPI (Invitrogen) 300 nM in PBS 1x for 5 min. Images were acquired by an Inverted Ti-E fluorescence microscope (Nikon).[1]

2.4.7.4.Statistical analysis

Results were expressed as Mean±SEM plotted on graph. Analysis was made by two-way ANOVA, followed by Bonferroni's post-hoc test. Statistical analysis was performed by the GraphPad Prism software (version 6.0), with statistical significance set at $p \leq 0.05$

REFERENCES

1. Savini Elisa. Design and development of biomineralized nanostructured devices from natural sources for biomedical applications. (University of Bologna, 2016).

2. Mao, J. S., Zhao, L. G., Yin, Y. J. & Yao, K. De. Structure and properties of

bilayer chitosan-gelatin scaffolds. *Biomaterials* **24**, 1067–1074 (2003).

3. Arora, A., Kothari, A. & Katti, D. S. Pore orientation mediated control of mechanical behavior of scaffolds and its application in cartilage-mimetic scaffold design. *J. Mech. Behav. Biomed. Mater.* **51**, 169–183 (2015).

4. Gostynska, N. *et al.* 3D porous collagen scaffolds reinforced by glycation with ribose for tissue engineering application. *Biomed. Mater.* **12**, (2017).

5. Shankar, K. G. *et al.* Investigation of different cross-linking approaches on 3D gelatin scaffolds for tissue engineering application: A comparative analysis. *Int. J. Biol. Macromol.* **95**, 1199–1209 (2017).

6. Campodoni, E. *et al.* Polymeric 3D scaffolds for tissue regeneration: Evaluation of biopolymer nanocomposite reinforced with cellulose nanofibrils. *Mater. Sci. Eng. C* **94**, 867–878 (2019).

7. Liu, Y., Peterson, D. A., Kimura, H. & Schubert, D. Mechanism of Cellular 3-(4,5-Dimethylthiazol-2-yl)-2,5-Diphenyltetrazolium Bromide (MTT) Reduction. *J. Neurochem.* **69**, 581–593 (2002).

3. In Bio-hybrid composite for dentin regeneration

3.1. Introduction

Teeth are hard, calcified structures found in the jaws (or mouths) with complex structures consisting of enamel and dentin supported by connective tissues (cementum, periodontal ligament and alveolar bone). Dentin structure, similar to that of bone, it is the most voluminous mineralized tissue of the tooth (~70% mineral, 20% organic, 10% water) and it consists of microscopic longitudinal dentinal tubules Its formation is a highly regulated process displaying several similarities with osteogenesis.[1] Several causes such as periodontal diseases, profound caries and trauma led to partial or full edentulism decreasing the individual life quality.

The choice of the suitable biomaterial plays a key role due to specific dentin characteristics like mineralized structure and a 3D architecture arranged in channel together to a suitable osteointegration.[2] Gelatin (Gel) is a biodegradable polymer which is obtained by collagen denaturation, this process allow to break the triple-helix structure into random coil maintaining the typical collagen properties such as biocompatibility, biodegradability and the ability to be mineralized On the other hand Gel has poor mechanical properties and stability that limit its application.[3] Chitosan (Chit) is a natural polysaccharide composed by glucosamine and N-acetylglucosamine, obtained by deacetylation of chitin, it is safe, hemostatic and osteoconductive.[4] It is synthesized by an enormous number of living organisms in the lower plant and animal kingdoms, serving in many functions where reinforcement and strength are required. Chit and Gel due to their functional groups can self-assembly generating a stable and homogeneous polymeric composite easy to process into a desiderable form like sponge, 3D scaffold, nanoparticles.[5,6] Biological HA is characterized by crystals with sizes in nano-scale, low degree of structural order and the crystal lattice is capable to include inside the structure or in the non-apatitic sites on the surface some foreign ions (CO_3, Na, K and Mg) substituting partially Ca and OH ions.[7] The HA features described above, bestow high solubility and specific biological activity of bone apatite on it.

In addition, exploiting the biomineralization process where the self-assembly of the polymer fibrils/molecules as well as the heterogeneous nucleation of hydroxyapatite were simultaneously induced, amazing and fascinating properties are bestowed on biomaterials, otherwise difficult to find in synthetic analogues.[8,9]

There are three key points essential to reproduce entirely dentin, i) it is a hard tissue composed of mineralized collagen with a high mineral content, around 70% [1,10]; ii) it is a tissue with a high toughness[11]; iii) it is endowed with an particular structure composed by channel called dentinal tubules, within them, there is an odontoblast process, which is an extension of an odontoblast, and dentinal fluid, which contains a mixture of albumin, transferrin, tenascin and proteoglycans.[12]

In response to these needs, in this chapter, hybrid composites were synthetized in which the mineral phase, composed of hydroxyapatite (HA) nucleated on gelatin fibers (Gel) is blended with a biopolymeric matrix (Gel and Chit) resembling the chemical composition and the nanocrystal sizes of natural mineralized tissues. A dentin-like 3D scaffold characterized from microscopic aligned channels suitable for tissue engineering was developed by means of a controlled freeze-drying process.

3.2. Synthesis process

Development of mineral phase (Gel/MgHA). Heterogeneous nucleation of MgHA nanocrystals on assembling Gel matrix was achieved by means of neutralization reaction performed as follows. An acid solution was prepared mixing H_3PO_4 (2.31 g in 100 mL of milliQ) in 2,5wt% gelatin solution (0.84 g in 33.5 mL of milliQ) at room temperature. Meanwhile, a basic solution was prepared adding 0.34 g of $MgCl_2$ to aqueous suspension of $Ca(OH)_2$ (2.60 g in 167 mL of milliQ) kept at room temperature. Immediately the acid solution was dropped into the basic solution under constant hand stirring at room temperature. The composite was left to ripen in the mother liquor without stirring for 2 hrs, then collected by centrifugation, washed three times with distilled water and, freeze-dried. Finally, a dehydrothermal treatment (DHT) after freeze-drying was carried out to introducing hybrid composite into an oven at 160°C for 48h under a pressure of 0.001 mbar, improve composite stability.

Development of hybrid 3D scaffold (Gel/MgHA@Gel-Chit). 10 mL of gelatin solution (12 wt%) was kept to 40 °C before adding 20 mL of chitosan solution (2 wt%) and, subsequently, the blend (Gel-Chit) was mixed for 30 min mechanically. Simultaneously, an aqueous suspension of Gel/MgHA hybrid composite (3.2 g in 66 mL) was prepared and subjected to sonication (tip sonicator ultrasonic processor XL 2020) in an ice bath for 10 min to disperse and homogenize the suspension. Gel-Chit blend was added to

Gel/MgHA under magnetic stirring at 37 °C and the final hybrid composite was left in those condition overnight. The 3D structure was realized by means of freeze-drying after introducing the composite into Teflon moulds. The freeze-drying cycle is performed with a controlled freezing ramp (50 °C/h) until -40 °C and with a controlled heating ramp of 5 °C/h from -40 °C to -5 °C and 3 °C/h until 20 °C for about three days under vacuum conditions (P= 0.086 mbar). Finally, Gel/MgHA@Gel-Chit 3D hybrid scaffold underwent DHT treatment (160°C for 48h under a pressure of 0.001 mbar) improving scaffold stability thanks to covalent bonds' formation.

Development of 3D polymer scaffold as control (Gel-Chit). 10 mL of gelatin solution (12 wt%) was kept to 40 °C before adding 20 mL of chitosan solution (2 wt%) and, subsequently, the blend (Gel-Chit) was mixed for 30 min mechanically. Gel-Chit blend was left under magnetic stirring at 37 °C overnight. The 3D structure was realized by means of freeze-drying after introducing the composite into Teflon moulds The freeze-drying cycle is performed with a controlled freezing ramp (50 °C/h) until -40 °C and with a controlled heating ramp of 5 °C/h from -40 °C to -5 °C and 3 °C/h until 20 °C for about three days under vacuum conditions (P= 0.086 mbar). Finally, Gel-Chit 3D polymer scaffold underwent DHT treatment (160°C for 48h under a pressure of 0.001 mbar) improving scaffold stability thanks to covalent bonds' formation.

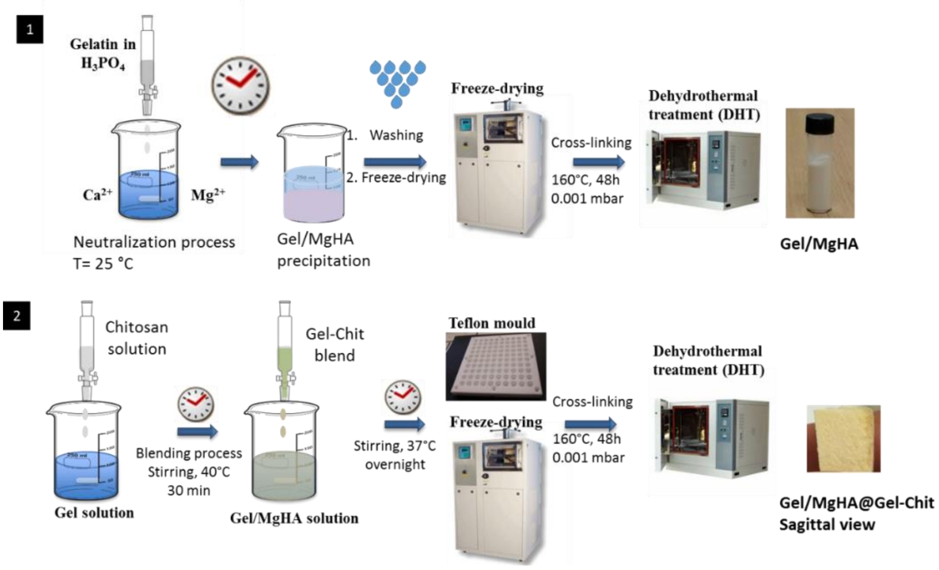

Figure 3.1. Schematic illustration of all step to develop 3D dentin-like biomaterial; 1. synthesis of Gel/MgHA hybrid composite; 2. Synthesis of Gel/MgHA@Gel-Chit 3D hybrid scaffold.

3.3. Results & Discussion

Hybrid particles composed of Gel and MgHA were obtained through biomineralization process where the acid solution composed of phosphate ions and Gel was dropped into a basic suspension composed of calcium and magnesium ions However, the final shape obtained after washing and sieving was that of particles and not scaffold. Biomineralization process was widely studied and exploited for the development of mineralized collagen based materials for bone regeneration.[13–15] According to best of our knowledge, Gel have a different behavior compared to collagen It is produced by hydroxylation of Collagen, therefore, its final structure is less organized than collagen.[16,17] As many literature shows, the biomineralization process on collagen fibers followed by freeze-drying technique allows to obtain a 3D hybrid composite highly mineralized and self-assembled.[18–20] On the other hand, the same protocol using Gel does not allow to obtain a 3D scaffold, but a highly mineralized powder (Gel/MgHA), because functional groups of Gel are busy for more roles (Figure 3.2). They link between them bearing the self-assembly and they host the nucleation of hydroxyapatite interacting with calcium and phosphate ions.[17] Gel/MgHA makes available mostly of its functional groups to interact with calcium and phosphate ions constraining the nucleation of hydroxyapatite on its fibers. In this way, a highly biomimetic material is developed, very close to natural hard tissues, nevertheless without any 3D architecture useful to provide appropriate micro-environment for cells to form the final structured organ.[21] To overcome this issue, mineralized Gel (Gel/MgHA) with combined to a polymer blend (Gel-Chit) in order to exploit both properties. Gel/MgHA represented mineral phase, while the polymer blend composed of Gel and Chit conferred the 3D aligned architecture essential for dentin-like structures. Mineral phase is constituted by mineralized Gel despite of hydroxyapatite alone for different reasons. On the one hand, gelatin in the mineral phase improves the biomimetism obtaining a material very close to natural tissue in terms of morphology, chemical composition and crystallinity.[9] On the other hand, Gel constrains the HA nucleation and the size was smaller obtaining a more homogeneous material due to a more affinity between functional groups of blend and mineralized gelatin promoting the dispersion of mineral phase in blend.[14,18,22] As figure 3.2 shows, after 24h HA alone mixed in the blend precipitates, while HA mineralized on gel mixed in the blend is completely dispersed creating a homogenous hydrogel. Polymer phase is composed of a blend of Gel and Chit; the latter has a positive charge under acidic conditions that come from protonation of its free amino groups. The positive charge allows the fabrication of composite materials with Gel revealing the formation not only of hydrogen bonds within and between chains of polymers, but also of electrostatic interactions between -COO(-) of Gel and -NH3(+) of Chit.[5,23] Those strong chemical interactions allowed a spontaneous self-assembling of Gel-Chit molecules and the generation of a stable and homogeneous polymer composite easy to process into a desirable form as sponge, 3D scaffold and hydrogels nanoparticles, to meet a specific application.[6,24]

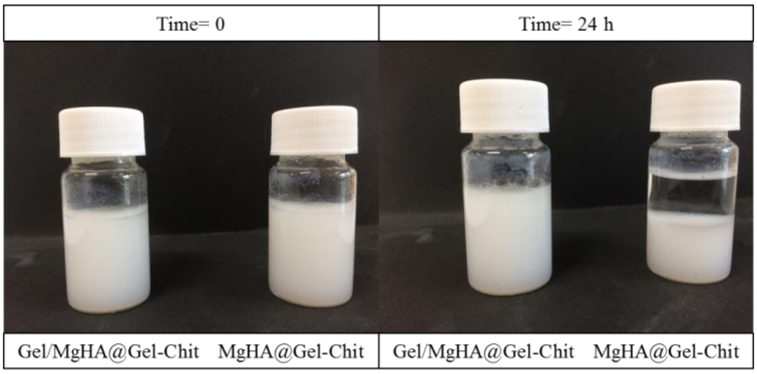

Fig. 3.2. Comparison between MgHA and Gel/MgHA as mineral phase in dentin-like scaffold. After 24h MgHA is precipitated highlighting the lower affinity between mineral and polymeric phases than Gel/MgHA.

Finally, the maintenance of 3D architecture from hydrogel to dry scaffold was supported by freeze-drying technique where a directional freezing allowed to obtain interconnected and organized pores. The pore characteristics such as size, homogeneity and orientation are dependent on ice crystal nucleation and growth.

Quantitative ICP analysis was applied to determine the overall content of Ca, P and Mg present in the mineral phase of hybrid materials. In Table 3.1 are shown the most significant data for the Gel/MgHA hybrid particles and for Gel/MgHA@Gel-Chit hybrid scaffold. In Gel/MgHA, ICP revealed the presence of Mg^{2+} ions and a Ca/P ratio of 1.62 lower than that of stoichiometric HA (Ca/P=1.67) and thus confirming the nucleation of a biomimetic substituted apatitic phase more soluble and bioactive then the stoichiometric one. According to the literature, the nucleation of a biomimetic HA is promoted by low synthesis temperature, presence of foreign ions and of polymeric phase.[25,26] The HA lattice promote the introduction of foreign ions, especially Mg^{2+} introduced during the synthesis can partially substitute Ca^{2+} ions creating a hybrid composite whose composition is more similar to young bones. By integrating the Gel/MgHA particles into

Gel-Chit blend to obtain the 3D hybrid scaffold (Gel/MgHA@Gel-Chit), the mineral phase does not change their characteristic as ICP revealed (Table 3.1).

Table 3.1. ICP analysis of Gel/MgHA and Gel/MgHA@Gel-Chit composites.

	Gel/MgHA	Gel/MgHA@Gel-Chit
Ca/P (mol)	1.62±0.05	1.65±0.01
(Mg+Ca)/P (mol)	1.70±0.07	1.75±0.02
Mg/Ca (mol)	0.05±0.01	0.05±0.01

ICP results were confirmed also by XRD analysis on both Gel/MgHA and Gel/MgHA@Gel-Chit as Figure 3.3A shows. In both case, the diffraction pattern was identified in hydroxyapatitic pattern as main phase (ICDD card n. 09-0432) and comparing spectra with MgHA (prepared with the same neutralization process), it can be stated that no secondary phase is appreciated. The main indices for nanometer sized apatite are (002), (102), (201), (211), (112), (300), (202), (130), (222), (213), (004) corresponding to $2\theta = 25.9°; 28.2°; 29.1°; 32.0°; 33.1°; 34.1°; 35.7°; 39.9°; 46.7°; 49.5°; 53.2°$.[27,28] The broad peaks evidenced in the XRD pattern report to a mineral phase with very small crystal domains, as an effect of the low synthesis temperature and the possible incorporation of foreign ions, such as Mg^{2+}, in the apatite structure, provoking structural destabilization. Noticeably, the 002 reflections (θ=25.9°) is particularly enhanced typical in the biomineralization process, meaning a preferential crystal development along the c axis of the hexagonal lattice of hydroxyapatite induced by the presence of gelatin. XRD diffraction revealed wider peaks due to features described above such as the presence of Mg^{2+}, of gelatin and the low synthesis temperature which highlight a less crystalline and thus more biomimetic mineral phase.[29,30] In addition, as supported from ICP analysis, the XRD pattern of Gel/MgHA@Gel-Chit confirmed the typical pattern of MgHA with wider peaks characteristic of a low crystallinity, highlighting as processes such as blending, freeze-drying and cross-linking preserved the features of mineral phase (Figure 3.3A).

The overall loss of weight due to thermal treatment (TG analysis) of freeze-dried Gel/MgHA and Gel/MgHA@Gel-Chit are shown in Figure 3.3B. Thermal decomposition profile of Gel/MgHA shows two distinct weight losses The first, in the rage temperature of 30-150 °C was due to evaporation of absorbed water, while the second weight loss, occurred between 250 and 450 °C, was attributed to the decomposition of gelatin molecules. The thermal decomposition is completed around 450°C, with an overall decrease of organic components of about 20 wt%, thus the total amount of MgHA is estimated close to the 80 wt% required to maintain an adequate amount of mineral phase in the final scaffold (Figure 3.3B).[13,31] The thermogravimetric analysis of the final material, Gel/MgHA@Gel-Chit, shows instead three weight losses: the losses due to water evaporation and gelatin molecules decomposition can be overlaid to those of the first thermal profile, while the new weight loss between 250 and supposedly 550°C, may be attributed to the decomposition of Chitosan.[32] The thermal decomposition is completed around 600°C, with an overall decrease of organic components of about 40 wt% of the total weight. The final weight ratio between inorganic/organic was so estimated to be 60/40 wt still suitable for hard tissue regeneration (Figure 3.3B)

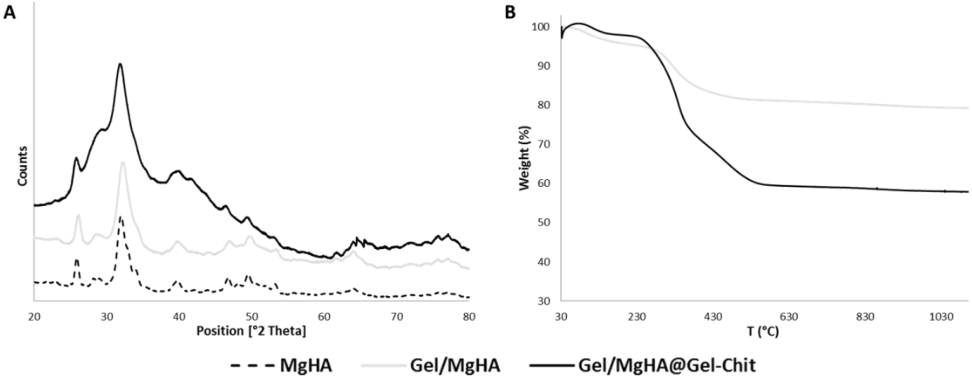

Figure 3.3. A) XRD spectra of Gel/MgHA and Gel/MgHA@Gel-Chit compared with synthetic MgHA; B) Thermal decomposition profile (TGA) of Gel/MgHA and Gel/MgHA@Gel-Chit

Scanning Electron Microscopy (SEM) was used to evaluated the material morphology and the influence of mineral phase in the polymeric blend, comparing Gel/MgHA morphology (Figure 3.4 A, B), the dentin like scaffold Gel/MgHA@Gel-Chit (Figure 3.4 C, D, E) and the control Gel-Chit (Figure 3.4 F, G, H). The images of Gel/MgHA revealed particles with irregular shape and dimensions (Figure 3.4 A) where the mineral phase (MgHA) is recognizable as microparticles of about 5-10 µm well linked and distributed on the polymer phase (Figure 3.4 B). The same morphology is observed only on the scaffold pores surface in Gel/MgHA@Gel-Chit highlighting as the mineral phase is homogenously distributed all along the scaffold (Fig. 3.4 E). Gel-Chit control scaffold revealed a smooth surface due to the absence of the mineral phase (Fig 3.4 G, H). Observing the scaffold macrostructure (Figure 3.4 D, G), is clear that the pores alignment is preserved in both scaffold despite of the presence of Gel/MgHA particles even if led to a reduction of pore size from about 132 µm to 62 µm (Table 3.2).

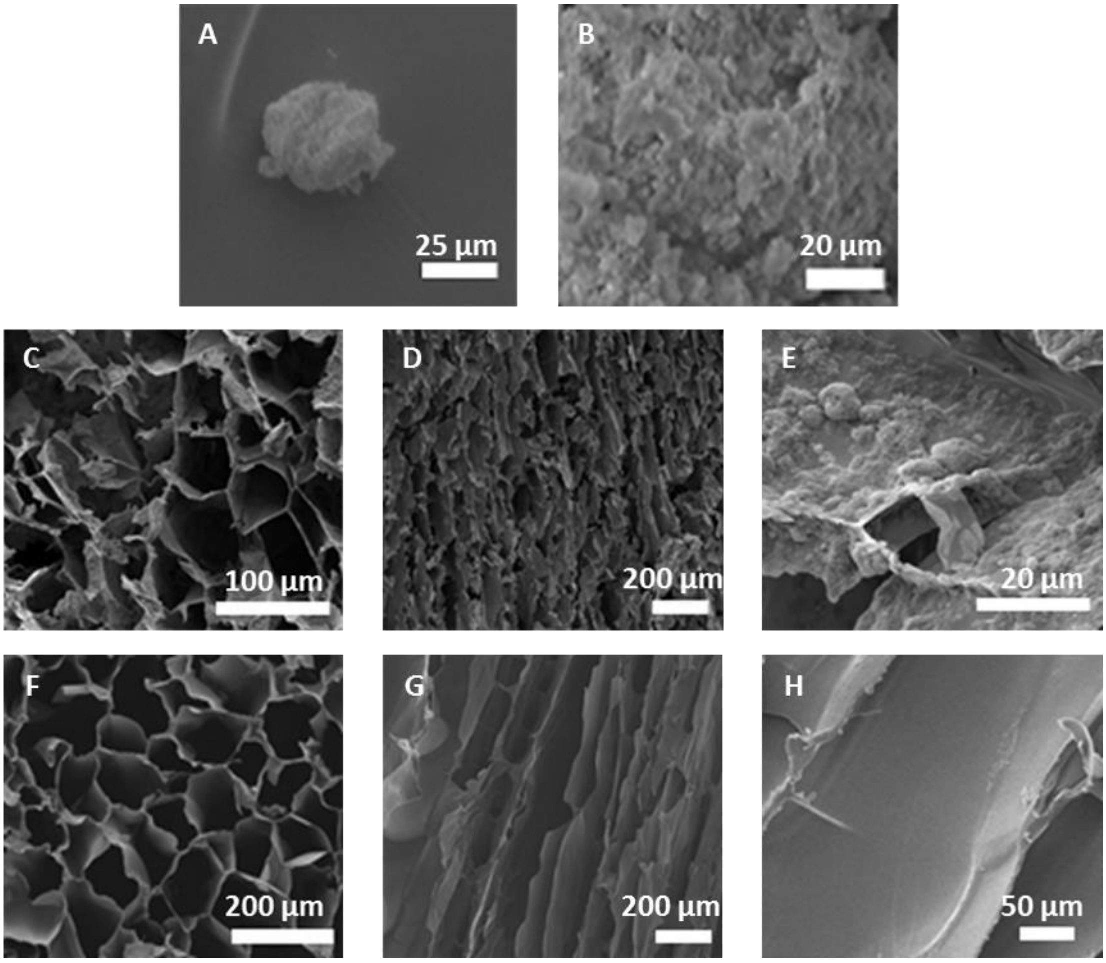

Figure 3.4. SEM images of (A, B) Gel/MgHA hybrid particles; (C, D, E) Gel/MgHA@Gel-Chit; (F, G, H) Gel-Chit control. In particular, comparison between cross section (C, F); longitudinal section (D, G) and surface detail (E, H).

Moreover, Gel/MgHA particles did not interfere in the assembling of a structure featured by a 3D alignment and by a high porosity. As evaluated by the density method, both scaffolds showed a total porosity, including nano and micro porosity, close to 95%. Concerning the macro porosity, referred only to the pores available for cell colonization and proliferation and evaluated by water squeezing method, it was slightly lower, but it still maintains high values around 80%.[33,34] In both porosity tests, Gel/MgHA@Gel-Chit hybrid scaffold highlighted higher values than the control Gel-Chit (Table 3.2).

Table 3.2. Morphological parameters: porosity (%), density and pore size of Gel-Chit and Gel/MgHA@Gel-Chit scaffolds.

		Gel-Chit	Gel/MgHA@Gel-Chit
% porosity	Density method	95.4 ± 0.1	97.6 ± 0.1
	Water squeezing method	82.1 ± 3.3	87.2 ± 1.8
Density (g/cm^3)		4.59 ± 0.07	2.46 ± 0.16
Pore size (µm)		132.08 ± 39.98	61.78 ± 15.14

In addition to an ideal chemical composition supporting cellular growth, a suitable 3D architecture is essential to promote it. In particular, the designed dentin-like scaffold shown a highly interconnected total porosity comprising macropores essential for cells colonization which, combined to an ideal composition and a good swelling means that cells will be stimulated to enter and proliferate along the entire scaffold.[35] Furthermore, DHT allowed to improve scaffold stability by decreasing its degradation rate; it is called zero-length cross-linking because promote the formation of amide groups between the fibers without any other chemical molecules. This type of cross-linking is not cytotoxic and safer for medical applications, however, the direct reaction on blend functional groups decreases the hydrophilicity of the scaffold and, consequently, its swelling ratio.[19,36] In this research, a compromise has been found by thermally cross-linking scaffolds whose constituting polymers are abundant of functional hydrophilic groups.

Therefore, the scaffold showed a high stability together with a suitable swelling which are fundamental requirements to enable the cells to perform tissue regeneration. From the analyses (Fig. 3.5), Gel/MgHA@Gel-Chit and control Gel-Chit displayed a good swelling because scaffolds absorb medium around 12-15 time their weight; in detail both scaffold Gel-Chit and Gel/MgHA@Gel-Chit displayed a swelling ratio after 6h of 12,2 ± 1,1 and 15,2 ± 1,3 respectively (Figure 3.5A). Furthermore, both scaffolds degraded less than 20%. In detail, Gel-Chit and Gel/MgHA@Gel-Chit, after 28 days, revealed a degradation percentage of 24,3 ± 1,7 and 16,9 ± 1,7, respectively (Figure 3.5B). Therefore, MgHA has demonstrated to play a dual role acting as hydrophilic factor by increasing the swelling ratio and as stabilizing factor by decreasing the scaffold degradation rate. [31]

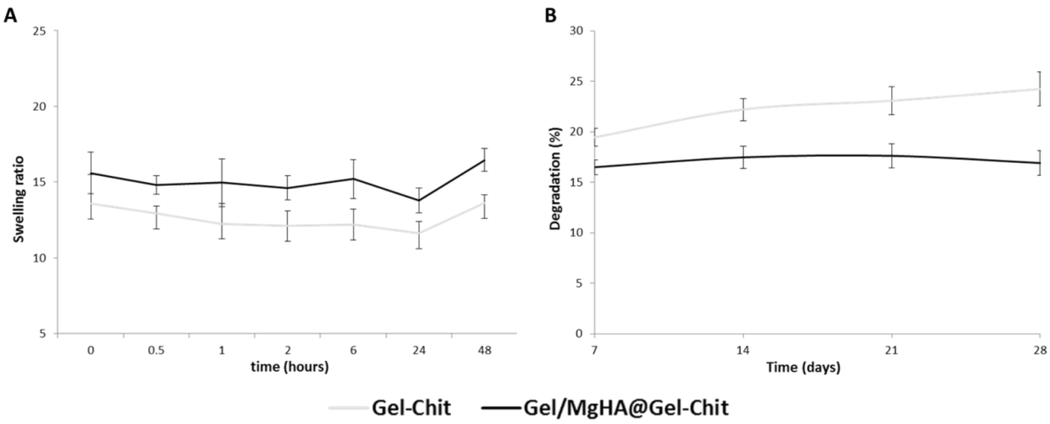

Figure 3.5. A) Swelling behavior and B) degradation rate of Gel/MgHA@Gel-Chit, performed in PBS at 37 °C.

Since the scaffolds are expected to be used in a hydrated environment, it is relevant to evaluate their biomechanical behavior in in vivo-like conditions, in terms of temperature and hydration state. It was possible by using DMA apparatus, allowing to setup temperature and dry or wet environment before the tests, that we used to evaluate the mechanical performances of Gel/MgHA@Gel-Chit 3D hybrid composite (Figure 3.6). The catastrophic failure plateau and the densification regions of the scaffolds can be observed from the typical stress-strain curve as seen in Figure 3.6A). The Young modulus of the Gel/MgHA@Gel-Chit scaffolds, calculated between 1-15 % strain value, is 6.12 kPa.[37] On observing the visco-elastic behavior of the scaffold, the storage modulus (E') increased with increase in frequency (Figure 3.6B). In response to oscillating frequencies, Gel/MgHA@Gel-Chit represented significant variation in their E' value. Ranging from 0.1 Hz to 10 Hz, it showed E' value which increased from 15.2 ± 3.6 kPa to 24.1 ± 2.8 kPa.[38] Finally, the creep tests (Figure 3.6C) show the behavior of scaffold when it is subjected to a static stress for a specific time and the strain recovering after releasing of stress. Static stress was identified with a preliminary linearity study and correspond to 0.005 MPa. During the compression of 15 minutes, Gel/MgHA@Gel-Chit reached a strain of 70%, however, after stress releasing, it recovers the majority of original shape. The spectra show indeed that the final strain is about 28 % and the strain recovery is close to 60 %.

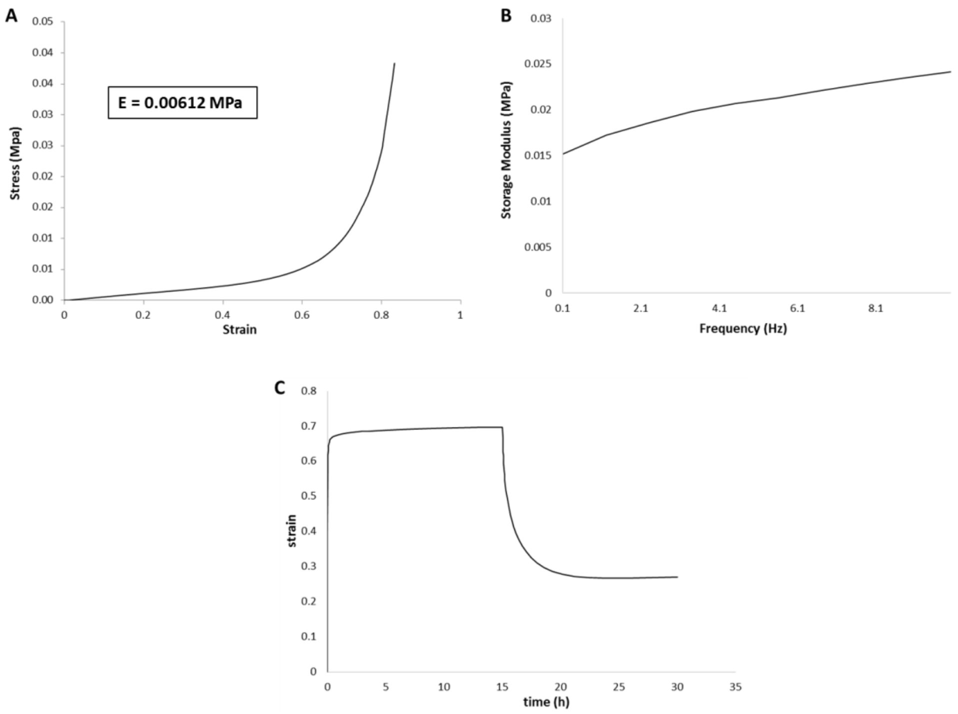

Figure 3.6. Compressive mechanical test of Gel/MgHA@Gel-Chit performed after immersion in PBS at 37 °C overnight. (A) Average stress-strain curves (n=5 specimens); (A inset) Young's modulus calculated as the slope of the stress-strain curve in a range from 1-10 % (n=5 specimens, data are mean ± SEM); (B) Average storage modulus (E')-frequency curves measured from 0.1 to 10 Hz (n= 5 specimens); (C) Average creep curves obtained after a creep time of 15 min and a recovery time of 15 min (n=5 specimens).

Finally, chemical and physical investigations on our material highlighted as the mineral phase was composed of a low crystalline HA due to the presence of Gel that constrained the nucleation and the introduction of Mg^{2+} ions inside the nucleated HA lattice typical of young hard tissues, furthermore its introduction in the polymeric blend allowed the creation of a 3D architecture with high and interconnected porosity capable to promote swelling without a rapid degradation. These features made Gel/MgHA@Gel-Chit highly biomimetic and favored its biological properties. It was bioactive, biodegradable, biocompatible and easily recognized by cells, thanks to the high hydrophilicity and porosity, particularly in terms of macropores, which fostered cell adhesion, colonization, proliferation and differentiation. For all this reason, in vitro evaluation was performed to give it a promising candidate for dentin regeneration. To assess whether or not the chemical composition of the biomaterials could lead to cytotoxicity, compromising the cellular viability, two types of assay have been performed. The quantitative cell viability MTT assay showed an increment over time of the absorbance directly related to the metabolically active cells, with each absorbance value per time point statistically different compared to the previous ones (Figure 3.7).

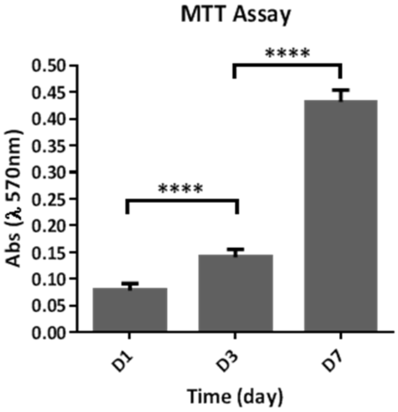

Figure 3.7. Quantitative analysis of cell proliferation using the MTT assay at 1, 3 and 7 days after seeding (n = 6). Scaffolds alone were used as blank. ****p ≤ 0,0001.

The quantitative cell viability assay is supported by the qualitative assay performed using the Live/Dead assay kit, as it confirmed the presence of a greater number of healthy and living cells compared to the dead cells, increasing at every time point (Fig.3.8).

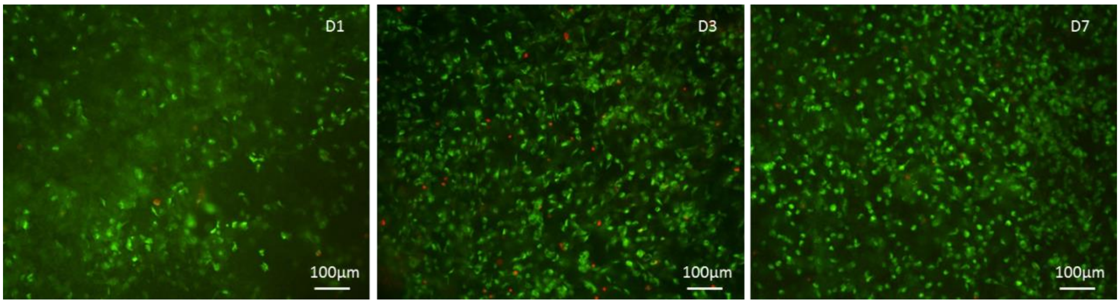

Figure 3.8. Qualitative cell viability analysis of Gel/MgHA@Gel-Chit performed with the Live/Dead kit, calcein stains live cells in green, ethidium homodimer-1 stains dead cells in red; at day 1, 3 and 7 after seeding.

The effects of both the chemical composition and structural rugosity of the scaffolds on the morphology of the cells were assessed via SEM observations (Fig. 3.9). These analyses showed cells with a healthy morphology and evident cytoplasmic extensions. It also revealed the absence of round-shaped cells, indicators of impaired anchoring capability due to lack of cell-material compatibility.

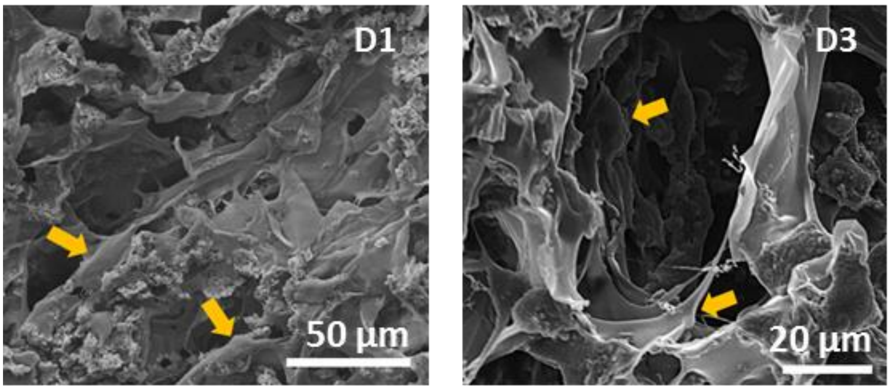

Figure 3.9: SEM images of cell-seeded scaffolds at day 1 and 3 after seeding. Yellow arrows show some cells stretched and anchored onto the scaffolds.

In conclusion, cell growth is also influenced by the overall biocompatibility of the materials, through the quality of the cell-material interaction.[35] The goodness of such interactions is determined by the material chemical composition and structural conformation as well as the overall surface rugosity. In the present study, the Gel/MgHA@Gel-Chit hybrid scaffold chemical composition does not interfere with the cell viability as proved by both the qualitative and quantitative cell viability assays. Also, along with the chemical composition, both the structural topography and rugosity of the scaffolds contributed to the overall cell growth, as proved by the SEM images showing good cells adhesion and healthy cytoplasmic spreading. From the biological point of view this biomaterial has proved to be viable for cells colonization and further experimentations.

3.4. Conclusion

Hybrid composite has been designed with customized characteristics with the aim to develop a dentin-like scaffold. In particular, studying the teeth morphology and the dentin structure, we want to create a hybrid composite that mimic perfectly the dentin in terms of chemical composition and 3D architecture so that cells can recognize the hybrid composite as self-dentin and thus a suitable microenvironment for cell proliferation and differentiation. A biomimetic approach was followed and a biomineralization process was performed on Gel matrix to develop a bio-hybrid material (Gel/MgHA@Gel-Chit) where the mineral and the organic phases mimicked the natural dentin, not only in terms of chemical composition but also for the 3D microstructure. Gel was selected as a promising organic template for biomineralization process due to its well noted biocompatibility and suitability for the development of scaffold for tissue regeneration. The developed Gel/MgHA, blended in a Gel-Chit matrix allowed to obtain a biomimetic and bioactive hybrid material (Gel/MgHA@Gel-Chit) where the mineral phase is well integrated and homogenously distributed. By means of well-studied cross-linking processes and optimized freeze-drying was possible to design micro- and macro-porous structures that cells recognized as natural tissue. This was confirmed by the preliminary *in vitro* investigation. In conclusion, hybrid composite thanks to its channel-like structure was thought for dentin regeneration where the morphological aspects together with the chemical composition and the swelling and mechanical behaviors, act as key factors for its promotion. However, this material could be exploited for the regeneration of hard tissues where the high mineralization and the 3D architecture are key factors.

REFERENCES

1. Wegst, U. G. K., Bai, H., Saiz, E., Tomsia, A. P. & Ritchie, R. O. Bioinspired structural materials. *Nat. Mater.* **14**, 23–36 (2015).

2. Liu, Y. *et al.* Biological tooth root reconstruction with a scaffold of swine treated dentin matrix. doi:10.1039/c5ra27332c

3. Boanini, E., Rubini, K., Panzavolta, S. & Bigi, A. Chemico-physical characterization of gelatin films modified with oxidized alginate. *Acta Biomater.* **6**, 383–388 (2010).

4. Zhao, F. *et al.* Preparation and histological evaluation of biomimetic three-dimensional hydroxyapatite/chitosan-gelatin network composite scaffolds. *Biomaterials* **23**, 3227–3234 (2002).

5. Nieto-Suárez, M., López-Quintela, M. A. & Lazzari, M. Preparation and characterization of crosslinked chitosan/gelatin scaffolds by ice segregation induced self-assembly. *Carbohydr. Polym.* **141**, 175–183 (2016).

6. Pulieri, E. *et al.* Chitosan/gelatin blends for biomedical applications. *J. Biomed. Mater. Res. - Part A* **86**, 311–322 (2008).

7. Gómez-Morales, J., Delgado-López, J. M., Iafisco, M., Hernández-Hernández, A. & Prat, M. Amino Acidic Control of Calcium Phosphate Precipitation by Using the Vapor Diffusion Method in Microdroplets. *Cryst. Growth Des.* **11**, 4802–4809 (2011).

8. Weiner, S. Biomineralization: A structural perspective. *Journal of Structural Biology* **163**, 229–234 (2008).

9. Sprio, S. *et al.* Bio-inspired assembling/mineralization process as a flexible approach to develop new smart scaffolds for the regeneration of complex anatomical regions. *J. Eur. Ceram. Soc.* **36**, 2857–2867 (2016).

10. Hakki, S. S., Karaoz, E., Hakki, S. S. & Karaoz, E. Dental Stem Cells: Possibility for Generation of a Bio-tooth. *Stem Cell Biol. Regen. Med.* **167**, (2016).

11. Zhang, Y. R., Du, W., Zhou, X. D. & Yu, H. Y. Review of research on the mechanical properties of the human tooth. *Int. J. Oral Sci.* **6**, 61–69 (2014).

12. Palosaari, H. *et al.* Expression profile of matrix metalloproteinases (MMPs) and tissue inhibitors of MMPs in mature human odontoblasts and pulp tissue. *Eur. J. Oral Sci.* **111**, 117–127 (2003).

13. Menale, C. *et al.* MSC-Seeded Biomimetic Scaffolds as a Factory of Soluble RANKL in Rankl-Deficient Osteopetrosis. *Stem Cells Transl. Med.* 1–13 (2018). doi:10.1002/sctm.18-0085

14. Tampieri, A. *et al.* Design of graded biomimetic osteochondral composite scaffolds. *Biomaterials* **29**, 3539–3546 (2008).

15. Krishnakumar, G. S. *et al.* Ribose mediated crosslinking of collagen-hydroxyapatite hybrid scaffolds for bone tissue regeneration using biomimetic strategies. *Mater. Sci. Eng. C* **77**, 594–605 (2017).

16. Djagny, K. B., Wang, Z. & Xu, S. Gelatin: A valuable protein for food and pharmaceutical industries: Review. *Crit. Rev. Food Sci. Nutr.* **41**, 481–492 (2001).

17. Panseri, S. *et al.* Biomimetic Scaffold with Aligned Microporosity Designed for Dentin Regeneration. *Front. Bioeng. Biotechnol.* **4**, 48 (2016).

18. Tampieri, A. *et al.* Biologically inspired synthesis of bone-like composite: Self-assembled collagen fibers/hydroxyapatite nanocrystals. *J. Biomed. Mater. Res. - Part A* **67**, 618–625 (2003).

19. Krishnakumar, G. S. *et al.* Evaluation of different crosslinking agents on hybrid biomimetic collagen-hydroxyapatite composites for regenerative medicine. *Int. J. Biol. Macromol.* **106**, 739–748 (2018).

20. Sprio, S., Sandri, M., Panseri, S., Cunha, C. & Tampieri, A. Hybrid scaffolds for tissue regeneration: Chemotaxis and physical confinement as sources of biomimesis. *J. Nanomater.* **2012**, (2012).

21. Eslahi, N., Abdorahim, M. & Simchi, A. Smart Polymeric Hydrogels for Cartilage Tissue Engineering: A Review on the Chemistry and Biological Functions.

Biomacromolecules **17**, 3441–3463 (2016).

22. Tampieri, A. *et al.* Biologically Inspired Nanomaterials and Nanobiomagnetism: A Synergy among New Emerging Concepts in Regenerative Medicine. in *Bio-Inspired Regenerative Medicine* 1–20 (Pan Stanford, 2016). doi:doi:10.1201/b19914-2

23. Huang, Y., Onyeri, S., Siewe, M., Moshfeghian, A. & Madihally, S. V. In vitro characterization of chitosan-gelatin scaffolds for tissue engineering. *Biomaterials* **26**, 7616–7627 (2005).

24. Prata, A. S. & Grosso, C. R. F. Production of microparticles with gelatin and chitosan. *Carbohydr. Polym.* **116**, 292–299 (2015).

25. Tampieri, A., Sprio, S., Sandri, M. & Valentini, F. Mimicking natural bio-mineralization processes: A new tool for osteochondral scaffold development. *Trends Biotechnol.* **29**, 526–535 (2011).

26. Tampieri, A., Celotti, G. & Landi, E. From biomimetic apatites to biologically inspired composites. *Anal. Bioanal. Chem.* **381**, 568–576 (2005).

27. Landi, E., Valentini, F. & Tampieri, A. Porous hydroxyapatite/gelatine scaffolds with ice-designed channel-like porosity for biomedical applications. *Acta Biomater.* **4**, 1620–1626 (2008).

28. Rusu, V. M. *et al.* Size-controlled hydroxyapatite nanoparticles as self-organized organic–inorganic composite materials. *Biomaterials* **26**, 5414–5426 (2005).

29. Iafisco, M., Ruffini, A., Adamiano, A., Sprio, S. & Tampieri, A. Biomimetic magnesium-carbonate-apatite nanocrystals endowed with strontium ions as anti-osteoporotic trigger. *Mater. Sci. Eng. C* **35**, 212–219 (2014).

30. Tampieri, A. *et al.* HA/alginate hybrid composites prepared through bio-inspired nucleation. *Acta Biomater.* **1**, 343–351 (2005).

31. Ramírez-Rodríguez, G. B. *et al.* Biomimetic mineralization of recombinant collagen type I derived protein to obtain hybrid matrices for bone regeneration. *J. Struct. Biol.* (2016). doi:10.1016/j.jsb.2016.06.025

32. Lozano-Navarro, I. J. *et al.* Chitosan-Starch Films with Natural Extracts: Physical, Chemical, Morphological and Thermal Properties. *Materials* **11**, (2018).

33. Mao, J. S., Zhao, L. G., Yin, Y. J. & Yao, K. De. Structure and properties of bilayer chitosan-gelatin scaffolds. *Biomaterials* **24**, 1067–1074 (2003).

34. Arora, A., Kothari, A. & Katti, D. S. Pore orientation mediated control of mechanical behavior of scaffolds and its application in cartilage-mimetic scaffold design. *J. Mech. Behav. Biomed. Mater.* **51**, 169–183 (2015).

35. Montesi, M. & Panseri, S. Triggering Cell-Biomaterial Interaction: Recent Approaches for Osteochondral Regeneration. in *Bio-Inspired Regenerative Medicine* 283–304 (Pan Stanford, 2016). doi:doi:10.1201/b19914-12

36. Madaghiele, M. *et al.* Assessment of collagen crosslinking and denaturation for the design of regenerative scaffolds. *J. Biomed. Mater. Res. - Part A* **104**, 186–194 (2016).

37. Yan, L. P. *et al.* Macro/microporous silk fibroin scaffolds with potential for articular cartilage and meniscus tissue engineering applications. *Acta Biomater.* **8**, 289–301 (2012).

38. Yan, L. P. *et al.* Genipin-cross-linked collagen/chitosan biomimetic scaffolds for articular cartilage tissue engineering applications. *J. Biomed. Mater. Res. - Part A* **95 A**, 465–475 (2010).

4. Bio-hybrid composites for soft and hard tissue regeneration

4.1. Introduction

Tissue engineering emerged as a viable therapeutic solution to regenerate diseased tissues, anyway, the rapid restoration of function of damaged tissues is still a major challenge in surgery. Associated to the concept of tissue engineering also the material science was involved and aimed at designing new custom-made scaffolds offering ideal environment for cell adhesion and migration, and regulating cellular proliferation and function by providing proper biochemical signals.[1,2] The current focus of biomedical research is on the unique characteristics and properties of these natural polymer structures useful for creating hydrogels, polymer nanocomposites and hybrid composites for the fabrication of biocompatible and biodegradable scaffolds, which meet the requirements of mechanical and mass transport properties (permeability and diffusion).[3,4] In particular, by blending polymers it is possible to combine the best properties of two or more materials and to develop nanocomposite scaffolds with unique characteristics that otherwise are difficult to achieve.[5]

Gelatin is an important hydrocolloid in the food, pharmaceutical and photographic industries. It has been deeply studied for the development of biomaterials for application in tissue engineering and regenerative medicine due to easy production, low cost and high biocompatibility.[6,7] Compared with collagen, gelatin is commercially available at low cost and, as its precursor, it contains the Arginine-Glycine-Aspartic acid (RGD) sequences responsible for promoting cell adhesion.[8] However, the use of gelatin as a 3D scaffold is limited due to their poor mechanical properties. Cellulose nanofibrils and nanocrystals are appealing as nano-reinforcement of scaffolds for biomedical application, specifically owing to their high surface area, high aspect ratio and exceptional mechanical properties.[9,10] Cellulose nanofibrils (CNF) are produced from wood or other plants and can be treated with (2,2,6,6-tetramethyl-piperidine-1-yl)oxyl radical (TEMPO) mediated oxidation and sodium hypochlorite as an oxidant, to introduce aldehyde and carboxyl groups on the fibrils' surface.[11,12]

The major gelatin drawbacks together with the poor mechanical properties is the rapid degradation that limit its further long-terms biomedical applications in tissue engineering. Several cross-linking methodologies have been studied to increase the stability of 3D structures. Physical cross-linking methods include dehydrothermal treatment and ultraviolet and gamma irradiation.[13,14] Furthermore, due to the large number of functional side groups it contains, gelatin readily undergoes chemical cross-linking. This is usually performed using bifunctional reagents as glutaraldehyde (GTA) and diisocyanates, as well as carbodiimides (EDC or NHS), polyepoxy compounds (BDDGE) and natural cross-linking agents as genipin. In the case of nanocellulose, hexamethylenediamine (HMDA) has been proposed as an effective cross-linking agent.[15,16] Another strategy adopted to further improve the mechanical performance of the scaffold was to blend gelatin with variables amounts of reinforcing elements such as TEMPO-oxidized CNF.

Finally, to extend the application of this material not only to soft tissue but also to bone regeneration hydroxyapatite (HA), suitable to confer osteoinductive characteristics and promote cell adhesion and differentiation in mature bone cells[17–19], was introduced in 3D polymeric scaffold.

In particular, this chapter is divided into 3 main goals:

i) **<u>evaluation of the influence of cross-linkers on polymeric scaffold</u>**

Reinforced nanocomposites were prepared by blending Gel with CNF and modulating their chemical stability and mechanical behavior by means of different cross-linking approaches. Three different cross-linkers were chosen to modulate the degradation rate of Gel-CNF blend: genipin as gelatin cross-linker, HMDA as CNF cross-linker and DHT as physical cross-linker for both polymers, investigating the effect of single cross-linking and the synergetic effect of all cross-linkers.

ii) **<u>evaluation of the influence of blend ratio on polymeric scaffold</u>**

Reinforced nanocomposites were prepared by bending Gel with CNF in different ratio modulating their stability by means of dehydrothermal treatment (DHT) to obtain hybrid materials with different and improved mechanical performances without losing biocompatibility, chemical stability and flexibility.

iii) **<u>evaluation of the influence of hydroxyapatite on hybrid scaffold</u>**

Different protocols were studied to introduce hydroxyapatite (HA) in CNF or reinforced nanocomposite exploiting the biomineralization process in order to extend the application of these materials to bone regeneration, in which the presence of HA is essential due to its osteoinductive features.

HA was mineralized on CNF fibers in different ratio and also combined to polymer blend in order to develop the suitable material in terms of structure, chemical composition and mechanical properties for bone regeneration.

4.2. Influence of cross-linkers on polymeric scaffold

4.2.1. Synthesis process

To obtain a biopolymer blend with a concentration of 5 wt% and a Gel:CNF weight ratio of 10:1, 37.84 g of CNF suspension (1.06 ± 0.01 wt%) were heated to 40 °C before adding Gel aqueous solution (8.55 wt%). The blend was mechanically mixed for 1 hour and the pH was increased up to 7 by adding 0.1 M sodium hydroxide (Sigma Aldrich, Saint Louis, Missouri, USA) solution. The polymer blend was divided into four parts and processes with three different cross-linking techniques as schematically reported in Scheme 1 and detailed below. As last step, for the achievement of 3D porous structures, the cross-linked blends poured in Teflon mould (Ø=8 mm) were freeze-dried with a cycle including a controlled freezing ramp of 50 °C/h until -40 °C and two heating ramps, the first of 5 °C/h from -40 °C to -5 °C and the second 3 °C/h until 20 °C for about three days under vacuum conditions (P=0.086 mbar).

Sample Gel-CNF: porous scaffold composed of Gel and CNF. After the stabilization at pH 7, a portion of hydrogel was placed into Teflon moulds and freeze-dried following the above reported protocol. This scaffold was not cross-linked and used as reference materials.

Sample Gel-CNF+HMDA: porous scaffold composed of Gel and CNF cross-linked with hexamethylenediamine (HMDA). A portion of the blend was mixed with the 6 wt% of HMDA (Sigma Aldrich, Saint Louis, Missouri, USA) (HMDA/CNF) by adding a 1 wt% water solution, and placed into Teflon moulds, then treated in an oven at 80 °C overnight to promote the cross-linking reaction before freeze-drying.

Sample Gel-CNF+gen: porous scaffold composed of Gel and CNF (10:1 wt) cross-linked with genipin (gen). A portion of the blend was mixed with 1 wt% of gen (purity 98%, Wako Pure Chemical, USA) (gen/Gel) by adding a 1 wt% water solution and placed into Teflon moulds then left at room temperature for 48 hours to promote the cross-linking reaction before freeze-drying.

<u>Sample Gel-CNF+DHT:</u> porous scaffold composed of Gel and CNF cross-linked by dehydrothermal treatment (DHT). A portion of the blend was placed into Teflon moulds and freeze-dried. Further, those scaffolds were cross-linked by DHT performed in an oven at 160 °C, with a pressure of 0.001 mbar, for 48 hours.

<u>Sample Gel-CNF+HMDA+gen+DHT:</u> porous scaffold composed of Gel and CNF cross-linked with HMDA, gen and DHT. A portion of the blend was mixed with the 6 wt% of HMDA (HMDA/CNF) by adding a 1 wt% water solution and the 1 wt% of gen (gen/Gel) by adding a 1 wt% water solution. The hydrogel was then placed into Teflon moulds and incubated at 80 °C overnight to promote the cross-linking reaction. After that, the hydrogel was freeze-dried and, after drying, the scaffold was incubated at 160 °C under vacuum (P=0.001 mbar) for 48 hours for cross-linking by DHT.

As control sample for mechanical and in vitro test two control scaffolds of Gel differently cross-linked was developed.

<u>Sample Gel+gen (control)</u>: porous scaffold composed of Gel cross-linked with gen. The aqueous solution of Gel (8.55 wt %) was mixed with 1 wt% of gen (purity 98%, Wako Pure Chemical, USA) (gen/Gel) by adding a 1 wt% water solution and placed into Teflon moulds then left at room temperature for 48 hours to promote the cross-linking reaction before freeze-drying.

<u>Sample Gel+DHT (control)</u>: porous scaffold composed of Gel cross-linked with DHT. The aqueous solution of Gel (8.55 wt %) was placed into Teflon moulds and freeze-dried. Further, those scaffolds were cross-linked by DHT performed in an oven at 160 °C, with a pressure of 0.001 mbar, for 48 hours.

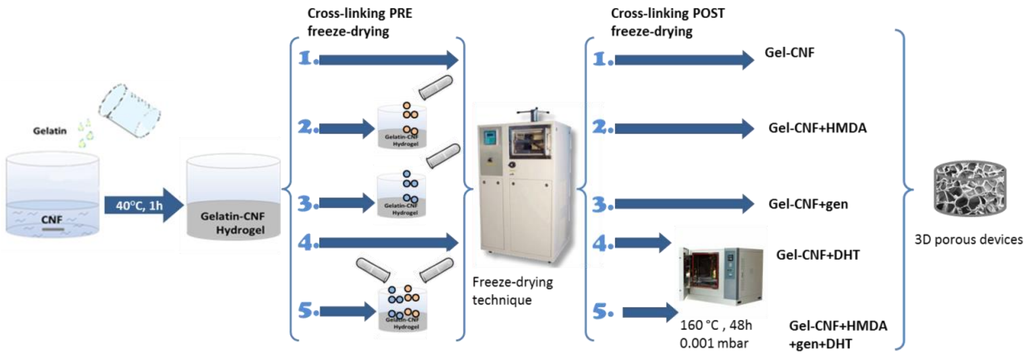

Figure 4.1. Schematic representation of experimental setup to produce Gel-CNF based scaffolds differently cross-linked.

4.2.2. Results & Discussion

Biomaterials play the fundamental role of load-bearing structure in tissue regeneration providing an appropriate microenvironment for neo tissue genesis. In this chapter, advanced scaffolds were designed combining the reinforcement properties of CNF with Gel matrix conveniently cross-linked with HMDA, gen and DHT to control the chemical stability of the blends in physiological conditions.[20,21] Finally, a freeze-drying process was applied ad optimized to obtain a tailored 3D porous structure. TEMPO-oxidized CNF was selected as reinforcing element because of its well noted biocompatibility, fibril stiffness, surface chemistry and gel formation capability.[15,22] The used CNF, with the aspect of a gel, is composed of individual nanofibrils, typically with widths of 3.5 - 20 nm and length in the µm range [23,24] that can be obtained as reversible or permanent gels through ionic or covalent linkages.[23] This type of cellulose nanofibrils expose on their surface, a significant number of aldehyde (211 ± 60 µmol/g) and carboxyl (764 ± 60 µmol/g) groups that are responsible to increase its hydrophilicity, playing a key role in cell-scaffold interaction, and suitable for the generation of covalent bonds with those of Gel molecules so as to enable a chemical stabilization of the nanocomposite.[12]

Different hydrogels were prepared using a fixed blend of CNF (1.1 wt%) and gelatin (8.55 wt%) with different cross-linking agents, these acts as cross-linking reacting with the amino groups of CNF and gelatin chains. Finally, the 3D porous scaffolds were obtained from hydrogels by the freeze-drying technique where a directional freezing and a following sublimation step gives formation of interconnected and organized pores where the size, homogeneity and orientation are dependent on ice crystal nucleation and growth.[25] This technique permit to modulate the porosity, a key characteristic in tissue engineering because the cell by means of pore can stick on the scaffold surface and proliferate.[26–28]

The scaffolds have the same blend concentration and polymer ratio, while they change cross-linking agents and cross-linking conditions (Table 4.1). Two different molecules were chosen as chemical cross-linking: HMDA and Gen. The first is a diamine commonly used as cross-linker for the chemical stabilization of biomaterials containing carboxyl or carbonyl functional groups through the generation of amide bonds.[23] Gen, is an aglycone derived extracted by the fruit of Gardenia Jasminoides Ellis, several works demonstrated that Gen reacts at room temperature with materials containing primary amine groups (e.g.

collagen, gelatin, chitosan), behaving as bridging molecule through the formation of covalently cross-linked networks.[6] Finally, a physical cross-linking was chosen as zero-length cross-linking: dehydrothermal treatment (DHT), a very simple and effective method selected for its noted efficiency in reducing the degradation rate of peptides like gelatin inducing a self-cross-linking reaction and thus avoiding the use of chemicals. It is based on a thermal treatment under vacuum condition, removing moisture and stabilizing polymer by promoting the formation of inter-chain peptide bonds.[6,29]

Table 4.1. Cross-linked protocols for CNF-gel scaffold.

Sample	**HMDA** **($_{wt}$% HMDA/CNF)**	**Genepin** **($_{wt}$% gen/gel)**	**Cross-linking condition** **(pre freeze-dried)**	**Cross-linking condition** **(post freeze-dried)**
Gel-CNF	None	None	None	None
Gel-CNF+HMDA	6 $_{wt}$%	None	80 °C 20 h	None
Gel-CNF+Gen	None	1 $_{wt}$%	20 °C 2 days	None
Gel-CNF+DHT	None	None	None	160 °C 2 days under vacuum
Gel-CNF+ HMDA+Gen+DHT	6 $_{wt}$%	1 $_{wt}$%	80 °C 20 h	160 °C 2 days under vacuum
Gel+Gen	None	$_{1wt}$%	20 °C 2 days	none

Gel+DHT	None	None	None	160 °C 2 days under vacuum

As highlighted from SEM analyses (Figure 4.2), all the developed scaffolds show highly porous structures with interconnected and homogeneously distributed pores characterized by rough surfaces. The pores size is slightly different in the samples due to the different cross-linking conditions used. However, the cross-linking treatment does not significantly affect the blend morphologies and the pores size ranges from 90 µm to 150 µm, suitable for cell permeation and proliferation.

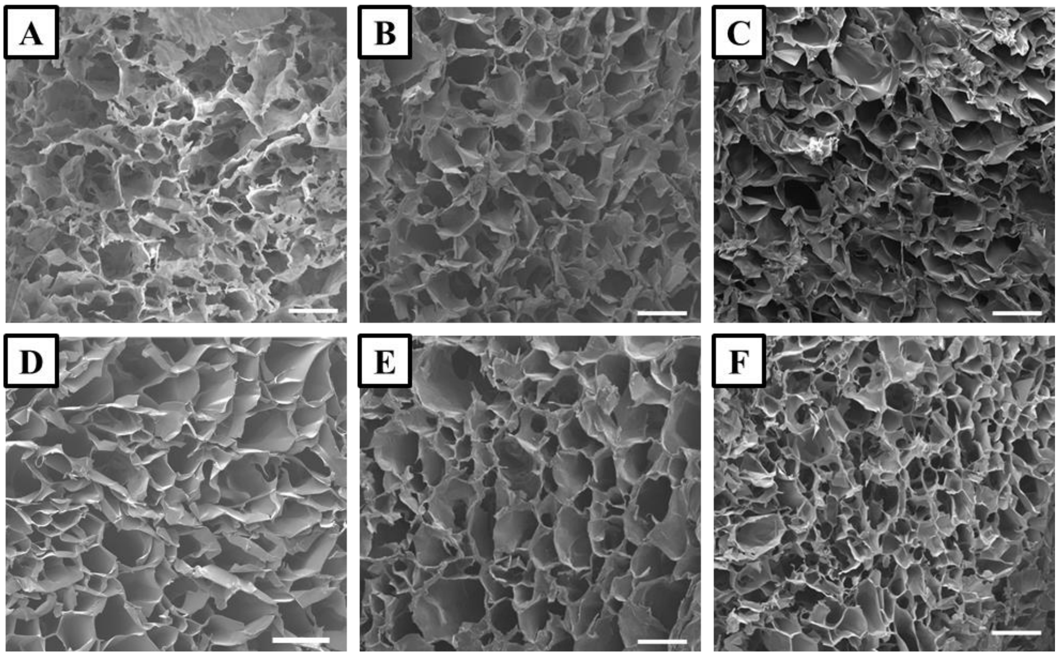

Figure 4.2. Cross-sectioned SEM images of (A) Gel+gen (control); (B) Gel-CNF; (C) Gel-CNF+HMDA; (D) Gel-CNF+gen; (E) Gel-CNF+DHT; (F) Gel-CNF+HMDA+gen+DHT. Scale bars are 200 µm.

Furthermore, Figure 4.3 shows the pores size of increases considerably from 200 µm to 300 µm when samples were swollen in simulated body conditions, 37 °C in PBS.

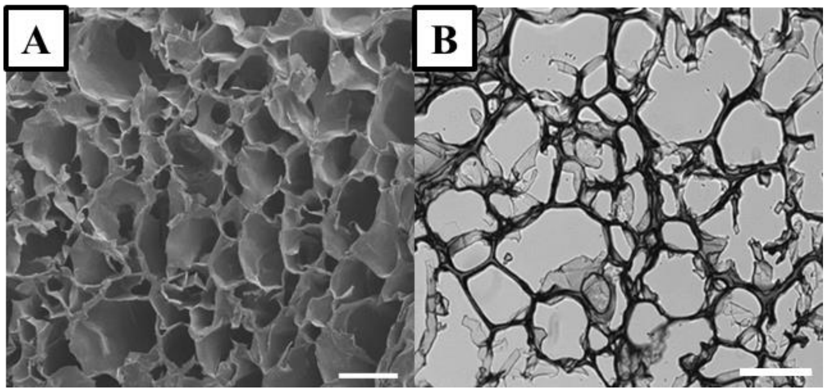

Figure 4.3. (A) Cross-sectioned SEM images of Gel-CNF+DHT; (B) Bright light images of swollen scaffold in simulated body condition(Gel-CNF+DHT). Scale bar is 200 µm.

The comparison between the surfaces of Gel-CNF and pure Gel (Figure 4.4) highlights the achievement of a nanocomposite material that comprises nanofibrils of CNF completely merged and homogenously distributed in the Gel matrix. As highlighted by Figure 4.4, the CNF confers a major superficial roughness to Gel matrix (white arrows) suitable to promote cell adhesion and scaffold colonization.

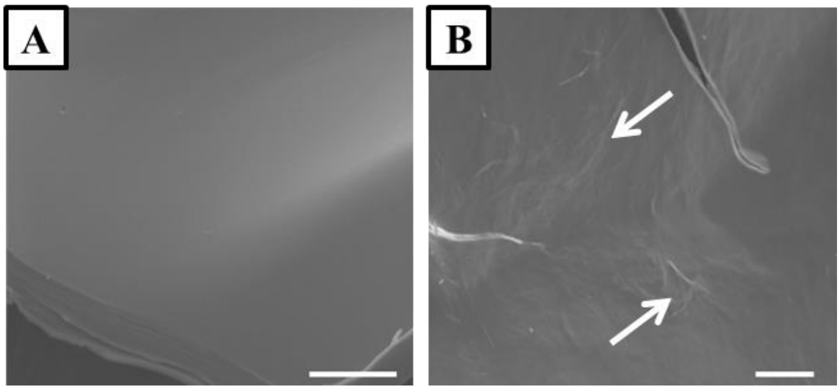

Figure 4.4. SEM images of surface of (A) Gel and (B) Gel-CNF scaffolds; scale bars are 20 µm.

The density and the porosity evaluated by means of the water squeezing method and the density method are reported in Table 4.2. The porosity test according to the SEM images shows a great porosity up to 95%. The different cross-linking techniques did not significantly affect this parameter as porosity was shown to be driven especially by the freeze-drying process (kept unvaried for all the protocols). While, the water squeezing method, revealing only the macropores volume percentage instead of the overall porosity, discloses an increase of the macro-porosities probably due to the thermal treatment performed during the cross-linking by DHT (samples Gel-CNF+DHT and Gel-CNF+HMDA+Gen+DHT). Although, taking into consideration that this method evaluates only the macropores volume percentage and not the overall porosity, a high porosity was observed. These data prove that the scaffolds have the suitable porosity requirement for the cell penetration and proliferation.

Table 4.2: Morphological parameters: pore size, density and porosity (%) of Gel-CNF scaffolds.

Samples	**Pore size (µm)** (n=32)	**Density** (g/cm^3)	**Porosity (%)**	
			Density method (total porosity)	**Water squeezing method** (macropores)
Gel-CNF	115 ± 23	0.054	95%	Not assessable
Gel-CNF+HMDA	124 ± 27	0.060	94%	Not assessable
Gel-CNF+gen	142 ± 29	0.056	94%	47%
Gel-CNF+DHT	148 ± 32	0.050	94%	74%
Gel-CNF+HMDA +gen+DHT	91 ± 21	0.040	95%	76%

Those evidences highlight that our approach, selected for the improvement of mechanical performances and life-time of Gel-based scaffold, does not negatively affects the overall Gel matrix characteristics and microstructure and allows the achievement of highly porous, interconnected and homogenous pore networks, providing suitable space for vascularization and tissue ingrowth. Moreover, the major roughness of the inner surface of pores due to the exposure of CNF fibrils is also suitable for the improving of cell attachment.

A thermogravimetric analysis (Figure 4.5) of gelatin, CNF and CNF-gelatin was performed in order to determine the degradation temperature of both the native polymers, in addition to assess their stability in the operating conditions set up for the DHT treatment. The thermogravimetric curves shows that until 180-200°C the weight loss refers to the water loss that is different depending on the interactions: at 40-60 °C the free water is released, at 80-120°C the water linked through hydrogen bonds is released and up to 160°C water strongly linked through polar interaction is released. While the degradation temperature of all samples (Gel, CNF and their blend) were around 265 °C, 220 °C and 260°C respectively. After that, the graphs show two different weight losses at 260-380°C and 410-700°C that correspond to the thermal (II) and oxidative decomposition (III) of both gelatin and CNF. Therefore, these spectra confirm our hypothesis that the degradation temperatures are below 160 °C corresponding to cross-linking temperatures, thus DHT cross-linking temperature is not dangerous for the polymer integrity.

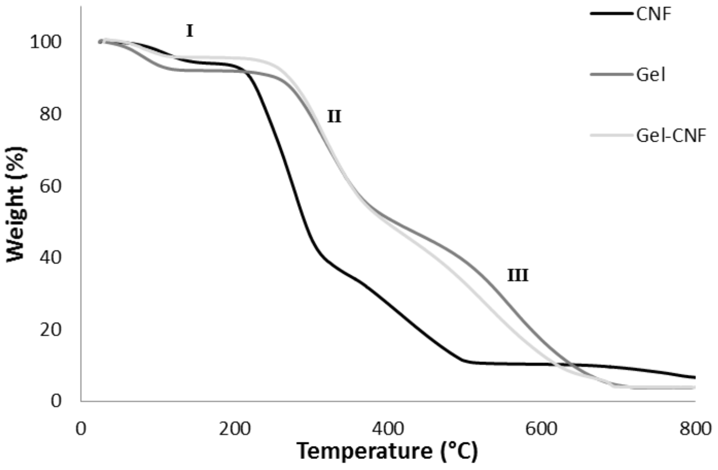

Figure 4.5. TGA spectra of pure polymers (Gel and CNF) and uncross-linked scaffold (Gel-CNF).

In order to determine the reaction efficiency between gelatin and cellulose nanofibers with cross-linking agents, the amount of the unreacted free amines in the chemically cross-linked samples was measured spectrophotometrically following a TNBS assay. The degree of cross-linking was calculated by comparing the absorbance of cross-linked samples with the control sample, i.e. uncross-linked Gel-CNF. An increase from 1.5% to 15% was detected, meaning that the cross-linking agents affects the degree of cross-linking (Table 4.3).

Table 4.3. Summary of stability parameters of Gel-CNF cross-linked scaffolds

Samples	Cross-linking Degree	Swelling ratio (after 24 h)	Degradation % (after 28 days)
Gel-CNF	0 %	Not assessable	Not assessable
Gel-CNF+HMDA	1.5 %	Not assessable	Not assessable
Gel-CNF+gen	8.7 %	10.6 ± 1.8	26.6 ± 1.8 %
Gel-CNF+DHT	13 %	7.4 ± 0.3	5.5 ± 1.4 %
Gel-CNF+HMDA +gen+DHT	15 %	10.8 ± 0.6	6.2 ± 1.4 %

To predict the effect of the different cross-linking treatments on scaffolds' stability in vivo, swelling and degradation tests were performed assessing the scaffold capacity to absorb fluids from the surrounding medium and its degradation rate in the long term period, up to 28 days (Figure 4.6).

As predictable from the cross-linking degree, samples Gel-CNF and Gel-CNF+HMDA were highly unstable and completely degraded in PBS at 37 °C within 72 hours (Table 4.3). Samples Gel-CNF+gen, Gel-CNF+DHT and Gel-CNF+HMDA+gen+DHT, highly cross-linked, highlight suitable swelling ratio and degradation rate, thus, based on these results, only these samples were further characterized. The swelling test (Figure 4.6) shows that the porosity of the samples allows the absorption of water, about 8-11 times more than the dried sample. Furthermore, the swelling is fast and does not change during the time, meaning no initial degradation and no loss of structure. The sample cross-linked with DHT showed lower swelling ratio. This treatment is based on the formation of amide linkages between carboxylic and amino residues. Tis reaction, however, reduces the scaffold hydrophilicity and, consequently, the swelling ratio.[14]

Finally, the degradation time is an important parameter for the scaffolds used in tissue regeneration because it should not be so fast because the cells need time to regenerate the tissue and in this initial time the biomaterial plays a fundamental role as a load-bearing structure. As Figure 6 shows, after 28 days at 37 °C in PBS, the samples lose from 10% to 20% of their overall weight preserving macroscopically their shape and structure. To conclude, for the composition of polymer nanocomposite considered, the DHT demonstrate to be the most suitable cross-linking approach for the achievement of chemically stable scaffolds (Samples Gel-CNF+DHT and Gel-CNF+HMDA+gen+DHT) in terms of cross-linking degree and stability against to the degradation.

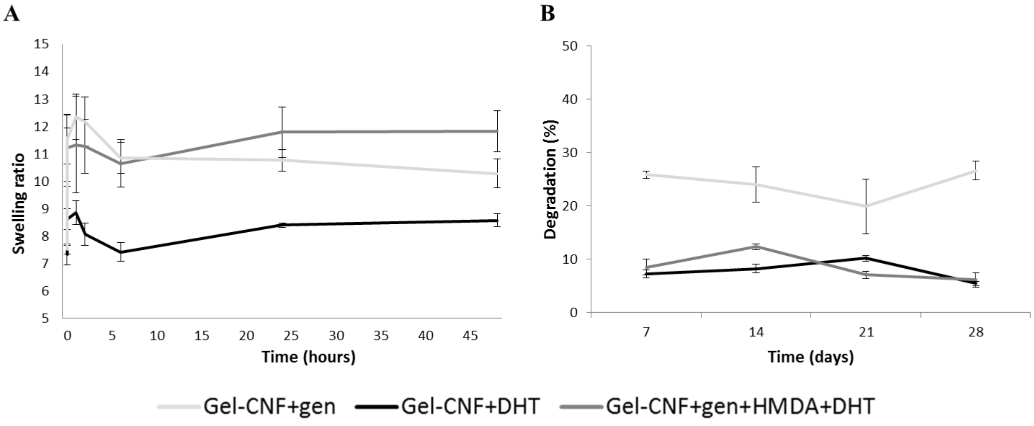

Figure 4.6. (A) Swelling behavior and (B) degradation rate of Gel-CNF cross-linked scaffolds, performed in PBS at 37 °C.

Since the scaffolds are expected to be used in a hydrated environment, it is relevant to evaluate their biomechanical behavior in *in vivo*-like conditions, in terms of temperature and hydration state. It was possible by using DMA apparatus, allowing to setup temperature and dry or wet environment before the tests, that we used to evaluate the mechanical performances of the best formulation of cross-linked nanocomposite scaffolds in comparison with the control samples (Gel+gen and Gel-DHT). Figure 7A and 7B show that Young's modulus increased drastically when 10 wt% of CNF was added to the Gel as nano-reinforcement and scaffold were cross-linked by DHT; from 17.9 kPa (Gel+gen) and 22.9 kPa (Gel+DHT) to 54.7 kPa (Gel-CNF+DHT) and 35.2 kPa (Gel-CNF+HMDA+gen+DHT). The compressive strength (Figure 7A) improves from 20.9 kPa (Gel+gen) and 24.1 kPa (Gel+DHT) to 28.3 kPa (Gel-CNF+DHT) and 25.6 kPa (CNF+HMDA+gen+DHT) and follows the same trend of Young's modulus. Comparing samples with two controls, it was clear that both CNF and cross-linkers affected Young modulus and both are essential for the development of biomaterial for tissue regeneration because CNF is needed to improve the mechanical properties, however, without cross-linking techniques samples are instable in wet condition that mimic the *in vivo* environment.[6,29,20]

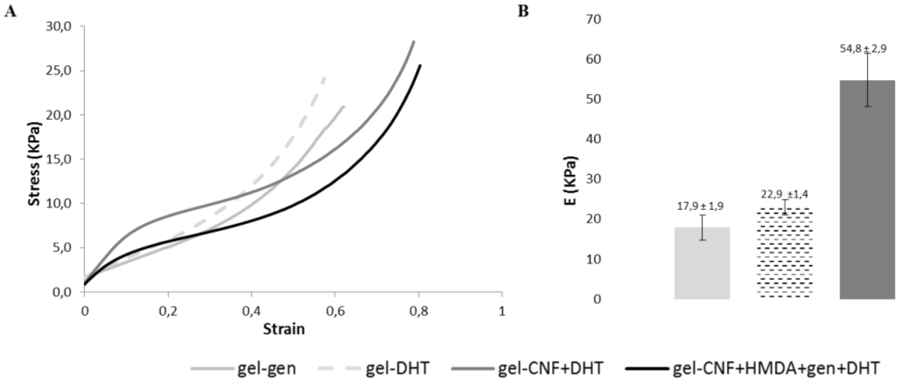

Figure 4.7. Compressive mechanical test of control sample Gel+gen (light grey), Gel+DHT (dotted light grey) sample Gel-CNF+DHT (grey) and sample Gel-CNF+HMDA+gen+DHT (black), performed after immersion in PBS at 37 °C overnight. (A) Average stress-strain curves (n=5 specimens); (B) Young's modulus calculated as the slope of the stress-strain curve in a range from 1-10 % (n=5 specimens, data are mean ± SEM.

In figure 4.8A were reported the viscoelastic behavior of the scaffolds when subjected to different frequency in the range from 0.1 to 10 Hz. From the graph is possible to observe that the storage modulus (E') of both samples (Gel-CNF+DHT and Gel-CNF+HMDA+gen+DHT) increases in comparison to the control (Gel+gen). In particular, the E' of sample Gel-CNF+DHT increases from 60.8 kPa to 107.7 kPa, and of sample Gel-CNF+HMDA+gen+DHT from 34.8 kPa to 63.6 kPa. Whereas, both control samples (Gel+gen and Gel+DHT) has a low E' and does not increase significantly.

Finally, the creep tests (Figure 4.8B) show that all samples when subjected to a static stress (0.01 MPa), identified with a preliminary linearity study (data no shown), for 15 min can recover almost completely their original shape.The spectra shows, ideed, that the final strain is less than 10 % and the strain recovery is close to 80 %.

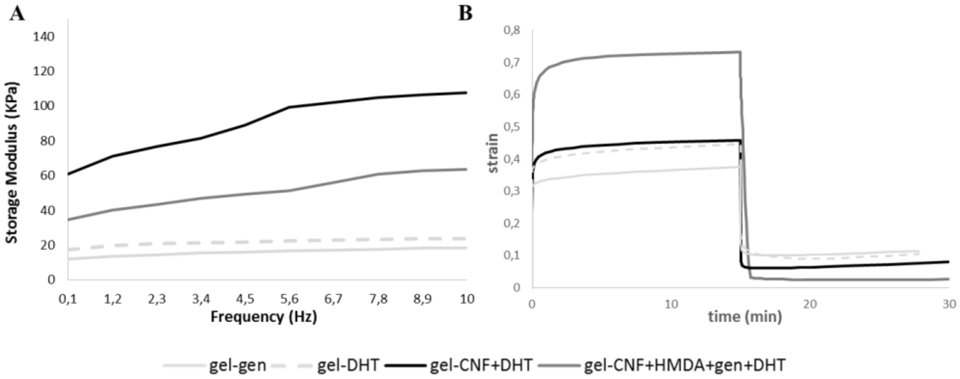

Figure 4.8. Compressive mechanical test of control sample Gel+gen (light grey), Gel+DHT (dotted light grey) sample Gel-CNF+DHT (grey) and sample Gel-CNF+HMDA+gen+DHT (black), performed after immersion in PBS at 37 °C overnight. (A) Average storage modulus (E')-frequency curves measured from 0.1 to 10 Hz (n= 5 specimens); (B) Average creep curves obtained after a creep time of 15 min and a recovery time of 15 min (n=5 specimens).

The differences establish in Young's modulus, viscoelastic properties and creep behavior of the examined scaffolds indicate that by selecting a proper cross-linking technique can be improved and tailored the mechanical behavior of these nanocomposite polymer scaffolds.[30,31] Both nanocomposite scaffolds Gel-CNF+DHT and Gel-CNF+HMDA+gen+DHT highlight promising features for application in tissue regeneration. They are characterized from a well interconnected porous structures, demonstrate good hydration capabilities and preserve their structural integrity and loading-bearing properties also in wet conditions.

The features highlighted for samples Gel-CNF+DHT and Gel-CNF+HMDA+gen +DHT make them suitable candidates for in vivo application, therefore, it is important to evaluate, by in vitro tests, their cytotoxicity, cell-scaffold interaction and ability to support cell colonization. In the current study, the short-term effect of leachable from cross-linked scaffolds was evaluated by exposing L929 cells to the extract of these scaffolds after soaking in culture medium for 24 h. Unlike cells treated with phenol, which served as toxic control and associated with apoptosis (Figure 4.9A_i), treatment with culture medium alone (nontoxic control) showed many cells with spindle-like morphology, indicating that cells are spreaded (Figure 4.9A_{ii}). Similarly, no significant morphological changes were observed in the cells treated with extracts of the tested scaffolds, compared to the nontoxic control (Figure 4.9).

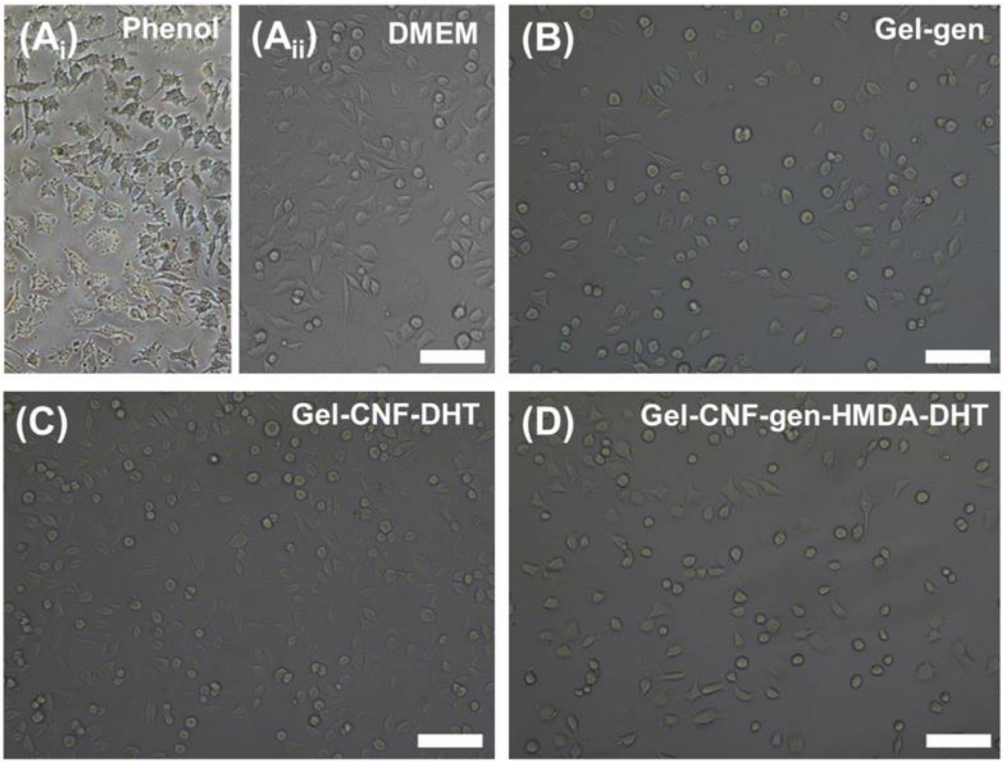

Figure 4.9. Morphology of L929 fibroblasts after treatment with extracts of cross-linked scaffolds for 24 h. (A) Cells treated with toxic and nontoxic media; (Ai) Toxic culture medium containing phenol, showing cells with apoptotic features (Aii) Nontoxic culture medium showing spreading of the cells. (B) Gel+gen. (C) Gel-CNF+DHT. (D) Gel-CNF+HMTA+gen+DHT. No morphological differences were found between scaffold extracts and nontoxic control. Cells treated with phenol. Scale bar=100 µm.

The nontoxic effect of the extracts was also confirmed with the Live/Dead assay (Figure 4.10). Most of cells treated with the toxic control appeared red, indicating the toxicity of the phenol (Figure 4.10Ai). In contrast, the fluorescent images of the cells treated with extracts of the test scaffolds showed that the majority of the cells were alive (green) with viability comparable to the nontoxic control (Figure 4.10Aii-D). The WST-1 results showed no toxic effect of the scaffold: compared with the nontoxic control, there was a significant increase in mitochondrial activity in the cells treated with the extract of Gel-CNF+DHT (Figure 4.10E).

This could be due to the absence of chemical cross-linkers in this sample. In tissue engineering, scaffolds should possess appropriate physicochemical parameters to support cell attachment and proliferation without toxicity. Generally, both gelatin and TEMPO-oxidized CNF-based materials have shown biocompatibility and non-cytotoxic characteristics when tested with different cells.[32] Hua et al. reported the direct and indirect nontoxic effect of TEMPO-oxidized CNF films and their extracts on different human cells.[33] Alexandrescu et al. showed that the TEMPO-oxidized CNF are not cytotoxic against fibroblast cells.[34] However, cross-linking process of hydrogels could alter the physicochemical structure and subsequently affect the cell respond. It was reported that the cross-linking of CNF with polyethyleneimine (PEI), significantly, reduced the viability of fibroblasts. In comparison with glutaraldehyde, gen showed comparable cross-linking ability but with much lower cytotoxicity. However, there are contradicting findings on the cytotoxicity of gen. For example, it was reported that gen inhibited the growth of bone and cartilage cells in a dose dependent manner within 24 h. Yeom et al. reported that hyaluronic hydrogel cross-linked with HMDA is biocompatible when implanted in mice.[35] However, the cytotoxicity of HMDA is not well investigated as a cross-linker in the literatures.

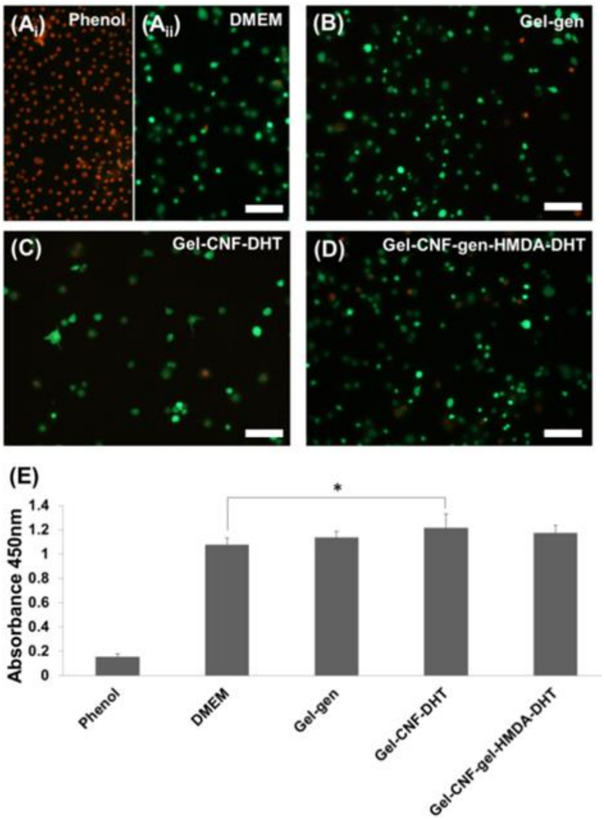

Figure 4.10. Cell viability and mitochondrial activity of L929 fibroblasts treated with scaffold extracts for 24 h. (A) Cell treated with nontoxic and toxic media; (Ai) Nontoxic culture medium showing live cells (green) and fewer dead cells (red) (Aii) Toxic culture medium with phenol showing that majority of the cells are dead (red). (B) Gel+gen. (C) Gel-CNF+DHT. (D) Gel-CNF+HMDA+gen+DHT. The results for the scaffold extracts were comparable to those for the nontoxic control, with more green cells than red. Scale bar = 100 µm. (E) Mitochondrial activity by

WST-1 showing the nontoxic effect of the scaffold extracts. Data are presented as the mean ± the standard deviation (n≥4). Statistical significance=*P<0.05.

Figure 4.11 shows the nontoxic effect of the cross-linked scaffolds when seeded with cells. The Live/Dead assay showed high viability of cells cultured on the scaffolds. More cells were found to attach to Gel-CNF scaffold cross-linked with gen, HMDA and DHT more than to Gel+gen scaffolding. This finding was confirmed by the data from the WST-1 assay (Figure 4.11C). With respect to cell attachment after 24 h, there was no significant difference between Gel-CNF+DHT and Gel-CNF+HMDA+gen+DHT. The addition of CNF in conjunction with physical and chemical cross-linking increased the rigidity of the scaffolds. Increasing the rigidity of cross-linked hydrogels has previously been reported to increase cell attachment and proliferation.[36] On the other hand, Bott et al. reported that the proliferation of fibroblast encapsulated in the PEG gels increased with decreasing the stiffness. Therefore, it is likely that Gel-gen-HMDA-DHT scaffold had a proper mechanical characteristic between the high rigidity of the Gel-CNF-DHT scaffold and the low rigidity of Gel-gen scaffold, thus supported higher cell proliferation.[37]

Overall, when tested in direct and indirect cultures with mouse fibroblasts for 24 h, the addition of CNF to Gel matrix cross-linked with HMDA and/or gen did not trigger a cytotoxic response.

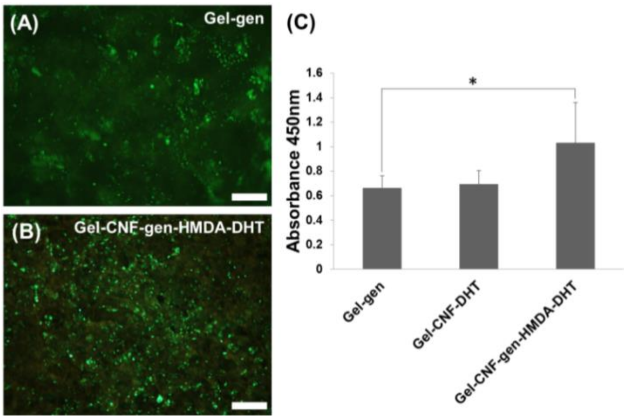

Figure 4.11. Cell viability and mitochondrial activity of L929 fibroblasts directly seeded onto scaffolds for 24 h. (A) Gel+gen. (B) Gel-CNF+HMDA+gen+DHT. Scale bar=100 µm. (C) Mitochondrial activity by WST-1 showing the nontoxic effect of the HMDA cross-linked scaffold compared to Gel+gen. Data are presented as the mean ± the standard deviation (n≥4). Statistical significance=*P<0.05.

4.3. Influence of blend ratio on polymeric scaffold

4.3.1. Synthesis process

To obtain a biopolymer blend with a final concentration of 1.1 wt% and a Gel:CNF weight ratio ranging from 2:1 to 1:1 and 1:2; 300g of CNF suspension (1.09 ± 0.01 wt%) were heated to 40 °C and separately a Gel aqueous solution (1.1 wt%; 3.3 g dissolved in 300 mL of ultrapure water). A specific amount of Gel solution was added to a specific amount of CNF suspension as described in the table below, in order to obtain the desired Gel:CNF weight ratio Moreover, blends were mechanically mixed for 1 hour. As last step, for the achievement of 3D porous structures, blends poured in Teflon mould (Ø=8 mm) were freeze-dried. Freeze-drying cycle included a controlled freezing ramp of 50 °C/h until -40 °C and two heating ramps, the first of 5 °C/h from -40 °C to -5 °C and the second 3 °C/h until 20 °C for about three days under vacuum conditions (P=0.086 mbar). Finally, scaffolds were cross-linked by dehydrothermal treatment (DHT) performed in an oven at 160 °C, with a pressure of 0.001 mbar, for 48 hours.[13,38,39]

Table 4.4. Synthesis and cross-linking protocols for CNF-gel scaffold.

Sample	Gel solution (1.1wt%)	CNF suspension (1.1 wt%)	Blend concentration (wt%)	Cross-linking condition
Gel+DHT	100 g	---	1.1 wt%	160 °C 2 days under vacuum
CNF+DHT	---	100 g	1.1 wt%	160 °C 2 days under vacuum

CNF-gel (1:1)+DHT	50 g	50 g	1.1 wt%	160 °C 2 days under vacuum
CNF-gel (2:1)+DHT	70 g	35 g	1.1 wt%	160 °C 2 days under vacuum
CNF-gel (1:2)+DHT	35 g	70 g	1.1 wt%	160 °C 2 days under vacuum

4.3.2. Results&Discussion

The blending processes are designed to combine the best properties of two bio-polymers and to obtain hybrid materials with improved mechanical performances without losing biocompatibility, chemical stability and flexibility. In particular, several blend compositions were studied to evaluate the different mechanical properties and degradability in simulated body conditions in order to obtain a different cell differentiation. Gelatin has been selected due to its easy production, low cost and high biocompatibility, while CNF have been selected due to its biocompatibility, exceptional mechanical properties, high crystallinity and surface area. The blends were performed varying the polymer ratio, but keeping unchanged the final blend concentration. Finally, the blends were freeze-dried and cross-linked using a dehydrothermal cross-linking treatment (DHT) at 160°C in vacuum.

The scaffold morphology plays a crucial role to be used in biomedicine because a suitable porous structure allows the adhesion, cellular proliferation and permeation of nutrients and oxygen. SEM images of the developed scaffolds show a similar pore sizes while the pores isotropy is slight different because the introduction of CNF decrease and avoid the typical gelatin aligned morphologies highlighted in the SEM images of sagittal sectioned scaffolds (Figure 4.12). However, these data confirm that modifying the CNF:Gel ratio the scaffold morphology does not significantly change. As SEM images shows, all the scaffolds show rough surfaces and a porous structure with interconnected pores homogeneously distributed throughout the whole cross-sectioned structure typical of freeze-dried gelatin scaffold.[6] The pores size ranges from 90 µm to 150 µm and it is suitable for cells proliferation.

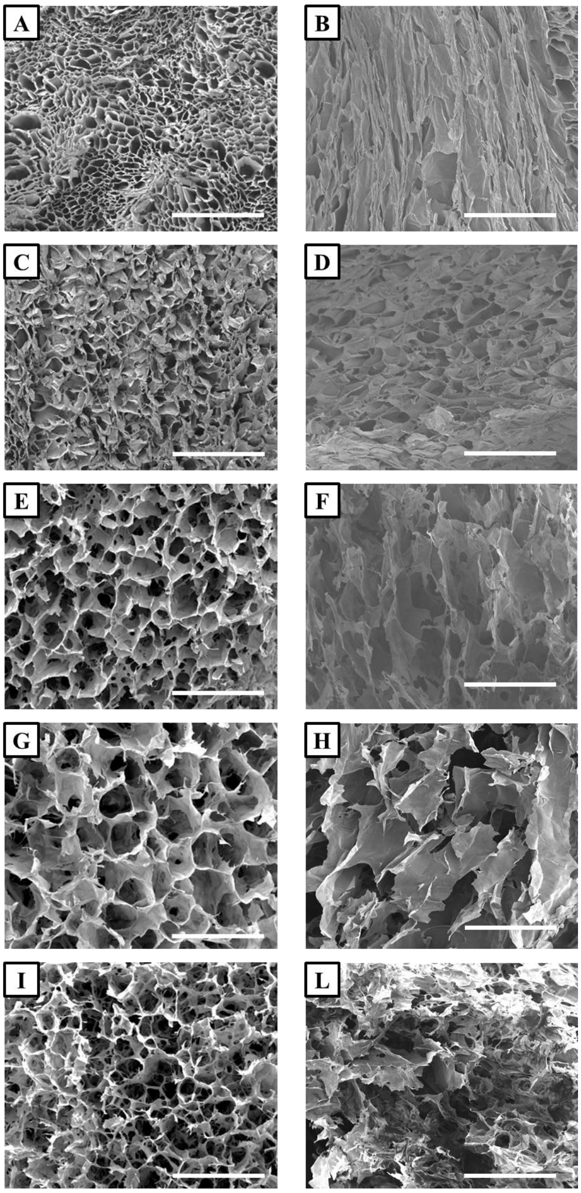

Figure 4.12. Cross- and sagittal-sectioned SEM images of (A,B) Gel; (C,D) CNF; (E,F) CNF-Gel (1:1); (G,H) CNF-Gel (2:1); (I,L) CNF-Gel (1:2) cross-linked with DHT. Scale bars are 500 µm.

Density and porosity evaluated by density and water squeezing methods are reported in table 4.5. The porosity test according to the SEM images shows a great porosity up to 90%, especially, observing the porosity measured by water squeezing method. Different blending ratio did not significantly affect this parameter that in all blends is higher than pure materials (Gel and CNF). This behavior depends on different ways to self-assembling of polymers creating nano and microporosity that differently affect the porosity. The self-assembling of CNF-gel blends create big pores detecting macro-porosity significantly higher than pure materials suitable for cell adhesion and colonization. Porosity of different blends is very similar because polymer ratio does not affect this parameter, but it is driven especially by the freeze-drying process (kept unvaried for all the protocols).[25] These data prove that scaffolds have the suitable porosity requirement for the cell penetration and proliferation. The wettability of the CNF-gel surfaces was measured using a static water contact angle on films and the results are shown in Table 4.5. All the materials showed high contact angles, more than 70, indicating that all these materials had poor hydrophilicity. Nevertheless, the cross-linking process and the different polymer ratio induce little changes. Water affinity depend on the number of hydrophilic functional groups present into the blend.[38] For this reason, blends show a higher hydrophilicity than raw materials that could be due to the formation of a molecular network through covalent bond increasing functional groups, however the increase of hydrophilicity is not significantly increased.

Table 4.5. Summary of porosity and contact angles of CNF-Gel scaffolds.

Samples	**Porosity**		**Contact angles**
	Density method	**Water squeezing**	
Gel+DHT	98 %	87 %	88.9 °
CNF+DHT	94 %	48 %	72.8 °
CNF-gel(1:1)+DHT	99 %	96 %	99.8 °
CNF-gel(2:1)+DHT	99 %	96 %	87.7 °

CNF-gel(1:2)+DHT	99 %	94 %	94.1 °

In order to determine the reaction efficiency between gelatin and cellulose nanofibers themselves and with cross-linking agent, the amount of the unreacted free amines in the chemically cross-linked samples was measured by spectrophotometrically following a TNBS assay (table 4.6). The degree of cross-linking was calculated by comparing the absorbance of cross-linked samples with the control sample, i.e. uncross-linked CNF-Gel (column left) or with pure gel (column right). Data showed in table 4.6 demonstrated that samples have a different cross-linking degree influenced by cross-linking agent and CNF-Gel bond depending on the samples.[40] In all samples, cross-linking is suitable to preserve the whole shape and in particular, the formation of covalent bound between gel and CNF is clearly visible. The polymer ratio affects the covalent bound because increasing the amount of CNF allows to increase the cross-linking degree and so the covalent bounds as table 4.6 confirmed proving the creation of a blend and not simply a mixing between polymers. The evaluation of cross-linking degree demonstrates that by blending different polymeric matrices it is possible to engineer new nano-composite materials with improved properties respect to the original raw materials.

Table 4.6. Cross-linking degree for CNF-Gel with different polymeric ratio.

Samples	**Cross-linking degree** **(blank = uncross-linked scaffold)**	**Samples**	**Cross-linking degree** **(blank = gel)**
Gel+DHT	32 %	**Gel**	0 %
CNF+DHT	21 %	**CNF:gel (1:1)**	16 %
CNF-gel (1:1)+DHT	22 %	**CNF:gel (2:1)**	49 %

CNF-gel (2:1)+DHT	56 %		**CNF:gel (1:2)**	5 %
CNF-gel (1:2)+DHT	48 %			

Swelling ratio was carried out to evaluate the scaffold capacity to absorb water and, subsequently, cell medium that is essential for cells migration inside scaffold and cells proliferation (Figure 4.13). It shows that the porosity of the samples allows the absorption of water, about 40-70 times more than the dried sample, the swelling of all blends is bigger than the pure raw materials. Furthermore, the swelling is fast and does not change during the time, meaning no initial degradation and no loss of structure. As reported in figure 4.13, after 28 days at 37 °C in PBS the samples lose from 10% to 20% of their overall weight preserving macroscopically their shape and structure. This is an important data because a porous scaffold for tissue regeneration must be biodegradable, but the degradation time is an important parameter to consider for the scaffold evaluation because a too fast degradation doesn't allow cells to regenerate the damage tissue.

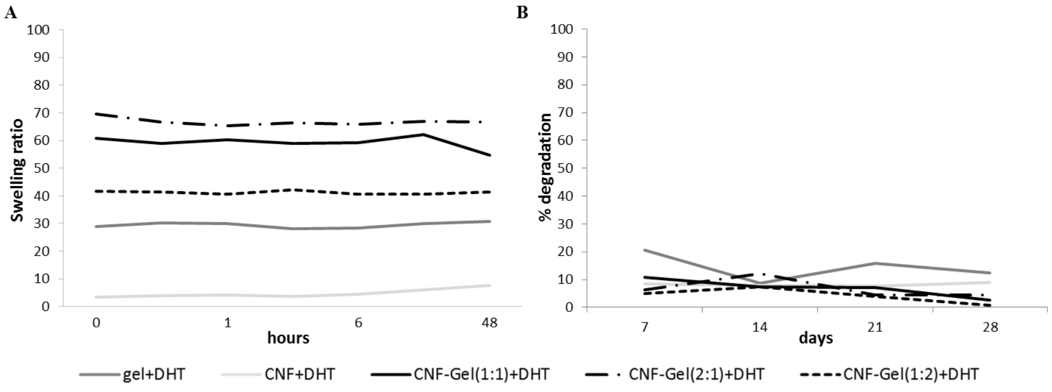

Figure 4.13. a) swelling behavior; b) scaffold stability in wet conditions in PBS at 37°C of CNF-Gel scaffolds.

Since the scaffolds are expected to be used in a hydrated environment, it is relevant to evaluate their biomechanical behavior in simulated body conditions, in term of temperature and wet state by using DMA apparatus. Figure 4.14 shows the mechanical properties of polymeric blends with different CNF:Gel ratio in comparison to pure gel e

CNF scaffolds, evaluated under compressive mode. What was observed is that the Young's modulus increased when CNF was introduced as a nano-reinforcement in different ways depending on the CNF:Gel ratio (Figure 4.14). CNF has high Young modulus (77.38 kPa), for this reason it was chosen as nano-reinforcement for Gel (2.48 kPa). In all blend Young modulus increased, but only where CNF is in higher ratio, CNF-gel (2:1), in significantly way, it displayed a Young modulus of 6.52 kPa, while CNF-gel ratio of 1:1 and 1:2 were 3.6 kPa and 2.9 kPa, respectively. Comparing samples with two pure materials, it was clear that the amount of CNF positevely affected Young modulus confirming that CNF is needed to improve the mechanical properties important for tissue regeration.[40]

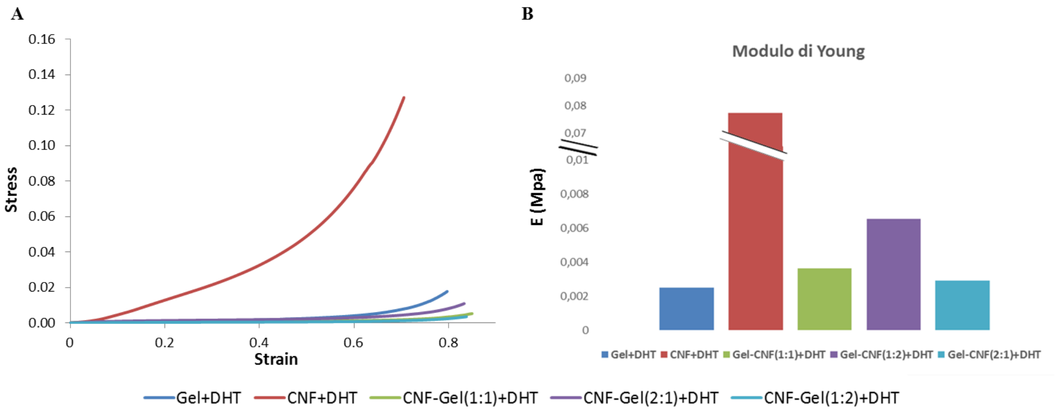

Figure 4.14. Compressive mechanical test of CNF-Gel scaffolds with different Gel:CNF ratio previously immersed in PBS at 37 °C overnight. A) Average stress-strain curves (n=5 specimens); b) Young's modulus calculated as the slope of the stress-strain curve in a range from 1-10 % (n=5 specimens, data are mean ± SEM.

Figure 4.15 shows the viscoelastic properties of the scaffolds when they were subjected to different frequency in a range of 0.1-10 Hz, this test is important to simulate in vivo stress conditions and evaluate the scaffolds behavior. The obtained data, demonstrate that the storage modulus (E') of all groups has different values in comparison to pure raw materials. CNF showed a higher storage modulus that increases from 35.9 kPa to 78.6 kPa, while Gel storage modulus increases from 13.2 kPa to 21.6 kPa. All blends increases storage modulus, it is different depending the amount of CNF: with low amount of CNF, modulus increase from 0.9 kPa to 13.1 kPa and 0.5 kPa to 0.8 kPa for CNF-gel of 1:1 and 1:2 respectively. With CNF-gel of 2:1 the modulus is higher and increases from 22.1 kPa to 21.4 kPa meaning that blend behavior is not intermediate between pure materials, but blend demonstrate a new behavior. All materials, except for CNF, increase their storage modulus of about 50% from 0.1 Hz to 10 Hz.

Finally, the creep allows to evaluate the behavior of the material when subjected to high stress for a specific time. The preliminary linearity study (data no showed) allows to identify the suitable stress value to apply on all samples. The creep tests (figure 4.15B) show that all the scaffolds after being subjected to a static stress (0.01 MPa) for 15 min can recover almost all their shape, showing an elastic behavior. Comparing with pure materials that displayed a strain recovery of 71% and 59% (Gel and CNF respectively), only CNF-Gel (1:1) revealed a low strain recovery of about 55%. Contrariwise, CNF-Gel blend (2:1) and (1:2) highlighted a good strain recovery higher than pure materials of about 85% and 84% respectively. In conclusion, was clearly demonstrated that by changing the polymeric ratio it is possible to develop scaffolds with different mechanical performances in terms of stiffness and elasticity.[41]

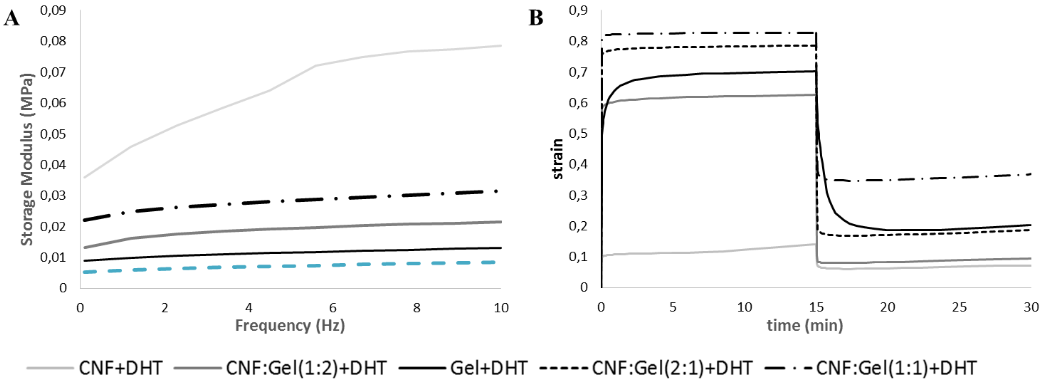

Figure 4.15. Compressive mechanical test of CNF-Gel scaffolds with different Gel:CNF ratio previously immersed in PBS at 37 °C overnight. A) average storage modulus (E')-frequency curves appreciated from 0.1 Hz to 10 Hz (n= 5); b) average creep curves appreciated in a creep time of 15 min and a recovery time of 15 min (n=5).

The differences establish in Young's modulus, viscoelastic properties and creep behavior of the examined scaffolds indicate that by selecting a proper CNF-gel ratio can be improved and modulate the mechanical behavior of these nanocomposite polymer scaffolds.[30] [31]

All nanocomposite scaffolds highlight promising features for application in tissue regeneration. They are characterized from a well interconnected porous structures, demonstrate good hydration capabilities and preserve their structural integrity and loading-bearing properties also in wet conditions. Furthermore, as literature reported, the biomaterials properties such as stiffness, mechanical stimulation, surface topography can influence cellular functions and direct stem cells differentiation.[42] Therefore, cells feel and respond to some characteristics of their substrate enhancing tissue specific extracellular matrix deposition and direct stem cell differentiation. With this purpose, the possibility to modulate the mechanical properties changing the polymers ratio in a blend allows to design a multifunctional material capable to regenerate different human tissue.

The materials cytocompatibility were tested with MG-63 cell line, immortalized fibroblasts from mice. Both a qualitative and quantitative viability assay tests and cellular morphology analysis were performed. The qualitative viability assay performed via live/dead kit showed an overall better cytocompatibility for the CNF:Gel (2:1) (Figure 4.16). This tendency was confirmed by the quantitative viability test performed via MTT assay, were the revealed absorbance is directly related to the quantity of metabolically active cells present in the sample. The assay showed a higher increase in absorbance over-time for the CNF:Gel (2:1) samples over the other formulations. Moreover, the cellular morphology observations conducted via SEM revealed that the cells grew on the CNF:Gel (2:1) were the ones showing the best cytoplasmic extensions and cytoskeleton spreading, coherent with a non-stress cells condition (Figure 4.17). Overall the CNF:Gel (2:1) chemical composition had proved to be the best cell-growth environment among the tested compositions.

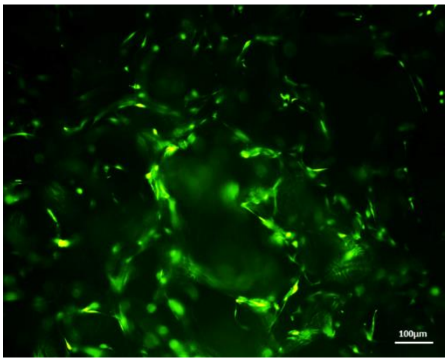

Figure 4.16. Cell viability analysis performed with the Live/Dead kit where Calcein AM label living cells in green, Ethidium homodimer-1 label dead cells in red. MG-63 seeded on EC04, image taken after 3 days from seeding. Scale bar: 100µm

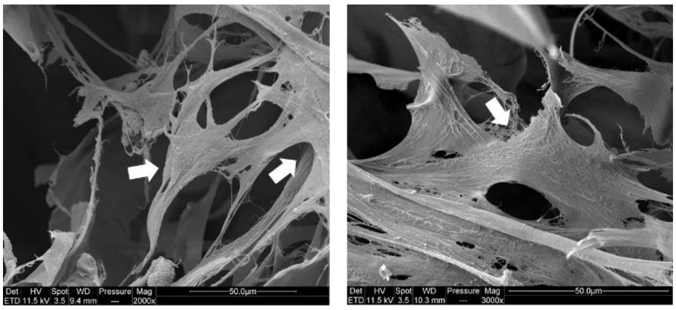

Figure 4.17. SEM observations of MG-63 cultured on EC04 until day 3 after seeding. White arrows pointing cells attached on the biomaterial surface, showing healthy cellular morphology. Scale bar: 50µm.

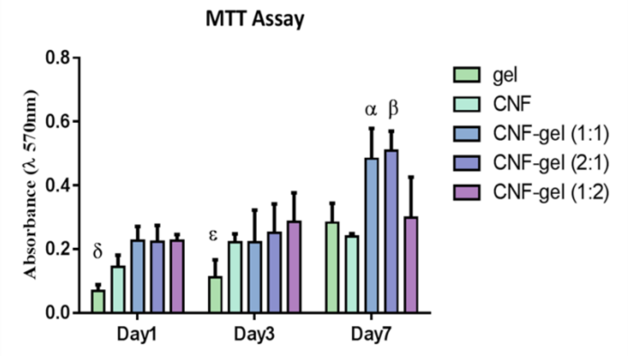

δ = gel vs CNF-gel (1:1)/CNF-gel (2:1)/CNF-gel (1:2), $P \leq 0,05$. e = gel vs CNF-gel (2:1), $P \leq 0,05$; vs CNF-gel (1:2), $P \leq 0,01$. α = CNF-gel (1:1) vs gel, $P \leq 0,001$; vs CNF, $P \leq 0,0001$; vs CNF-gel (1:2) $P \leq 0,01$. β = CNF-gel (2:1) vs gel/CNF/CNF-gel (1:2), $P \leq 0,0001$.

Figure 4.18. Quantitative analysis of cell proliferation among the samples at 1, 3 and 7 days after seeding (n=3). Scaffolds alone were used as blank.

4.4. Influence of hydroxyapatite on hybrid scaffold

4.4.1. Synthesis process

To obtain a biomineralized scaffold for bone regeneration, two different strategies were exploited to create three different materials: mineralized CNF with a different ratio of CNF/HA in order to evaluate if CNF behavior is similar to Collagen and, if CNF/HA do not have a 3D architecture, it was introduced in gelatin solution to create a 3D hybrid composite.

Synthesis of CNF/MgHA with a 20/80 ratio

An acid suspension was prepared dissolving 27.5 g of CNF hydrogel (1.1 wt%) into acid phosphate solution (0.69 g of H_3PO_4 in 143 mL of H_2O). A basic suspension was prepared suspending 0.77 g of $Ca(OH)_2$ into 142 mL of H_2O and after adding 0.1 g of $MgCl_2$. Acid suspension was added dropwise into basic suspension at room temperature under gentle manual shaking through a glass stick in order to induce a biomineralization process of magnesium-doped hydroxyapatite (MgHA) nanoparticles on cellulose nanofibrils. The mineralization of CNF is immediately visible and the precipitate was let at room temperature for 2 hours to allow the growth of HA nano-crystals into CNF fibers. CNF/MgHA hybrid composite was washed three times through a centrifuge and a suspension of 4 wt% CNF/MgHA in water is prepared and distributed in Teflon moulds in order to obtain homogeneous porous structures with ordered pores and to pull out easy the material. Hybrid composite was freeze-dried with a controlled freeze-drying cycle setting the precise cooling temperature (−40 °C) and heating ramp (2 °C min^{-1} up to −5 and 1 °C min^{-1} up to 25 °C) at p = 0.086 mbar to achieve dried product. Finally, the DHT cross-linking was used after freeze-drying process, treating the samples in oven at 160°C and vacuum (P=0.001 mbar) for 48h. (Figure 4.19)

Synthesis of CNF/MgHA with a 60/40 ratio

An acid suspension was prepared dissolving 165 g of CNF hydrogel (1.1 wt%) into acid phosphate solution (0.69 g of H_3PO_4 in 143 mL of H_2O). A basic suspension was prepared suspending 0.77 g of $Ca(OH)_2$ into 142 mL of H_2O and after adding 0.1 g of $MgCl_2$. Acid suspension was added dropwise into basic suspension at room temperature under gentle manual shaking through a glass stick in order to induce a biomineralization process of magnesium-doped hydroxyapatite (MgHA) nanoparticles on cellulose nanofibrils. The mineralization of CNF is immediately visible and the precipitate was let at room temperature for 2 hours to allow the growth of HA nano-crystals into CNF fibers. CNF/MgHA hybrid composite was washed three times through a centrifuge and a suspension of 4 wt% CNF/MgHA in water is prepared and distributed in Teflon moulds in order to obtain homogeneous porous structures with ordered pores and to pull out easy the material. Hybrid composite was freeze-dried with a controlled freeze-drying cycle setting the precise cooling temperature (−40 °C) and heating ramp (2 °C min^{-1} up to −5 and 1 °C min^{-1} up to 25 °C) at p = 0.086 mbar to achieve dried product. Finally, the DHT cross-linking was used after freeze-drying process, treating the samples in oven at 160°C and vacuum (P=0.001 mbar) for 48h. (Figure 4.19)

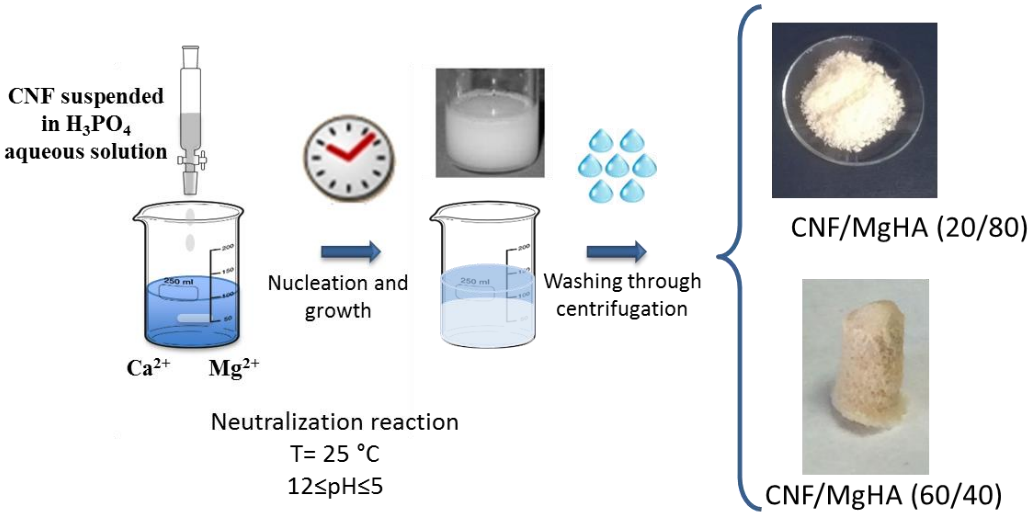

Figure 4.19. Schematic view of set-up for CNF/MgHA hybrid composites with a CNF/MgHA ratio of 20/80 and 60/40.

Synthesis of CNF/MgHA@Gel

An acid suspension was prepared dissolving 27.5 g of CNF hydrogel (1.1 wt%) into acid phosphate solution (0.69 g of H_3PO_4 in 143 mL of H_2O). A basic suspension was prepared suspending 0.77 g of $Ca(OH)_2$ into 142 mL of H_2O and after adding 0.1 g of $MgCl_2$. Acid suspension was added dropwise into basic suspension at room temperature under gentle manual shaking through a glass stick in order to induce a biomineralization process of magnesium-doped hydroxyapatite (MgHA) nanoparticles on cellulose nanofibrils. The mineralization of CNF is immediately visible and the precipitate was let at room temperature for 2 hours to allow the growth of HA nano-crystals into CNF fibers. CNF/MgHA hybrid composite was washed three times through a centrifuge it was freeze-dried with a controlled freeze-drying cycle setting the precise cooling temperature (−40 °C) and heating ramp (2 °C min^{-1} up to −5 and 1 °C min^{-1} up to 25 °C) at p = 0.086 mbar to achieve dried product. A 5 wt% CNF/MgHA suspension was prepared (1.25 g in 25 mL of H_2O) using ultrasound bath and vortex and a 3 wt% gelatin solution was prepared dissolving gelatin into water heated at 45 °C (0.75 g in 25 mL of H_2O) under magnetic stirring. Finally, CNF/MgHA suspension was poured into gelatin solution creating a 4 wt% blend in water and it was distributed in Teflon moulds in order to obtain homogeneous porous structures with ordered pores and to pull out easy the material. Hybrid composite was freeze-dried with a controlled freeze-drying cycle setting the precise cooling temperature (−40 °C) and heating ramp (2 °C min^{-1} up to −5 and 1 °C

min^{-1} up to 25 °C) at p = 0.086 mbar to achieve dried product. Finally, the DHT cross-linking was used after freeze-drying process, treating the samples in oven at 160°C and vacuum (P=0.001 mbar) for 48h. (Figure 4.20)

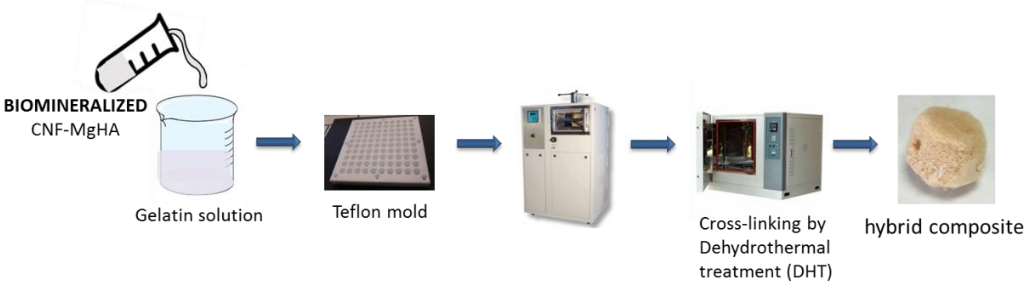

Figure 4.20. Schematic view of set-up for CNF/MgHA@Gel hybrid composite.

4.4.2. Results & Discussion

In the previous studies we demonstrated that CNF has an effective role as nano-reinforcement for gel based scaffolds and how different CNF:Gel ratio changes the mechanical properties of scaffolds. In this work, we want to evaluate how happen when the mineral phase was introduced in polymeric blend. At the beginning of experiment, different mineralization strategies were chosen such as the mineralization of CNF with two different CNF/MgHA ratio and the introduction of CNF/MgHA composite into a gel solution to obtain a hybrid composite. In particular, three different samples were synthetized: CNF/MgHA80 and CNF/MgHA40 where only the CNF/MgHA ratio changes from 80% to 40% of mineral phase and a hybrid composite (CNF/MgHA@Gel) where CNF/MgHA80 was introduced in a gel solution.

First of all, XRD, TGA and ICP analysis were carried out to confirm the presence of hydroxyapatite (HA) as mineral phase. XRD spectra revealed the presence of a very low crystalline phase typical of HA synthetized in presence of an organic phase through a biomineralization process (Figure 4.21A).[43,44] TGA confirmed the different organic/MgHA ratio, CNF/MgHA80 shows the highest amount of HA (78wt%) while CNF/MgHA@Gel and CNF/MgHA40 shows a lower amount of HA of 48 wt% and 38 wt% respectively, reason why only in these samples the final shape is a 3D architecture (Figure 4.19B). In addition, ICP revealed a Ca/P ratio below 1.60 typical of a biomimetic hydroxyapatite doped with magnesium typical ions in young bone which promotes the bioavailability reducing the crystallinity of HA (Table 4.7). In conclusion, chemical analyses revealed the formation of a quasi-amorphous hydroxyapatite typical of nature hard tissue and biomimetic scaffolds for tissue regeneration.[45]

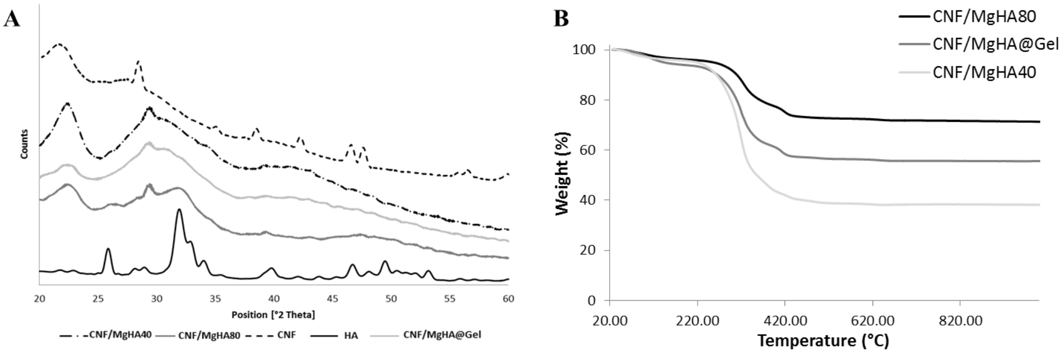

Figure 4.21. (A) XRD spectra of CNF/MgHA80, CNF/MgHA40 and CNF/MgHA@Gel compared with pure HA and CNF; (B) TGA spectra of CNF/MgHA80, CNF/MgHA40 and CNF/MgHA@Gel.

Table 4.7. ICP analysis of CNF/MgHA80, CNF/MgHA40 and CNF/MgHA@Gel hybrid composites.

Samples	**Ca/P**	**Mg/Ca**	**(Ca+Mg)/P**
CNF/MgHA40	2,29 ± 0,16	0,06 ± 0,001	2,44 ± 0,17
CNF/MgHA80	1,78 ± 0,07	0,07 ± 0,001	1,91 ± 0,08
CNF/MgHA@Gel	1,93 ± 0,04	0,06 ± 0,001	2,07 ± 0,05

As shown in figure 4.22, not all samples have a 3D stable architecture, in particular, CNF/MgHA80 synthesis determines the formation of a particulate and the CNF/MgHA40 a highly brittle scaffold not stable in wet conditions. However, in all samples SEM images showed a rough surface of fibers where mineral phase covered completely CNF fibers as figure 4.20A shows. In particular, CNF/MgHA80 showed flakes of 50-100 µm where mineral phase is clearly visible on the surface, however no 3D porous structure is achieved in the final materials. This happen when the mineral phase is too high and all functional groups of CNF interacts with HA, avoiding the self-assembling of fibers and, thus, the achievement of a 3D stable architecture. Anyway, by blending CNF/MgHA80 with Gel solution a 3D structure was obtained. As is visible from SEM images (CNF/MgHA@Gel in Fig. 4.20) its characterized of interconnected porosity and mineralized CNF particles are homogeneously distributed and well-adhered to Gel matrix, responsible for confer stability to the 3D structure[28]. As mentioned above, CNF/HA40 produced a 3D scaffold due to the low amount of mineral phase, so some functional groups remain available to interact between them and to develop a 3D architecture, however, due to the low amount of functional groups in CNF, in comparison to Collagen, the self-assembling of CNF cannot create a robust dried scaffold.[46]

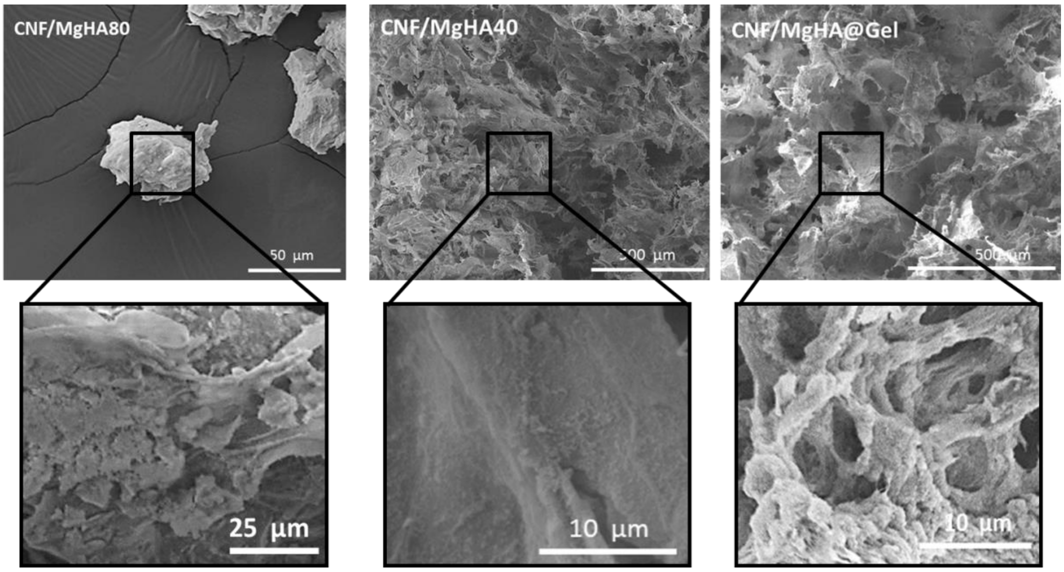

Figure 4.22. SEM images of CNF/MgHA80; CNF/MgHA40; CNF/MgHA@Gel at low magnification. Insets reveal detail on the composites' surface at high magnification.

Porosity and stability tests were carried out to well-characterized hybrid composites. Both CNF/MgHA40 and CNF/MgHA@Gel displayed high porosity more than 95% evaluated by density method and more than 70% evaluated by water squeezing method. First method measures the overall porosity composed of nano- and micro-porosity, while the second method measures only the macro-porosity suitable for cell colonization and proliferation and nutrients migration inside scaffold (table 4.8).[25,47] Furthermore, a stability test was carried out on the scaffolds CNF/MgHA40 and CNF/MgHA@Gel submerging scaffolds in PBS at 37°C and evaluating the degradation rate and swelling ratio. These are important data because a porous scaffold for tissue regeneration must be biodegradable, but the modulation of degradation time is essential because a too fast degradation doesn't allow cells to regenerate the damaged tissue. The degradation of the scaffold, indeed, should occur at the same time with the formation of new tissue. After 28 days the scaffolds with lower amount of HA (CNF/MgHA40) revealed a high degree of degradation, while CNF/MgHA@Gel revealed a lower degradation. However, after three months both scaffolds have lost their macroscopic shape revealing their suitability as scaffolds for fast bone regeneration processes.[48]

Table 4.8. Summary of porosity and stability parameters of CNF/MgHA40 and CNF/MgHA@Gel.

Samples	Porosity		Degradation	
	Density method	Water squeezing method	After 28 days	After 3 months
CNF/MgHA40	98,27 ± 0,24	89,08± 1,84	50,2 ± 0,3	Instable
CNF/MgHA@Gel	95,21 ± 0,46	71,75 ± 1,72	18,6 ± 4,8	instable

The swelling ratio was carried out to evaluate the scaffold capacity to absorb water and, subsequently, cell medium that is essential for cells migration inside scaffold and cells proliferation (Figure 4.23). It shows that samples porosity allows to absorb huge amounts of water, about 10-20 times the weight of dried sample, nevertheless, the swelling of CNF/MgHA40 is double than CNF/MgHA@Gel, probably meanings that CNF/MgHA40 has more polar functional groups affecting the hydrophilicity and, thus, swelling ratio. Furthermore, the swelling is fast and does not change during the time, meaning no initial degradation and no loss of structure.

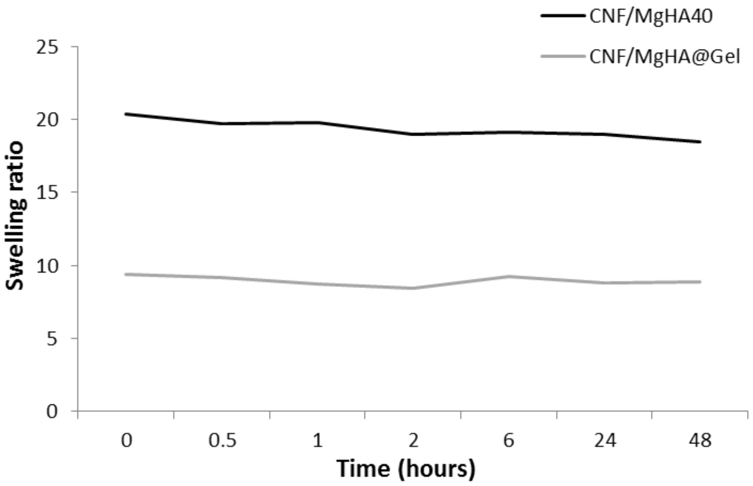

Figure 4.23. a) swelling behavior in wet conditions in PBS at 37°C of CNF/MgHA40 and CNF/MgHA@Gel.

4.5. Conclusion

In the present work, polymeric nanocomposites were designed for the obtainment of Gel-based 3D porous scaffolds with improved performances making them suitable for tissue regeneration. The approach selected to enhance the mechanical response of the gelatin matrix consists in the addition of cellulose nanofibrils by a blending process and the treatment with different cross-linking methods. As result, we were able to achieve reinforced nanocomposite scaffolds with an isotropic porous structure with tailored degradation kinetics and the mechanical test reveals an improvement of the Young’s modulus and a preservation of Gel elastic properties. Moreover, preliminary in vitro evaluations demonstrate that developed scaffolds are able to promote and support cell adhesion and proliferation.

The evaluation of blends with different CNF:Gel ratio demonstrates the blend powerful able to improve the single polymer properties. In particular, polymeric blend reveals some different characteristics in comparison to pure polymers. This is a proof of the blend concept.

Furthermore, all blends are capable to promote and support the cell colonization and proliferation confirming that blending different polymeric matrices it is possible to engineer new nano-composite materials with improved properties respect to the original raw materials. Finally, the biomineralization process occurred successfully, but only CNF/MgHA40 and CNF/MgHA@Gel maintained a 3D dried structure after freeze-drying. All the analysis demonstrates the obtaining of a hybrid material reproducing the chemical features of bone highlighted from a high Ca/P ratio typical of not stoichiometric HA and a poorly crystalline MgHA phase. Anyway, the final shape is not a robust scaffold yet.

REFERENCES

1. Tampieri, A., Sprio, S., Sandri, M. & Valentini, F. Mimicking natural bio-mineralization processes: A new tool for osteochondral scaffold development. *Trends Biotechnol.* **29**, 526–535 (2011).

2. Sprio, S. *et al.* Bio-inspired assembling/mineralization process as a flexible approach to develop new smart scaffolds for the regeneration of complex anatomical regions. *J. Eur. Ceram. Soc.* **36**, 2857–2867 (2016).

3. Serra, I. R. *et al.* Production and characterization of chitosan/gelatin/β-TCP scaffolds for improved bone tissue regeneration. *Mater. Sci. Eng. C* **55**, 592–604 (2015).

4. Uchida, N. *et al.* Nanometer-sized extracellular matrix coating on polymer-based scaffold for tissue engineering applications. *J. Biomed. Mater. Res. Part A* **104**, 94–103 (2015).

5. Campodoni, E. *et al.* Polymeric 3D scaffolds for tissue regeneration: Evaluation of biopolymer nanocomposite reinforced with cellulose nanofibrils. *Mater. Sci. Eng. C* **94**, 867–878 (2019).

6. Shankar, K. G. *et al.* Investigation of different cross-linking approaches on 3D gelatin scaffolds for tissue engineering application: A comparative analysis. *Int. J. Biol. Macromol.* **95**, 1199–1209 (2017).

7. Boanini, E., Rubini, K., Panzavolta, S. & Bigi, A. Chemico-physical characterization of gelatin films modified with oxidized alginate. *Acta Biomater.* **6**, 383–388 (2010).

8. Yue, K. *et al.* Synthesis, properties, and biomedical applications of gelatin methacryloyl (GelMA) hydrogels. *Biomaterials* **73**, 254–271 (2015).

9. Mondragon, G., Peña-Rodriguez, C., González, A., Eceiza, A. & Arbelaiz, A. Bionanocomposites based on gelatin matrix and nanocellulose. *Eur. Polym. J.* **62**, 1–9 (2015).

10. Eichhorn, S. J. *et al.* *Review: Current international research into cellulose*

nanofibres and nanocomposites. *Journal of Materials Science* **45**, (2010).

11. Saito, T., Nishiyama, Y., Putaux, J., Vignon, M. & Isogai, A. Homogeneous Suspensions of Individualized Microfibrils from.pdf. **7**, 3–7 (2006).

12. Rashad, A., Mustafa, K., Heggset, E. B. & Syverud, K. Cytocompatibility of Wood-Derived Cellulose Nanofibril Hydrogels with Different Surface Chemistry. *Biomacromolecules* **18**, 1238–1248 (2017).

13. Ratanavaraporn, J., Rangkupan, R., Jeeratawatchai, H., Kanokpanont, S. & Damrongsakkul, S. Influences of physical and chemical crosslinking techniques on electrospun type A and B gelatin fiber mats. *Int. J. Biol. Macromol.* **47**, 431–438 (2010).

14. Madaghiele, M. *et al.* Assessment of collagen crosslinking and denaturation for the design of regenerative scaffolds. *J. Biomed. Mater. Res. - Part A* **104**, 186–194 (2016).

15. Syverud, K., Pettersen, S. R., Draget, K. & Chinga-Carrasco, G. Controlling the elastic modulus of cellulose nanofibril hydrogels---scaffolds with potential in tissue engineering. *Cellulose* **22**, 473–481 (2015).

16. Bi, L. *et al.* Effects of different cross-linking conditions on the properties of genipin-cross-linked chitosan/collagen scaffolds for cartilage tissue engineering. *J. Mater. Sci. Mater. Med.* **22**, 51–62 (2011).

17. Marcacci, M. *et al.* Arthroscopic second generation autologous chondrocyte implantation. *Knee Surgery, Sport. Traumatol. Arthrosc.* **15**, 610–619 (2007).

18. Marcacci, M. *et al.* Unicompartmental osteoarthritis: an integrated biomechanical and biological approach as alternative to metal resurfacing. *Knee Surgery, Sport. Traumatol. Arthrosc.* **21**, 2509–2517 (2013).

19. Behrens, P., Bitter, T., Kurz, B. & Russlies, M. Matrix-associated autologous chondrocyte transplantation/implantation (MACT/MACI)—5-year follow-up. *Knee* **13**, 194–202 (2006).

20. Dash, R., Foston, M. & Ragauskas, A. J. Improving the mechanical and thermal

properties of gelatin hydrogels cross-linked by cellulose nanowhiskers. *Carbohydr. Polym.* **91**, 638–645 (2013).

21. Tillet, G., Boutevin, B. & Ameduri, B. Chemical reactions of polymer crosslinking and post-crosslinking at room and medium temperature. *Prog. Polym. Sci.* **36**, 191–217 (2011).

22. Syverud, K. Tissue Engineering Using Plant-Derived Cellulose Nanofibrils (CNF) as Scaffold Material. in *Nanocelluloses: Their Preparation, Properties, and Applications* **1251**, 171-189 SE–9 (American Chemical Society, 2017).

23. Syverud, K., Kirsebom, H., Hajizadeh, S. & Chinga-Carrasco, G. Cross-linking cellulose nanofibrils for potential elastic cryo-structured gels. *Nanoscale Res. Lett.* **6**, 626 (2011).

24. Ishii, D., Saito, T. & Isogai, A. Viscoelastic evaluation of average length of cellulose nanofibers prepared by tempo-mediated oxidation. *Biomacromolecules* **12**, 548–550 (2011).

25. Arora, A., Kothari, A. & Katti, D. S. Pore orientation mediated control of mechanical behavior of scaffolds and its application in cartilage-mimetic scaffold design. *J. Mech. Behav. Biomed. Mater.* **51**, 169–183 (2015).

26. Landi, E., Valentini, F. & Tampieri, A. Porous hydroxyapatite/gelatine scaffolds with ice-designed channel-like porosity for biomedical applications. *Acta Biomater.* **4**, 1620–1626 (2008).

27. Nieto-Suárez, M., López-Quintela, M. A. & Lazzari, M. Preparation and characterization of crosslinked chitosan/gelatin scaffolds by ice segregation induced self-assembly. *Carbohydr. Polym.* **141**, 175–183 (2016).

28. Panseri, S. *et al.* Biomimetic Scaffold with Aligned Microporosity Designed for Dentin Regeneration. *Front. Bioeng. Biotechnol.* **4**, 48 (2016).

29. Krishnakumar, G. S. *et al.* Evaluation of different crosslinking agents on hybrid biomimetic collagen-hydroxyapatite composites for regenerative medicine. *Int. J. Biol. Macromol.* **106**, 739–748 (2018).

30. Yan, L. P. *et al.* Macro/microporous silk fibroin scaffolds with potential for articular cartilage and meniscus tissue engineering applications. *Acta Biomater.* **8**, 289–301 (2012).

31. Yan, L. P. *et al.* Genipin-cross-linked collagen/chitosan biomimetic scaffolds for articular cartilage tissue engineering applications. *J. Biomed. Mater. Res. - Part A* **95 A**, 465–475 (2010).

32. Huang, Y., Onyeri, S., Siewe, M., Moshfeghian, A. & Madihally, S. V. In vitro characterization of chitosan-gelatin scaffolds for tissue engineering. *Biomaterials* **26**, 7616–7627 (2005).

33. Hua, K. *et al.* Transition from Bioinert to Bioactive Material by Tailoring the Biological Cell Response to Carboxylated Nanocellulose. *Biomacromolecules* **17**, 1224–1233 (2016).

34. Alexandrescu, L., Syverud, K., Gatti, A. & Chinga Carrasco, G. *Cytotoxicity tests of cellulose nanofibril-based structures*. *Cellulose* **20**, (2013).

35. Yeom, J. *et al.* Effect of Cross-Linking Reagents for Hyaluronic Acid Hydrogel Dermal Fillers on Tissue Augmentation and Regeneration. *Bioconjug. Chem.* **21**, 240–247 (2010).

36. Pandit, V. *et al.* Evaluation of Multifunctional Polysaccharide Hydrogels with Varying Stiffness for Bone Tissue Engineering. *Tissue Eng. Part A* **19**, 2452–2463 (2013).

37. Bott, K. *et al.* The effect of matrix characteristics on fibroblast proliferation in 3D gels. *Biomaterials* **31**, 8454–8464 (2010).

38. Pulieri, E. *et al.* Chitosan/gelatin blends for biomedical applications. *J. Biomed. Mater. Res. - Part A* **86**, 311–322 (2008).

39. Ratanavaraporn, J., Damrongsakkul, S., Sanchavanakit, N., Banaprasert, T. & Kanokpanont, S. Comparison of Gelatin and Collagen Scaffolds for Fibroblast Cell Culture. *J. Met. Mater. Miner.* **16**, 31–36 (2006).

40. Jiang, Y. *et al.* Preparation of Cellulose Nanofiber-reinforced Gelatin Hydrogel

and Optimization for 3D Printing Applications. *Bioresour. Vol 13, No 3* (2018).

41. Mohammadi, R. *et al.* Physico-mechanical and structural properties of eggshell membrane gelatin- chitosan blend edible films. *Int. J. Biol. Macromol.* **107**, 406–412 (2018).

42. Cigognini, D. *et al.* Engineering in vitro microenvironments for cell based therapies and drug discovery. *Drug Discov. Today* **18**, 1099–1108 (2013).

43. Krishnakumar, G. S. *et al.* Ribose mediated crosslinking of collagen-hydroxyapatite hybrid scaffolds for bone tissue regeneration using biomimetic strategies. *Mater. Sci. Eng. C* **77**, 594–605 (2017).

44. Tampieri, A. *et al.* Biologically inspired synthesis of bone-like composite: Self-assembled collagen fibers/hydroxyapatite nanocrystals. *J. Biomed. Mater. Res. - Part A* **67**, 618–625 (2003).

45. Sprio, S. *et al.* Biomimesis and biomorphic transformations: New concepts applied to bone regeneration. *J. Biotechnol.* **156**, 347–355 (2010).

46. Tampieri, A. *et al.* HA/alginate hybrid composites prepared through bio-inspired nucleation. *Acta Biomater.* **1**, 343–351 (2005).

47. Mao, J. S., Zhao, L. G., Yin, Y. J. & Yao, K. De. Structure and properties of bilayer chitosan-gelatin scaffolds. *Biomaterials* **24**, 1067–1074 (2003).

48. Nicoletti, A. *et al.* Effects of different crosslinking conditions on the chemical-physical properties of a novel bio-inspired composite scaffold stabilised with 1,4-butanediol diglycidyl ether (BDDGE). *J. Mater. Sci. Mater. Med.* **24**, 17–35 (2013).

5. Superparamagnetic hybrid nanoparticles as drug delivery system

5.1. Introduction

Magnetic nanomaterials have the potential as smart switching agent to be incorporated in carriers of biomolecules for nanomedical applications and can be remotely activated through alternate magnetic fields. Indeed, superparamagnetic iron oxides nanoparticles (SPIONS) are the most frequently used magnetic NPs in nanomedicine, and they were also used for the synthesis of magnetic hybrid nanobeads (MHNs) due to their high magnetization[1,2]. However, harmful side effects related to long-term accumulation in the human body pose serious concerns to their use and push material scientists to develop new biocompatible magnetic media.[3,4] In this respect the recently developed biocompatible, bioresorbable, superparamagnetic Fe-HA nano-phase represents a unique tool associating intense responsiveness to magnetic fields and adequate bio-safety so to represent a possible breakthrough in the current scenario of nanoparticles used in medicine.[5] This new phase exhibits high magnetization when exposed to the effect of electromagnetic fields, in spite of low amounts of secondary iron oxides, so that it can exhibit excellent biocompatibility and bioresorbability.[6] A recent approach consists in the synthesis of hybrid devices where functional inorganic phases are dispersed into organic matrices.[7] The physico-chemical properties of bio-polymers and biocompatible inorganic nano-phases such as hydroxyapatite (HA:$Ca_{10}(PO_4)_6(OH)_2$) can be combined to exploit the high densities of active surface sites in both components for the linking of bioactive molecules, and to design their release profile, thus enabling smart and flexible applications.[8–10] In this respect synthetic polymers exhibiting excellent biocompatibility and biodegradability. Among these, Alginate (Alg), a natural polysaccharide extracted by brown algae is largely used for the fabrication of biomaterials and nanobeads thank to its biodegradability, biocompatibility and low production costs.[11] Calcium is the most frequently used divalent ions for Alg gelation, as it forms an ideal matrix for developing stable hydrogels[12], thanks to its ability to link its constituting mannuronic and guluronic units, thus assuming a typical structure called ‘egg-box’.[13] Moreover, thanks to its ability to link Ca^{2+} ions, Alg is a good candidate for heterogeneous nucleation of calcium phosphates, particularly HA, so that hybrid Alg/HA biomaterials can be easily developed.[14] In the present chapter, magnetic hybrid nanobeads (MHNs) were produced using Alg as bio-polymeric matrix that acted as a template for the heterogeneous nucleation of FeHA nanoparticles. The resulted composite was then engineered into magnetic hybrid nanobeads by oil-in-water emulsion technique[15–17], and stabilized by cross-linking with Ca^{2+} ions. The obtained MHNs are intended for use as drug delivery system.

5.2. Synthesis process

Synthesis of Iron-Substituted Hydroxyapatite (FeHA NPs). FeHA NPs were synthesized through neutralization process.[5] An acid aqueous solution of H_3PO_4 was prepared dissolving 20.75 g in 300 mL of H_2O. Three different basic suspension was prepared in the following way: i) 23.4 g of $Ca(OH)_2$ was suspended in 400 mL of H_2O; ii) 6.03 g of $FeCl_2 \cdot 4H_2O$ was dissolved in 75 mL of H_2O; iii) 8.28 g of $FeCl_3 \cdot 6H_2O$ was dissolved in 75 mL of H_2O. Calcium suspension was heated in a heating mantle set at 45 °C under mechanical stirring and the temperature was controlled by means of a thermometer placed in the reacting solution. After 30 minutes, $Fe^{2/3+}$ solutions were added at calcium suspension, afterwards, acid suspension was added dropwise into the basic suspension maintaining temperature at 40 °C under constant stirring. Afterwards, the reaction product was left to age at 40 °C under constant stirring for 1 hour and then for 24 hours at room temperature. The solid was separated from the mother liquor by centrifugation, washed three times with water, freeze-dried, and finally sieved at 150 μm.

Synthesis of hybrid composite (AlgFeHA). Heterogeneous nucleation of FeHA nanocrystals on assembling Alg matrix was achieved by means of neutralization reaction performed as follows. An acid solution of H_3PO_4 (0.88 g in 200 mL) at 40 °C was dropped into a basic aqueous suspension of $Ca(OH)_2$ (1 g in 200 mL) containing $FeCl_2 \cdot 4H_2O$ (0.258 g in 4 mL) and $FeCl_3 \cdot 6H_2O$ (0.351 g in 4 mL) kept at the constant temperature of 40 °C. Immediately after the addition of H_3PO_4 a gelatinous aqueous solution of sodium alginate (1.28 g in 200 mL) was dropped under constant magnetic stirring. The composite was left to age without stirring for 2 hrs, then collected by centrifugation, washed three times with distilled water and, finally, freeze-dried.

Synthesis of magnetic hybrid nanobeads (MHNs) by oil-in-water emulsion process. MHNs were prepared by using oil-in-water emulsion technique. An aqueous suspension of AlgFeHA hybrid composite (0.275 g in 60 mL) was prepared and subjected to sonication (tip sonicator ultrasonic processor XL 2020) to disperse and homogenize AlgFeHA agglomerates. 0.333 g of sodium alginate were added to the obtained suspension together with dichloromethane (CH_2Cl_2) in oil/water ratio of 1/10. Then, the biphasic dispersion was sonicated in an ice bath for 5 min and the obtained emulsion was stabilized by cross-linking adding 39 mL of 0.36 mM $CaCl_2$ aqueous solution under mechanic and constant stirring at 20 °C. The suspension was ripened at 20 °C overnight under stirring to homogenize the nanobeads and to remove the CH_2Cl_2 by evaporation. Finally, the product was washed by centrifugation with deionized water and dried in oven at 40 °C for 48 h before analysis (Figure 5.1).

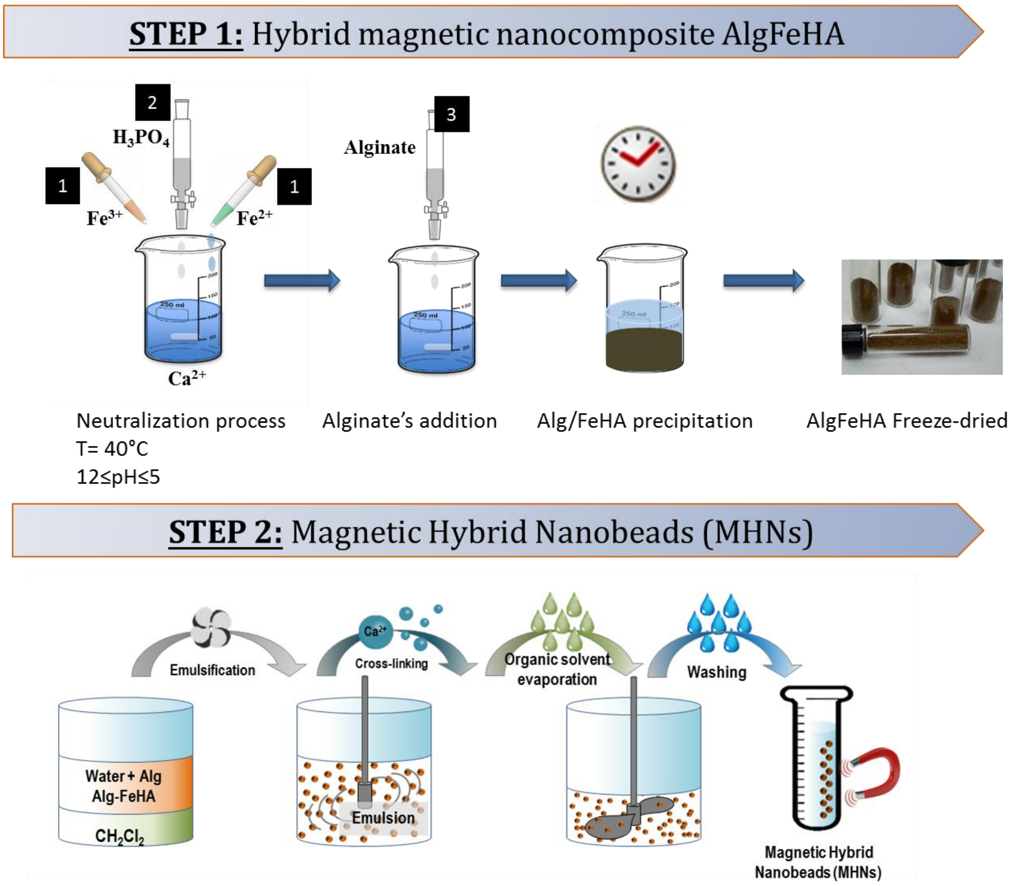

Figure 5.1. Schematic representation of experimental setup to produce MHNs through *oil-in-water* technique.

5.3. Results&Discussion

FeHA NPs were synthesized according to the method reported by Tampieri et al.[5] to obtain a reference material to be compared with the AlgFeHA hybrid composite investigating the effects of Alg matrix on the mineralized iron-doped phase. A bio-inspired mineralization approach was followed to synthesize an AlgFeHA superparamagnetic hybrid composite consisting of Fe-doped apatite nanocrystals nucleated onto alginate polymeric matrices. During the mineralization reaction the chemical and spatial constraints imposed by the organic template led to the formation of a biomimetic mineral phase with very low crystal ordering. These features provide enhanced mimicry of bone tissue.[18]

XRD analysis was carried on AlgFeHA in comparison with FeHA NPs, stoichiometric HA and magnetite as figure 5.2A shows. The pattern highlighted the formation of apatitic phase (JCPDS-PDF 740565) with the characteristic peaks at 26° and 32°, while peaks ascribable to any iron oxide secondary phase (e.g. magnetite or maghemite) were not detected. As demonstrated by the poorly resolved peaks, the iron-doped apatite crystals nucleated on the Alg is characterized by very low crystallinity degree, which is typical of HA grown on organic templates meaning that the biomineralization process meaning successfully.[14,19] Furthermore, also FTIR spectrum of AlgFeHA (Figure 5.2B) shows peaks at 3404, 1612, 1424, 1036, 557 cm^{-1}. The peak at 3404 cm^{-1} corresponds to the stretching vibrations of O-H bonds of both FeHA and Alg, while the peaks at 1612 and 1425 cm^{-1}, recorded only for pure alginate and AlgFeHA, are related to the asymmetric and symmetric stretching vibrations of the carboxylate groups in Alg. The signal at 1036 cm^{-1} corresponds to the asymmetric stretching of PO_4 groups of FeHA and to the C-O-C stretching vibration, particularly of pyranosyl ring in M residues of the Alg. Finally, the peak at 557 cm^{-1} is related to the bending of the PO_4 group of the FeHA.[19,20]

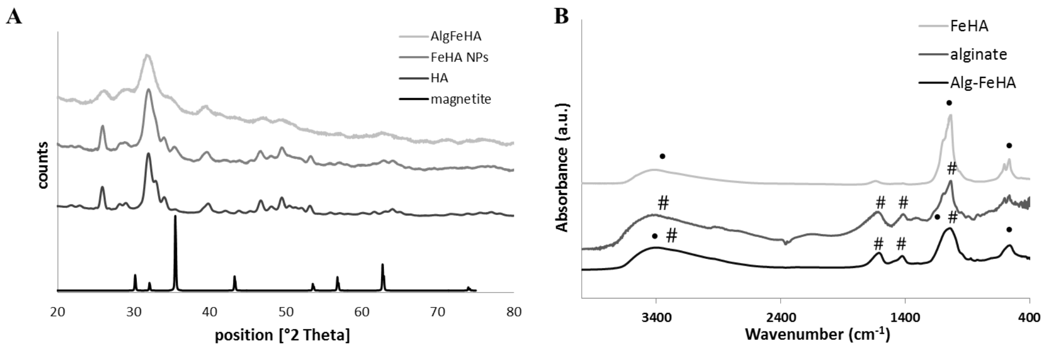

Figure 5.2. A) XRD patterns of AlgFeHA hybrid composite, FeHA NPs, and reference magnetite and poorly crystalline HA; B) FTIR spectra of AlgFeHA hybrid composite, Alg and FeHA NPs, the peaks marking with # correspond to the organic phase (Alg), while those marked with · correspond to the apatitic phase.

The hybrid composite obtained by the bio-inspired nucleation process (AlgFeHA) appears as flakes on which the mineral phase is uniformly distributed (Figure 5.3). TEM pictures of FeHA NPs and AlgFeHA (Figure 5.3) highlighted the effects of Alg matrix on iron-doped apatite crystal growth. The pictures show that FeHA NPs display rod-like morphology and are rather heterogeneous in size with a major axis around 150 nm and a small minor axis in the 10-20 nm range, while the mineral phase of the AlgFeHA hybrid composite consists of crystallites of 20 nm surrounded by an amorphous film of Alg. Of note is the absence of any iron oxide secondary phase inside AlgFeHA hybrid composite (Figure 5.3C), that instead was detected for FeHA NPs (Figure 5.3A) as small (<20 nm) and black round-shaped NPs also confirmed from XRD analyses. The high heterogeneity of FeHA NPs can be ascribed to the great amount of foreign ions (i.e. Fe^{2+}, Fe^{3+}, CO_3^{2-}) causing crystal lattice distortion, reduction of the long-range periodic regularity, and possible modifications of surface energy.[21]

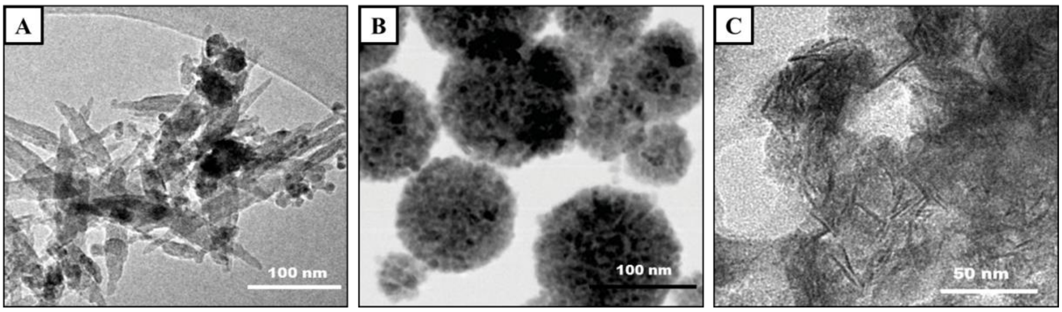

Figure 5.3. TEM images of A) FeHA NPs; B) commercial iron oxides (SPIONs); C) AlgFeHA hybrid composite.

Summarizing the whole analysis conducted on AlgFeHA, it is possible to state that biomineralization process occurs successfully thank to organic matrix, alginate, which constrained the nucleation of apatitic phase. The effect of these constraints on the reduction of particle size and crystallinity is demonstrated by comparing AlgFeHA hybrid composite with FeHA NPs synthesized in absence of organic template. Even if TEM and XRD analysis did not show the presence of secondary phases beside FeHA, the occurrence of small quantities of iron oxides could not be excluded. During the oil-in-water emulsion, the interaction between the Alg molecules and the oil under sonication induces the 3D arrangement of the AlgFeHA hybrid composite into an egg-like form featuring uniform size distribution – and exposure of iron-doped apatitic phase at the nanobeads surface. The amount of $CaCl_2$ needed for effective cross-linking process should be optimized to find the suitable amount of cross-linking capable to stabilize nanobeads formed without promoting their aggregation. The ratio between $CaCl_2$ and Alg was varied in the range 0.003-0.37 wt% and the suitable cross-linking degree was selected by measuring the hydrodynamic diameter and the polydispersity index obtained by dynamic light scattering (DLS) with a Zetasizer Nano ZS (Malvern Ltd., UK). As figure 5.4 shows, the evaluation of the average hydrodynamic diameter (H_d) revealed that when the $CaCl_2$:Alg ratio is lower than 0.07 the average hydrodynamic diameter and the polydispersity index determined by DLS are high, suggesting a poor cross-linking degree. Similarly, when the $CaCl_2$:Alg ratio exceeds the value of 0.37, the MHNs diameter and polydispersity index become too big, probably due to the nanobeads aggregation.[22] On this basis, the $CaCl_2$:Alg ratio selected for the fabrication of MHNs described in this work was 0.26, corresponding to the formations of nanobeads with the lower particle size and polydispersity index.

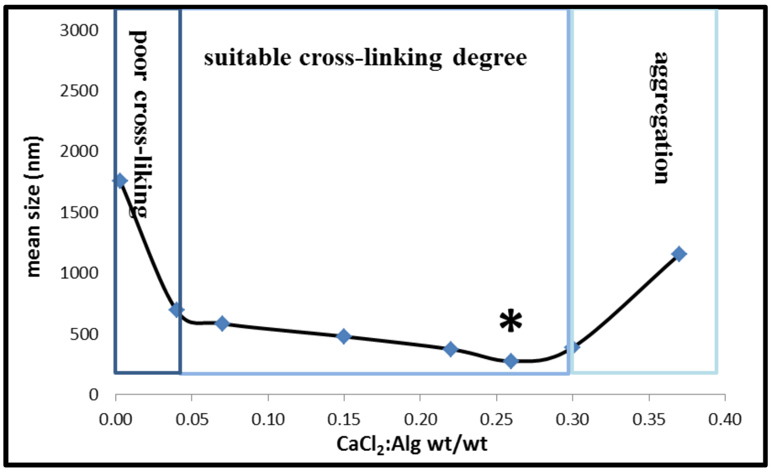

Figure 5.4. Effect of the $CaCl_2$ on Alg ratio on the stability of MHNs water suspension (pH = 7.8)

XRD and FTIR analyses were performed on MHNs to evaluate if the formation of nanobeads could interfere on the properties of HA. The XRD pattern and FTIR analysis of the MHNs (Figure 5.5) obtained by the oil in water technique was comparable to that recorded on the AlgFeHA hybrid composite, demonstrating that the procedure utilized to produce the nanobeads did not alter composition and crystallinity of the mineral phase.

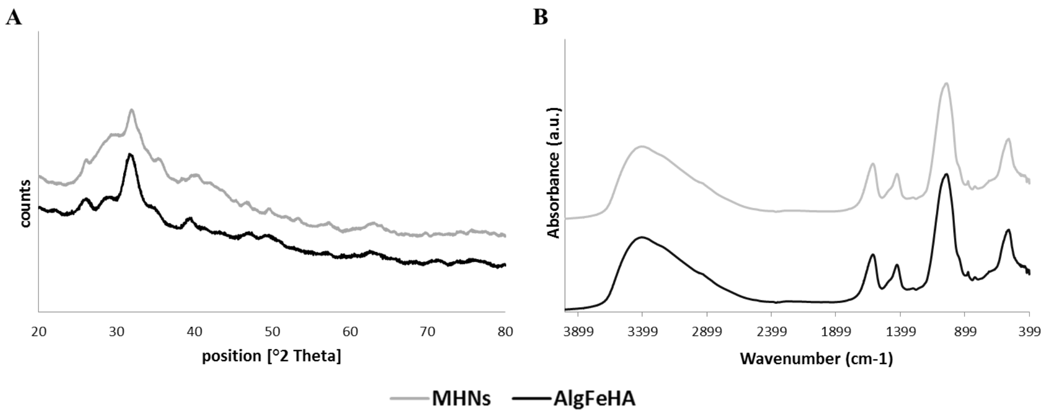

Figure 5.5. A) XRD patterns and B) FTIR spectra of magnetic hybrid nanobeads (MHNs) compared to AlgFeHA hybrid composite.

ICP analysis showed the chemical quantification of MHNs compared to FeHA NPs (Figure 5.6A). The (Ca+Fe)/P molar ratio of MHNs is higher with respect to FeHA NPs due to the strong interaction between Alg and Ca^{2+} and Fe^{3+} ions. As shown by a previous study, the iron(III)-alginate complex is more stable than the iron(III) or alginate alone[23]. Thus part of the quantified iron could be due to the formation of Fe-Alg complexes rather than to substitutional iron ions in the iron-doped HA lattice. Moreover, the Ca2+ ions used to cross-link the suspension after the emulsion process and forming the Ca-Alg complex contribute to increase the (Ca+Fe)/P and Ca/P molar ratios. However, that data showed that the Ca/P and Fe/Ca molar ratios of FeHA NPs and MHNs are quite similar, and are in agreement with that reported by Tampieri et al. for biomimetic FeHA NPs.[5] The degradation profiles registered by the thermogravimetric analysis of MHNs (Figure 5.6B) revealed a mineral content of about 68 wt%. In spite of the important role of the polymeric matrix, TGA analysis revealed a low amount of Alg (32%), and consequently a major amount of mineral phase. This aspect is very important in respect of the superparamagnetic ability detected on MHNs. Only mineral confers indeed to MHNs a superparamagnetic behavior, thus a higher density of magnetic inorganic phase can allow to obtain a material with a higher saturation magnetization value.

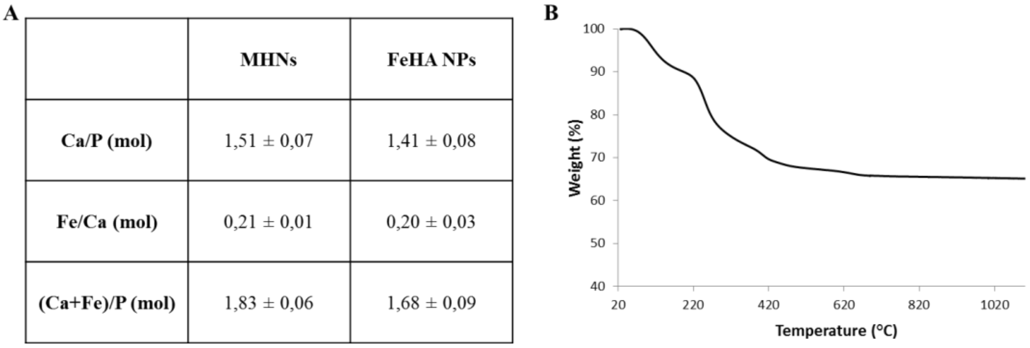

	MHNs	FeHA NPs
Ca/P (mol)	1,51 ± 0,07	1,41 ± 0,08
Fe/Ca (mol)	0,21 ± 0,01	0,20 ± 0,03
(Ca+Fe)/P (mol)	1,83 ± 0,06	1,68 ± 0,09

Figure 5.6. A) Chemical features measured by ICP of the MHNs in comparison with a biomimetic FeHA NPs reported in the literature [5]) TGA curve of MHNs.

TEM and SEM images (Figure 5.7) shows that the adopted oil-in-water emulsion process followed by cross-linking was suitable for the development of egg-like shaped nanometric particles exposing on the surface the FeHA NPs. The DLS analysis revealed an average hydrodynamic diameter for the MHNs of 203 ± 1 nm, in agreement with TEM analysis, with a low polydispersity index (Table 5.1), and a ζ-potential of the MHNs suspension (7.80 pH) similar to that of FeHA NPs (-21.0 ± 0.7 mV).[24] the superficial charge of MHNs, very close to that of biomimetic FeHA NPs confirmed the presence of iron doped mineral phase on the nanobeads surface. The presence of apatitic phase on the surface makes the MHNs suitable in drug delivery field because FeHA on the surface can highly protect drug inside the nanobeads and it can link with several bioactive molecules capable to target the system in the desired area.

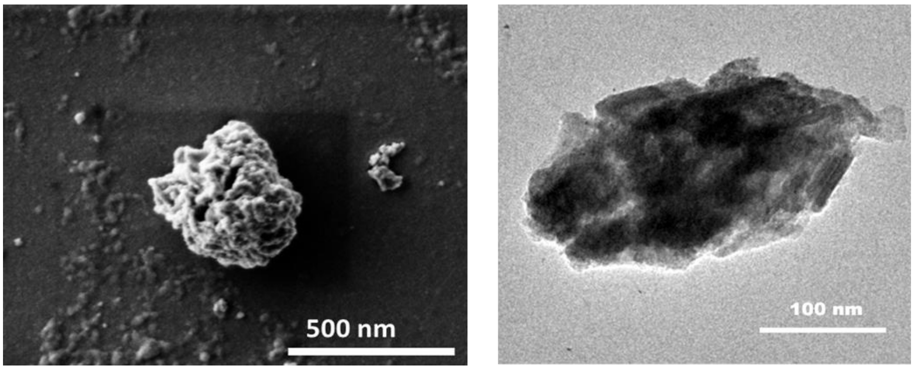

Figure 5.7. A) SEM images and B) TEM images of MHNs.

The magnetic hysteresis loop recorded at RT on MHNs reported in Figure 5.8 is that of a superparamagnetic material displaying a very low coercive field (coercitivity Hc = 5 Oe). The magnetization saturates readily in rather low fields (< 15 kOe), reaching a magnetization saturation (Ms) of 2.75 emu/g. Due to their superparamagnetic ability the new MHNs can be potentially used for smart applications in nanomedicine, in replacement of the currently used SPION, such as controlled, and on demand drug delivery in targeted tissues.[25–27]

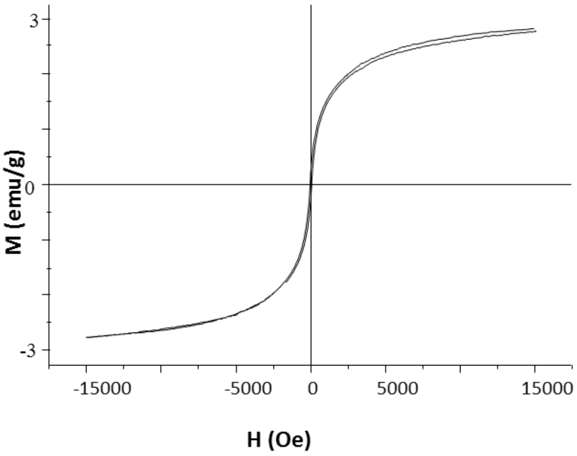

Figure 5.8. Magnetization versus magnetic field isotherm collected of MHNs collected at RT.

Stability tests performed at 37 °C upon variation of the pH range and the suspension medium (Tables 5.1 and 5.2) showed that MHNs are stable in physiological, acid and basic solutions up to the day 3. After 7 days the hydrodynamic diameter and polydispersity index of MHNs increased significantly, suggesting that after day 3 MHNs start to degrade and/or to agglomerate.[28] This is particularly evident when a basic medium was used evidenced by the large size and polydispersity index increase, but also for the significant error (±186.4) in strong contrast to the other. Furthermore, stability tests carried out at different temperatures show that MHNs can be preserved at low temperature (up to 4°C, at least) as aqueous suspensions without significant alterations up to seven days. The high stability of MHNs in different media and over a wide range of pH[20,28] and the absence of any remnant magnetization prevent aggregation phenomena which is a fundamental requirement to avoid the thrombi formation in the cardiovascular system. Besides, the good stability of MHNs is also important to avoid the their degradation before reaching the target site, and to prevent the uncontrolled release of the drug eventually loaded into them in undesired areas of the body.[29,30]

Table 5.1. Stability tests of MHNs depending on (A) different medium and (B,C) different pH.

Days	**PBS (pH = 7.4)**		**Acid aqueous solution (pH = 4)**		**Basic aqueous solution (pH = 10)**	
	Size (nm)	Polydispersity index	Size (nm)	Polydispersity index	Size (nm)	Polydispersity index
Day 0	223,3±12,7	0,34±0,02	223,3±12,7	0,34±0,02	223,3±12,7	0,34 ± 0,02
Day 1	306,8 ± 4,8	0,21±0,01	239,8±4,9	0,29±0,03	331,1±7,4	0,47±0,01
Day 3	418,1 ± 6,9	0,29±0,03	313,8±3,1	0,37±0,01	357,5±30,0	0,44±0,04
Day 7	490,2 ± 49,5	0,52±0,02	568,6±6,7	0,40±0,01	993,5±186,4	0,74±0,09

Table 5.2. Stability test of MHNs suspension depending on Temperature (-20 °C and 4 °C).

Time	**Water at -20°C**			**Water at 4°C**		
	Size (nm)	Polydispersity index	ζ-potential (mV)	Size (nm)	Polydispersity index	ζ-potential (mV)
Day 0	223,3±12,7	0,34±0,02	-22,0±0,6	223,3±12,7	0,34±0,02	-22,0±0,6
Day 7	153,2±2,1	0,22±0,01	-20,0±0,3	239,8±4,9	0,29±0,03	-15,1±0,2

Preliminary *in vitro* evaluation was carried out to observe the cell behavior in presence of MHNs and to confirm the use of MHNs in nanomedicine applications. Fibroblast morphology was analyzed by phalloidin staining that visualized organization of the cytoskeletal actin filaments, essential proteins in maintaining and modulating cellular morphology and cell structural integrity. The preliminary results showed that the cell morphology are not negatively affect in presence of 100 µg/ml of MHNs (Figure 5.9). The cells showed their typical morphology well-spreaded on the well surfaces.

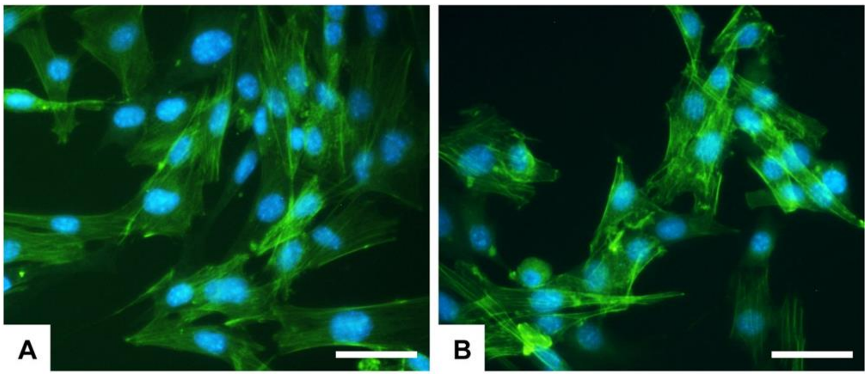

Figure 5.9. Analysis of cell morphology by phalloidin staining. Fibroblasts were spread with good morphology and firmly attached to the well plate with 100 µg/ml nanobeads (A) or without (B) after 3 days. Scale bars: 20 µm.

Furthermore, MTT test results demonstrated an increase in cell proliferation from day 1 to day 7 highlighting the absence of cytotoxicity due to the presence of MHNs in cell culture (Figure 5.10). Therefore, these preliminary findings make the new MHNs worthy of further investigation to select it as an excellent candidate in nanomedicine applications.

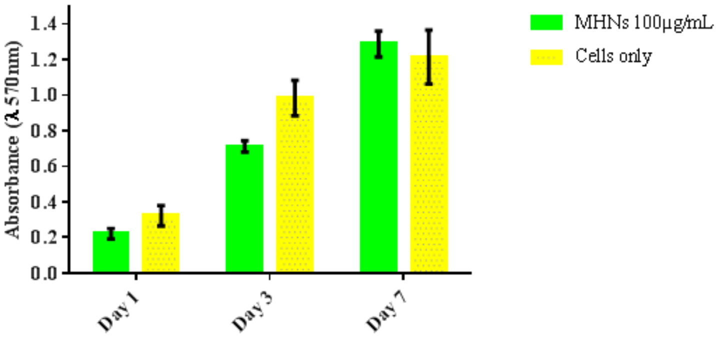

Figure 5.10. Analysis of cell proliferation by the MTT assay after 1, 3 and 7 days of fibroblasts cultured in presence with MHNs compared to cells alone (n =6). No statistically significant differences were seen between the two groups.

5.4. Conclusion

Hybrid nanobeads composed by superparamagnetic iron-doped apatite crystals nucleated on Alg matrix (MHNs) were successfully prepared by a bio-inspired assembling/mineralization process followed by an oil-in-water emulsion technique. The superparamagnetic ability and the good biocompatibility of the new nanobeads opens to possible uses in nanomedicine in replacement of currently used SPIONs, the use of which is affected by several concerns on their toxicity. Indeed, the degradation products of MHNs are limited to iron, calcium and phosphate ions. MHNs can be considered as building block materials with the aim to delivery drugs into the body guided by an external magnetic field or to be embedded into a scaffold for hard/soft tissue regeneration. The possibility of multiple uses is extended by the high-density of iron-doped nanoapatite on the MHNs surface, thus allowing to link several bioactive molecules for active targeting and therapeutic purposes. The promising properties of the new MHNs deserve further investigation in more clinically relevant environments to define more precisely their applicability in nanomedicine and theranostics.

REFERENCES

1. Stepanov, A. *et al.* Amphiphiles with polyethyleneoxide-polyethylenecarbonate chains for hydrophilic coating of iron oxide cores, loading by Gd(III) ions and tuning R2/R1 ratio. *React. Funct. Polym.* **99**, 107–113 (2016).

2. Cui, L. *et al.* Developing a hybrid emulsion polymerization system to synthesize Fe3O4/polystyrene latexes with narrow size distribution and high magnetite content. *J. Polym. Sci. Part A Polym. Chem.* **45**, 5285–5295 (2007).

3. Singh, N., Jenkins, G. J. S., Asadi, R. & Doak, S. H. Potential toxicity of superparamagnetic iron oxide nanoparticles (SPION). *Nano Rev.* **1**, 5358 (2010).

4. Liu, G., Gao, J., Ai, H. & Chen, X. Applications and potential toxicity of magnetic iron oxide nanoparticles. *Small* **9**, 1533–1545 (2013).

5. Tampieri, A. *et al.* Intrinsic magnetism and hyperthermia in bioactive Fe-doped hydroxyapatite. *Acta Biomater.* **8**, 843–851 (2012).

6. Panseri, S. *et al.* Intrinsically superparamagnetic Fe-hydroxyapatite nanoparticles positively influence osteoblast-like cell behaviour. *J. Nanobiotechnology* **10**, 32 (2012).

7. Nguyen, K. T. & Zhao, Y. Engineered Hybrid Nanoparticles for On-Demand Diagnostics and Therapeutics. *Acc. Chem. Res.* **48**, 3016–3025 (2015).

8. Iafisco, M. *et al.* Magnetic bioactive and biodegradable hollow fe-doped hydroxyapatite coated poly(l -lactic) acid micro-nanospheres. *Chem. Mater.* **25**, 2610–2617 (2013).

9. Minardi, S. *et al.* Multiscale patterning of a biomimetic scaffold integrated with composite microspheres. *Small* **10**, 3943–3953 (2014).

10. Mohammed, L. & Gomaa, D. R. and H. Bioactivity of Hybrid Polymeric Magnetic Nanoparticles and Their Applications in Drug Delivery. *Current Pharmaceutical Design* **22**, 3332–3352 (2016).

11. Daemi, H. & Barikani, M. Synthesis and characterization of calcium alginate

nanoparticles, sodium homopolymannuronate salt and its calcium nanoparticles. *Sci. Iran.* **19**, 2023–2028 (2012).

12. Zhao, D., Zhuo, R. X. & Cheng, S. X. Alginate modified nanostructured calcium carbonate with enhanced delivery efficiency for gene and drug delivery. *Mol. Biosyst.* **8**, 753–759 (2012).

13. De, S. & Robinson, D. P olymer relationships during preparation of chitosan – alginate and poly-l-lysine – alginate nanospheres. **89**, 101–112 (2003).

14. Tampieri, A. *et al.* HA/alginate hybrid composites prepared through bio-inspired nucleation. *Acta Biomater.* **1**, 343–351 (2005).

15. Feuser, P. E. *et al.* Encapsulation of magnetic nanoparticles in poly(methyl methacrylate) by miniemulsion and evaluation of hyperthermia in U87MG cells. *Eur. Polym. J.* **68**, 355–365 (2015).

16. Pongsawatmanit, R., Harnsilawat, T. & McClements, D. J. Influence of alginate, pH and ultrasound treatment on palm oil-in-water emulsions stabilized by β-lactoglobulin. *Colloids Surfaces A Physicochem. Eng. Asp.* **287**, 59–67 (2006).

17. Shimanovich, U., Bernardes, G. J. L., Knowles, T. P. J. & Cavaco-Paulo, A. Protein micro- and nano-capsules for biomedical applications. *Chem. Soc. Rev.* **43**, 1361–1371 (2014).

18. Tampieri, A. *et al.* Magnetic bioinspired hybrid nanostructured collagen-hydroxyapatite scaffolds supporting cell proliferation and tuning regenerative process. *ACS Appl. Mater. Interfaces* **6**, 15697–15707 (2014).

19. Tampieri, A. *et al.* Biologically inspired synthesis of bone-like composite: Self-assembled collagen fibers/hydroxyapatite nanocrystals. *J. Biomed. Mater. Res. - Part A* **67**, 618–625 (2003).

20. Mandal, S., Kumar, S. S., Krishnamoorthy, B. & Basu, S. K. Development and evaluation of calcium alginate beads prepared by sequential and simultaneous methods . *Brazilian J. Pharm. Sci. (Impresso); Vol 46, No 4 (2010)DO - 10.1590/S1984-82502010000400021* (2010).

21. Ma, X. & Ellis, D. E. Initial stages of hydration and Zn substitution/occupation on hydroxyapatite (0 0 0 1) surfaces. *Biomaterials* **29**, 257–265 (2008).

22. De, S. & Robinson, D. Polymer relationships during preparation of chitosan-alginate and poly-l-lysine-alginate nanospheres. *J. Control. Release* **89**, 101–112 (2003).

23. Sreeram, K. J., Yamini Shrivastava, H. & Nair, B. U. Studies on the nature of interaction of iron(III) with alginates. *Biochim. Biophys. Acta - Gen. Subj.* **1670**, 121–125 (2004).

24. Iafisco, M. *et al.* Superparamagnetic iron-doped nanocrystalline apatite as a delivery system for doxorubicin. *J. Mater. Chem. B* **4**, 57–70 (2016).

25. Panseri, S. *et al.* Modifying bone scaffold architecture in vivo with permanent magnets to facilitate fixation of magnetic scaffolds. *Bone* **56**, 432–439 (2013).

26. De Santis, R. *et al. Towards the Design of 3D Fiber-Deposited Poly(-caprolactone)/Iron-Doped Hydroxyapatite Nanocomposite Magnetic Scaffolds for Bone Regeneration*. *Journal of Biomedical Nanotechnology* **11**, (2015).

27. Luna-Pineda, T. Synthesis and characterization of alginate-based magnetic nanocomposite.

28. Ab Wab, H. A., Abdul Razak, K. & Zakaria, N. D. Properties of amorphous silica nanoparticles colloid drug delivery system synthesized using the micelle formation method. *J. Nanoparticle Res.* **16**, (2014).

29. Shen, J.-M. *et al.* Luminescent/Magnetic Hybrid Nanoparticles with Folate-Conjugated Peptide Composites for Tumor-Targeted Drug Delivery. *Bioconjug. Chem.* **23**, 1010–1021 (2012).

30. Almeida, J. P. M., Chen, A. L., Foster, A. & Drezek, R. In vivo biodistribution of nanoparticles. *Nanomedicine* **6**, 815–835 (2011).

6. Innovative bio-hybrid composites as booster for sunscreen formulations

6.1. Introduction

It is known that solar radiations, especially the ultraviolet (UV) component of the spectrum of these radiations, are responsible for photochemical degradation of various types such as fading and aging of paints, plastic coating as well as the alterations of the skin issues in humans, potentially up to the onset of skin cancer.[1] Acute and chronic exposure to UV rays can indeed lead to sunburn, photoaging, photoimmunosuppression and a photocarcinogenity, which are of great concern for young people and in particular children.[2] UV radiation comprises the portion of the spectrum of wavelengths between 100 and 400 nm divided into UVC (100-290 nm), UVB (290-320 nm) and UVA (320-400 nm). UVC radiation are absorbed by the ozone layer and do not reach the Earth's surface, while exposure to UVA and UVB is considered unavoidable. In order to prevent or mitigate the negative effects of UV ray exposure, sunscreens can be used. They are fluid compositions that can be spread on the part to be protected and which contain components able to reduce the amount of UV radiation that reaches the same part.[2,3] The use of sunscreens as protective barriers against skin damage and cancer, by absorbing harmful UVA and UVB rays, is becoming an increasingly important issue and sunscreen can be divided into two main classes: a) chemical filter where the active components are organic molecules capable of absorbing UV rays and physical or inorganic UV filters where particles are able to reflect radiation acting as physical barriers.[4,5] Among chemical filter ones of the most used are methozydibenzoylmethane butyl or avobenzone, while among inorganic filter is mentioned titanium dioxide (TiO_2) or zinc oxide (ZnO). TiO_2 is able to reflect, scatter and absorb UV radiation, thus preventing sunlight-related skin disorders such as sunburn and skin photodamage. However, TiO_2 is well known to generate reactive oxygen species (ROS) under photoexcitation, it has to be chemically modified when used in sunscreens.[2,6,7] Calcium phosphates (CaPs), especially hydroxyapatite (HA) have been deeply investigated for several applications in biomedical field and nanomedicine due to their high biomimicry and biocompatibility. An interesting feature of biomimetic HA is to incorporate some foreign ions in its lattice, indeed, in the past years, we developed a number of protocols for the incorporation of different kind of ions (e.g. Mg, Sr, CO3, and Fe (II, III)) and the achievement of multifunctional products for regenerative- and nano- medicine.[8,9] However, regarding sunscreens, unmodified HA does not absorb in the UV range, so it is necessary to modify its structure to obtain a UV-absorbing material, thus doping with appropriate elements may provide final compound with promising UV protection (Figure 6.1).[10,11]

In response to these needs, in this chapter, hybrid composites were synthetized in which the mineral phase, composed of titanium-doped and/or iron-doped hydroxyapatite (TiHA, FeTiHA) was nucleated on gelatin fibers (Gel) creating a biomimetic hybrid composite endowed with UV-reflectance properties and brownish color suitable in the development of sunscreen formulation where nanoparticles' size and conformation avoid any kind of whitening effect despite of low skin penetrating power.

Figure 6.1. possible uses of polymers mineralized with iron and/or titanium hydroxyapatite.

6.2. Synthesis process

Synthesis of titanium-doped hydroxyapatite biomineralized on gelatin (GelTiHA). Heterogeneous nucleation of TiHA nanocrystals on assembling gel matrix was achieved by means of neutralization reaction performed as follows. An acid solution was prepared mixing a gelatin solution (3.32 g of gel in 83 mL H_2O at 45 °C) with phosphate solution (3.46 g of H_3PO_4 in 30 mL). A solution of $Ti(iOPr)_4$ was prepared separately by mixing 2.20 g of the compound with 15 mL of isopropanol under Argon flux to avoid the oxidation of Ti^{4+}. Finally, a basic suspension was prepared in a three necks round-bottom flask dispersing 3.90 g of $Ca(OH)_2$ in 100 mL of H_2O at 45° under mechanical stirring for 30 minutes. The acid and titanium solution was transferred in two cylindrical dropping funnels and slowly are added dropwise to the basic suspension in order to finish in the same time (acid flux is faster than titanium flux) under vigorous mechanical agitation and keeping the reaction bath at 45°C. Pay attention that titanium drops go directly into basic solution and don’t touch the flask in order to avoid the oxidation of Ti^{4+}. A controlled temperature for 2 hours was kept after addition finished, and then was left without stirring and heating for 2 hours. Finally, the product was centrifuged at 6000 rpm for 10 minutes to pellet particles, washed three times and was freeze-dried. A controlled freeze-drying process was applied setting the precise cooling temperature (−40 °C) and heating ramp (2 °C min−1 up to −5 and 1 °C min−1 up to 25 °C) at p = 0.086 mbar to achieve dried powder.

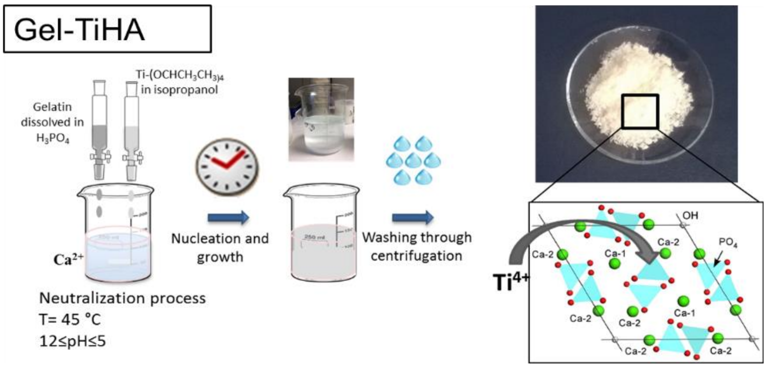

Figure 6.2. Synthesis of GelTiHA hybrid composite.

Synthesis of titanium-doped and iron-doped hydroxyapatite biomineralized on gelatin (GelFeTiHA). Heterogeneous nucleation of FeTiHA nanocrystals on assembling gel matrix was achieved by means of neutralization reaction performed as follows. An acid solution was prepared mixing a gelatin solution (5 g of gel in 125 mL H_2O at 45 °C) with phosphate solution (4.2 g of H_3PO_4 in 30 mL). A solution of $Ti(iOPr)_4$ was prepared separately by mixing 3.15 g of the compound with 15 mL of isopropanol under Argon flux to avoid the oxidation of Ti^{4+}. Finally, a basic suspension was prepared in a three necks round-bottom flask dispersing 4.72 g of $Ca(OH)_2$ in 100 mL of H_2O at 45° under mechanical stirring for 30 minutes. Two solution of iron precursor were prepared by dissolving 1.2 g of $FeCl_2·4H_2O$ and 1.65 g of $FeCl_3·6H_2O$ into 8 mL of H_2O for each, respectively. The two iron precursor solutions were poured into the calcium precursor solution in a simultaneously way. The acid and titanium solution was transferred in two cylindrical dropping funnels and slowly are added dropwise to the basic suspension in order to finish in the same time (acid flux is faster than titanium flux) under vigorous mechanical agitation and keeping the reaction bath at 45°C. Pay attention that titanium drops go directly into basic solution and don’t touch the flask in order to avoid the oxidation of Ti^{4+}. A controlled temperature for 2 hours was kept after addition finished, and then was left without stirring and heating for 2 hours. Finally, the product was centrifuged at 6000 rpm for 10 minutes to pellet particles, washed three times and was freeze-dried. A controlled freeze-drying process was applied setting the precise cooling temperature (−40 °C) and heating ramp (2 °C min−1 up to −5 and 1 °C min−1 up to 25 °C) at p = 0.086 mbar to achieve dried powder.

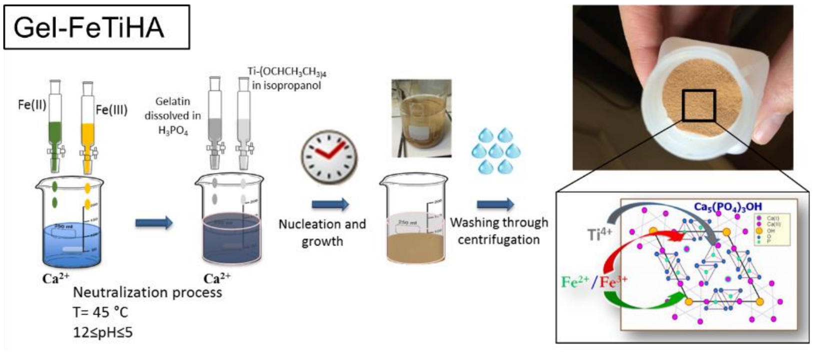

Figure 6.3. Synthesis of GelFeTiHA hybrid composite.

6.3. Results&Discussion

The dispersion of ions-doped HA nanoparticles in the matrix does not occur by mechanical mixing of previously formed HA nanoparticles in the organic matrix but rather through a biomineralization process in which the HA nanoparticles are nucleated directly within the matrix itself. In this process gelatin control the nucleation, orientation, crystallization and morphology of hydroxyapatite particles mainly playing a role of crystallization inhibitors. Furthermore, the partially substitution of calcium and phosphate ions with iron and titanium ions allowed to confer innovative properties to the apatitic phase, endowing with reflectance characteristic that make them suitable in cosmetic field especially as booster in sunscreen formulation. [10,12]

Thermogravimetric and ICP analyses determined the chemical composition and the composition in terms of % by weight of water, gelatin and mineral fraction. The water and gelatin contents were calculated by the weight losses that occur in the range 25-110 °C and 120-1000 °C, respectively, attributing the residual mass to the substituted HA (Figure 6.4).

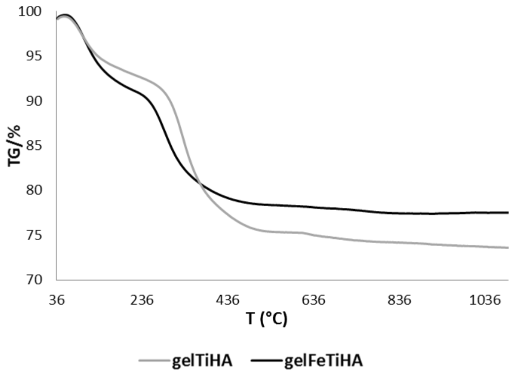

Figure 6.4. Thermal decomposition profile (TGA) of GelTiHA and GelFeTiHA

Regarding hydroxyapatite, the chemical composition was measured by ICP quantitative analyses in terms of molar ratio between the various elements (Table 6.1).

Table 6.1. gelatin, HA and water content and chemical composition of GelTiHA and GelFeTiHA evaluated by TGA and ICP respectively.

	GelTiHA	**GelFeTiHA**
HA	73.61 wt%	77.52 wt%
Gelatin	20.93 wt%	17.21 wt%
Water	2.16 wt%	2.50 wt%
Ca/P	1.90 ± 0.2	1.35 ± 0.1
Fe/Ca	/	0.21 ± 0.05
Ti/Ca	0.15 ± 0.03	0.21 ± 0.05
(Ca+Fe)/P	/	1.63 ± 0.05
Ca/(P+Ti)	1.48 ± 0.1	1.05 ± 0.03
Fe^{2+}/Fe^{3+}	/	1:1

The values of water amounts were very similar in both samples. The amount of gelatin and HA instead showed greater variation in the different samples. In general, all the samples show a very different Ca/P atomic ratio value from pure HA (theoretical ratio 1.67): the value of this ratio are lower than the theoretical in GelFeTiHA while that of the GelTiHA sample is significantly higher than theoretical.[13,14] Ti/Ca ratio in GelTiHA is in accordance with the amount of titanium nominally introduced during its preparation. In the GelFeTiHA sample the Ti/Ca ratio is greater than that of the GelTiHA sample and even higher than that derivable from the nominal amount of titanium introduced during synthesis. Moreover, a very low Ca/(P+Ti) ratio was measured this can be attributed to the substitution of Ca with Fe ions as confirmed by (Ca+Fe)/P, a value close to that of stoichiometric HA.[11,15] These data suggest the presence of a secondary phase of TiO_2. Finally, the Fe^{2+}/Fe^{3+} ratio for GelFeTiHA is in complete accordance with the amounts of the two ions nominally introduced during synthesis.

XRD profiles showed the presence of a crystalline phase that can be identified as HA as literature data reported (Figure 6.5A). No secondary crystalline phase is identified. On the basis of this observation, it can be concluded that the TiO_2 phase, whose presence is inferred from the chemical analysis is amorphous. However, gelatin is not visible to XRD due to its amorphous nature. All XRD patterns are poorly resolved with low intensity especially in the case of GelFeTiHA, these characteristic meanings a low degree of crystallinity of material. This low crystallinity may be ascribed to various factors. Firstly, the low biomineralization temperature does not allow an atomic rearrangement in favor of more crystalline structures, which are thermodynamically more stable. A second factor is the presence of gelatin. The amorphous organic polymer can direct the mineralization process towards low crystallinity phases as is known in the field. Finally, the presence of iron and/or titanium ions during biomineralization, in which the crystal lattice is formed, has the effect of distorting the lattice itself, thus leading to an increase in disorderly areas and causing the formation of poorly crystalline HA.

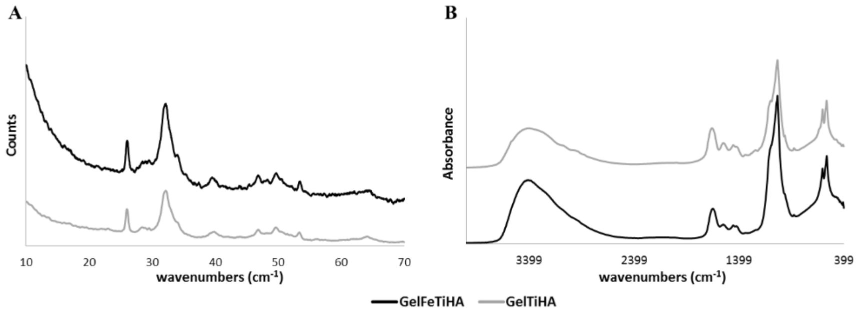

Figure 6.5. A)XRD spectra and B)FTIR spectra of GelFeTiHA and GelTiHA hybrid composites.

FTIR analysis of GelTiHA and GelFeTiHA revealed a similar pattern (Figure 6.5B) showing peaks at 3405, 1650, 1547, 1453, 1036, 602, 562 cm^{-1}. The peak at 3405 cm^{-1} corresponds to the stretching vibrations of O-H bonds of both FeHA and Gel, while the peaks at 1650, 1547 and 1453 cm^{-1}, are related to the asymmetric and symmetric stretching vibrations of the carboxylate groups in Gel. The signal at 1036 cm^{-1} corresponds to the asymmetric stretching of PO_4 groups of HA. Finally, the peak at 602 and 562 cm^{-1} is related to the bending of the PO_4 group of the HA.[16]

The morphology of the samples, analyzed using a scanning electron microscope, was shown in Figure 6.6. GelTiHA sample consists of particles with similar dimensions in the three spatial directions, of between about 100 and 200 nm. Furthermore, also GelFeTiHA reveals a morphology and dimension very close to GelTiHA.

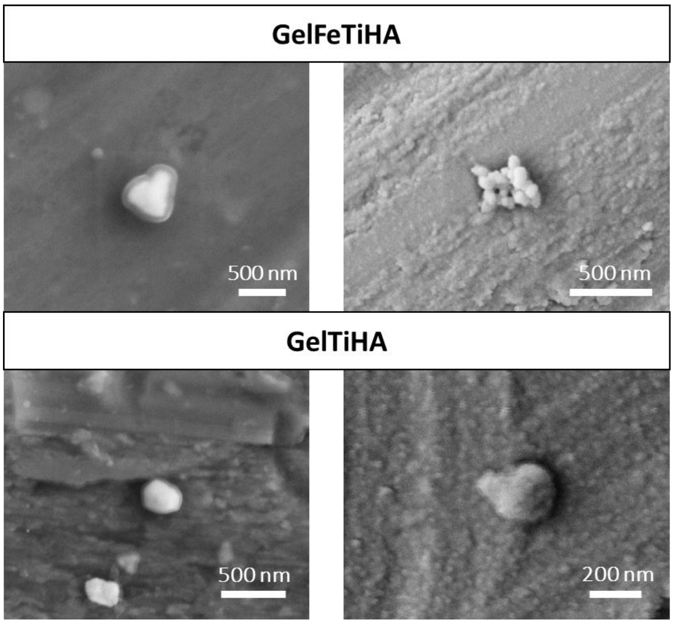

Figure 6.6. SEM-FEG images of GelFeTiHA and GelTiHA hybrid composites. Scale bar at 500 nm and 200 nm.

Hydrodynamic diameter (Hd) values recorded by light diffraction are much higher than those measured by SEM analysis. These values are hundreds of nanometers for each sample, GelTiHA values is slighter higher than GelFeTiHA. The difference between DLS and SEM is due to the fact that for SEM analysis the samples were suspended in ethanol and dried by means of an infrared lamp on alumina matrix, while for the DLS analysis it was necessary to prepare a suspension. In this way, DLS provides additional information on the behavior of hibrid composite in water revealing the size of the particles in the aqueos medium. As it is well known in literature, nano-sized particles tend to clump together when they are suspended in aqueous media, so the values obtained from DLS do not relate to single particles but to aggregates thereof. However, SEM determines the size of the single dry particles.[11,15]

Table 6.2. particles size average and polidispersity index of GelFeTiHA and GelTiHA

Samples	d (nm)	PDI
Gel/FeTiHA	421,9 ± 19,39 nm	0,105 ± 0,058
Gel/TiHA	531,3 ± 7,858 nm	0,167 ± 0,051

The UV-Vis absorption and reflection properties of the hibrid composites was riported in figure X. the reflectance profiles of both composites were very different between them, GelTiHA revealed an area of average reflectance between 280 and 320 nm followed by a rapid increase up to reach the maximum reflectance (90%) at about 350 nm (in the range of UVB), after this peak the reflectance decreases slowly but never drops below values of about 65 % (at 800 nm). However, GelFeTiHA showed a low reflectance capacity (about 20%) at low wavelenghts followed by a gradual increase up to reach 60% of the light reflected around 650 nm wavelength. The behaviour changed measuring the absorbancve of hybrid composites, GelFeTiHA revealed a maximum value recorded at 280 nm, followed by an inflection point at about 360 nm and then a rapis decrease up to about 400 nm, after which values remains costant throughout the visible field. On the other hand, GelTiHA, across the entire measuring range, shows low level of absorption, with a profile that decreses in almost linear manner with increasing wavelength. In conclusion, GelTiHA has excellent reflectance properties in the UVA range and can reflect the radiation also in UVB range. GelFeTiHA instead have a good absorption properties in the UVB range. These properties make GelTiHA a physical filter, efficient for sunscreen composition, while GelFeTiHA can be used in combination with the first one to extend and increase the range of protection and the protective efficacy of solar filters in the UVB range.[10,17]

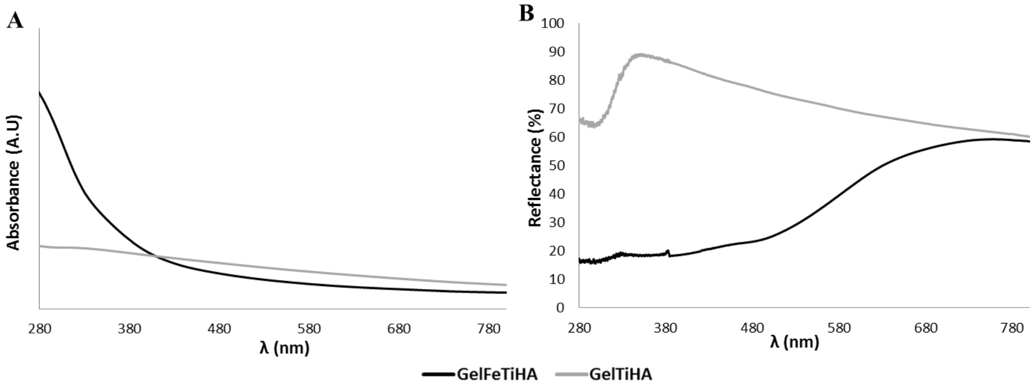

Figure 6.7. A) Absorption and B) reflectance spectra of GelFeTiHA and GelTiHA hybrid composites.

Finally, the photodegradation test carried out in presence of Rhodamine demonstrated that both samples not show photocatalytic effect avoiding the formation of radicals and/or reactive species under irradiation and highlighting their potentiality for innovation in sunscreens (Figure 6.8).[2,18]

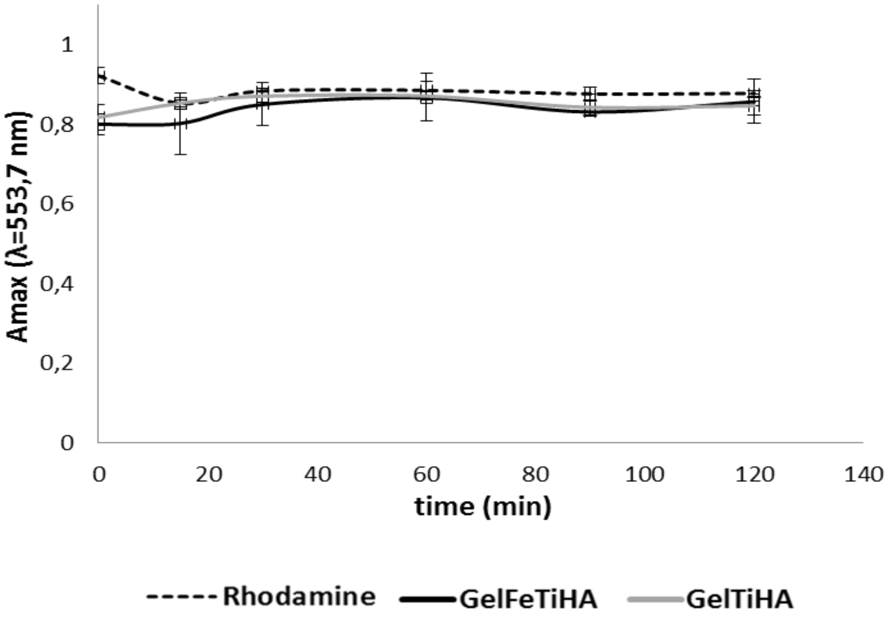

Figure 6.8. Photodegradation of GelFeTiHA and GelTiHA carried out using Rhodamine as control.

6.4. Conclusion

Hybrid composites developed had such features as to allow the development of new safe solar filters, because alongside its high biocompatibility compared to ZnO and TiO_2, its band of absorption/reflection of the UV radiation can be extended and modulated in the desired range by introducing suitable dopant ions in its crystalline structure. Moreover, the matrix must of course be harmless to the surface to be protected and in the case of the skin, it must be non-toxic and ensure physiological pH values in the finished product. Finally, the HA particles are of nanometric size, whereby they obviate the whitening effect problem. Moreover, being in close structural relation with the organic matrix and therefore part of larger composite particles, they also have a low skin penetrating power.

REFERENCES

1. Stavros, V. G. Photochemistry: A bright future for sunscreens. *Nat. Chem.* **6**, 955–956 (2014).

2. Serpone, N., Dondi, D. & Albini, A. Inorganic and organic UV filters: Their role and efficacy in sunscreens and suncare products. *Inorganica Chim. Acta* **360**, 794–802 (2007).

3. Katz, D. A. SUNSCREENS : PREPARATION AND. (2005).

4. Gasparro, F. P., Mitchnick, M. & Nash, J. F. A Review of Sunscreen Safety and Efficacy. *Photochem. Photobiol.* **68**, 243–256 (1998).

5. Shen, B., Scaiano, J. C. & English, A. M. Zeolite Encapsulation Decreases TiO2-photosensitized ROS Generation in Cultured Human Skin Fibroblasts†. *Photochem. Photobiol.* **82**, 5 (2006).

6. Tan, M. H., Commens, C. A., Burnett, L. & Snitch, P. J. A pilot study on the percutaneous absorption of microfine titanium dioxide from sunscreens. *Australas. J. Dermatol.* **37**, 185–187 (1996).

7. Shao, Y. & Schlossman, D. Effect of Particle Size on Performance of Physical Sunscreen Formulas. 1–9 (1999).

8. Landi, E. *et al.* Biomimetic Mg- and Mg,CO3-substituted hydroxyapatites: synthesis characterization and in vitro behaviour. *J. Eur. Ceram. Soc.* **26**, 2593–2601 (2006).

9. Landi, E. *et al.* Sr-substituted hydroxyapatites for osteoporotic bone replacement. *Acta Biomater.* **3**, 961–969 (2007).

10. Piccirillo, C. *et al.* A hydroxyapatite-Fe2O3based material of natural origin as an active sunscreen filter. *J. Mater. Chem. B* **2**, 5999–6009 (2014).

11. Adamiano, A. *et al.* Biomineralization of a titanium-modified hydroxyapatite semiconductor on conductive wool fibers. *J. Mater. Chem. B* **5**, 7608–7621 (2017).

12. Sojka, M. F. *et al.* UV protection afforded by gel-trapped TiO2particles.

Photochem. Photobiol. Sci. **10**, 1146–1151 (2011).

13. Tampieri, A. *et al.* Biologically inspired synthesis of bone-like composite: Self-assembled collagen fibers/hydroxyapatite nanocrystals. *J. Biomed. Mater. Res. - Part A* **67**, 618–625 (2003).

14. Tampieri, A. *et al.* Design of graded biomimetic osteochondral composite scaffolds. *Biomaterials* **29**, 3539–3546 (2008).

15. Tampieri, A. *et al.* Intrinsic magnetism and hyperthermia in bioactive Fe-doped hydroxyapatite. *Acta Biomater.* **8**, 843–851 (2012).

16. Krishnakumar, G. S. *et al.* Ribose mediated crosslinking of collagen-hydroxyapatite hybrid scaffolds for bone tissue regeneration using biomimetic strategies. *Mater. Sci. Eng. C* **77**, 594–605 (2017).

17. Smaoui, S., Ben Hlima, H., Ben Chobba, I. & Kadri, A. Development and stability studies of sunscreen cream formulations containing three photo-protective filters. *Arab. J. Chem.* **10**, S1216–S1222 (2017).

18. De Araujo, T. S., De Souza, S. O. & De Sousa, E. M. B. Effect of Zn2+, Fe3+and Cr3+addition to hydroxyapatite for its application as an active constituent of sunscreens. *J. Phys. Conf. Ser.* **249**, (2010).

7. Conclusions and Future Perspectives

The need of new generation of biomaterials with several applications and capable of interact with cells in an active way has been a major driving force in the regenerative medicine. In particular, a macro and nano-environment have to be recreated to stimulate the biochemical and biophysical signals of extracellular matrix (ECM). In this PhD work, new materials have been synthesized exploiting a biomimetic mineralization of different biopolymers such as gelatin and cellulose nanofibers with a subsequent freeze-drying. Biomimetic protocol previously studied using collagen as organic matrix of the mineralization has been successfully adapted although the 3D architecture was not preserved. Since biopolymers selected do not self-assemble into big microfibers and they are featured by lower density of charged amino acids groups respect to natural collagen, increasing the mineral contents (50-70 wt.%) it will be obtained only a powdered samples or a brittle and heterogeneous scaffolds. For this reason, a blending process was exploited to create a 3D bio-hybrid scaffolds. In this PhD project, biomineralization process was studied to generate different biomimetic-like composite ranging from composites for tissue regeneration, to composites for drug delivery systems and cosmetics. Natural polymers such as alginate, gelatin, cellulose nanofibers and chitosan were used as they could be highly biocompatible due to their natural origin and they could easily undergo physicochemical modifications. However, biopolymers display a rapid biodegradation in physiological conditions and low mechanical properties. For this reason, a proper cross-linking to stabilize and reinforce is highly requested. It is very difficult to identify which cross-linkers present on the market is featured by mechanical properties together with the ability to physically stabilize the material without observing cytotoxic effects. For this reason, different cross-linking agents and techniques such as genipin, hexamethylenediamine and dehydrothermal treatment, were chosen in order to modulate degradation rate and mechanical properties obtaining custom-made materials. Finally, during this PhD project a broad spectrum of possible applications of these kind of composites has been studied. This highlighted how such biomimetic materials composed of hydroxyapatite and biopolymers can be used in different fields thanks to their multifunctional ability. In addition to tissue engineering, where biomimetic materials allow cell stimulation, promoting regenerative process by acting like a 3D support other fields can be explored due to the versatility of hydroxyapatite (HA) that modifies its characteristic depending on the foreign ions included in its structure. In particular, including iron ions in a specific ratio, superparamagnetic properties have been observed (FeHA). The capacity of FeHA to be drug-loaded and, by applying an external magnetic field, guided to the desired site with subsequent local release of the drug via, for instance, magneto-shaking, makes FeHA a promising candidate for the development of drug delivery systems. In particular, in this PhD thesis, FeHA was nucleated on alginate fibres in order to create a following nanobeads system (MHNs) where drug can be entrapped inside, minimizing its side-effects and FeHA, exposed on the fibres surface, to promote the local drug release. Furthermore, together with iron ions, also titanium ions were included into HA lattice and the mineral phase was nucleated on gelatin fibers (GelFeTiHA and GelTiHA) in order to obtain a UV-reflecting material useful in cosmetic field as active component in sunscreen. The resulting materials are biodegradable, biocompatible, but especially the photocatalytic effect was not detected, meaning that samples do not form radicals and/or reactive species.

In conclusion, these results can also represent a proof of concept for further development of innovative materials obtained by biologically-inspired self-assembling processes and exploting cross-linking, blending and freeze-drying processes.

8. List of publications

1. Dellaquila A, Greco G, Campodoni E, Mazzocchi M, Mazzolai B, Tampieri A, Pugno NM, Sandri M. (2018) *Biomineralization of spider silk for the development of a high-performing hybrid biomaterial for bone tissue engineering application.* Submitted to Acta Biomaterialia.
2. Dellaquila A, Campodoni E, Tampieri A, Sandri M. (2018) *Investigation of hybrid Hydroxyapatite/Collagen scaffolds for osteochondral regeneration by factorial design.* Submitted to Current Applied Physics.
3. Sprio S, Campodoni E, Sandri M, Preti L, Keppler T, Mueller F, Pugno N, Tampieri A. (2018) *Graded multifunctional hybrid scaffold with superparamagnetic ability for periodontal regeneration.* Submitted to International Journal of Molecular Sciences.
4. Dozio SM, Montesi M, Campodoni E, Sandri M, Piattelli A, Tampieri A, Panseri S. (2018) *3D in vitro dentin-like model versus traditional 2D culture: a biomimetic scaffold for human Dental Pulp Stem cells culture*. Submitted to International Journal of Molecular Sciences.
5. Campodoni E, Dozio SM, Panseri S, Montesi M, Tampieri A, Sandri M. (2018) *Bio-hybrid matrix-based aligned 3D porous dentin-like scaffold*. In preparation.
6. Bortolomai I, Sandri M, Draghici E, Fontana E, Campodoni E, Marcovecchio GE, Ferrua F, Perani L, Spinelli A, Canu T, Di Tomaso T, Sergi Sergi L, Esposito A, Lombardo A, Naldini L, Tampieri A, Hollander GA, Villa A and Bosticardo M. (2018) *Novel strategy for thymus regeneration using 3d collagen type i scaffolds and gene modification*. Submitted to Biomaterials.
7. Rashad A, Syverud K, Campodoni E, Suliman S, Mustafa K, Mustafa M, Sandri M, Pedersen T. (2018) *Inflammatory Responses and Host Tissue Reactions to Wood-Based Nanocellulose*. Submitted to Materials science and Engineering: C.
8. Campodoni E, Heggset EB, Elsabahy R.S.M A, Ramírez-Rodríguez GB, Mustafa B.E. K, Syverud K, Tampieri A, Sandri M. (2018) *Polymeric 3D scaffolds for tissue regeneration: evaluation of biopolymer nanocomposite reinforced with cellulose nanofibrils.* Material science and Engineering: C; 10.1016/j.msec.2018.10.026
9. Menale C, Campodoni E, Palagano E, Mantero S, Erreni M, Inforzato A, Fontana E, Schena F, Van't Hof R, Sandri M, Tampieri A, Villa A, Sobacchi C. (2018)

MSC-seeded biomimetic scaffolds as factory of soluble RANKL in Rankl-deficient osteopetrosis. STEM CELLS Translational Medicine. 10.1002/sctm.18-0085

10. Campodoni E, Patricio T, Montesi M, Tampieri A, Sandri M, Sprio S (2018). *Biomineralization process generating hybrid nano and micro-carriers*. Core-Shell Nanostructures for Drug Delivery and Theranostics, (pp 19-42). Woodhead Publishing.
11. Krishnakumar G S, Gostynska N, Dapporto M, Campodoni E, Montesi M, Panseri S, Tampieri A, Kon E, Marcacci M, Sprio S, Sandri M. (2017). *Evaluation of different crosslinking agents on hybrid biomimetic collagen-hydroxyapatite composites for regenerative medicine.* International Journal of Biological Macromolecules.
12. Gostynska N, Krishnakumar G S, Campodoni E, Panseri S, Montesi M, Sprio S, Kon E, Marcacci M, Tampieri A, Sandri M. (2017). *3D porous collagen scaffolds reinforced by glycation with ribose for tissue engineering application.* Biomedical Material 2017 Jun 2. doi: 10.1088/1748-605X/aa7694.
13. Krishnakumar G S, Gostynska N, Campodoni E, Dapporto M, Montesi M, Panseri S, Tampieri A, Kon E, Marcacci M, Sprio S, Sandri M. (2017). *Ribose mediated crosslinking of collagen-hydroxyapatite hybrid scaffolds for bone tissue regeneration using biomimetic strategies;* Materials Science and Engineering: C, 77, 594–605.
14. Sprio S, Sandri M, Iafisco M, Panseri S, Adamiano A, Montesi M, Campodoni E, Tampieri A. (2016). *Bio-inspired assembling/mineralization process as a flexible approach to develop new smart scaffolds for the regeneration of complex anatomical region;* Journal of the European Ceramic Society, *36*(12), 2857-2867.
15. Campodoni E, Adamiano A, Dozio S. M, Panseri S, Montesi M, Sprio S, Tampieri A, Sandri M. (2016). *Development of innovative hybrid and intrinsically magnetic nanobeads as a drug delivery system*. Nanomedicine, 11(16), 2119-2130.

9. Scientific contributions to congresses and school

1. Campodoni E, Dozio Sm, Heggset EB, Dellaquila A, Panseri S, Syverud K, Tampieri A, Sandri M. *Hybrid polymer composite made from gelatin and cellulose nanofibrils: a nanobiomaterial with tunable degradability and mechanical performances.* ESB – 28th European Conference on Biomaterials, Maastricht, The Netherlands, 2018.
2. Campodoni E, Adamiano A, Tampieri A, Sandri M *The role of Ti and Fe ions in the hydroxyapatite; can improve its ability as physical filter in sunscreen formulation?".* International School of Crystallization, ISC Granada, Spain, 2018.
3. Montesi M, Panseri S, Campodoni E, Sandri M, Tampieri A. *Focus on Bone Cancer Model Via Biomimetic Materials.* TERMIS-WC, Kyoto, Japan, 2018.
4. Campodoni E, Tampieri A, Sandri M. *Ti and Fe doped hydroxyapatite: novel biomimetic UV-filter for sunscreen formulation.* Materials.it 2018, Bologna, Italy, 2018.
5. Montesi M, Panseri S, Campodoni E, Sandri M, Tampieri A, *Focus on Bone Cancer Model Via Biomimetic Materials*. Materials.it 2018, Bologna, Italy, 2018.
6. Campodoni E, Dozio SM, Panseri S, Montesi M, Tampieri A, Sandri M. *Bio-hybrid matrix-based aligned 3D porous dentin-like scaffold.* Bioceramics29, Toulouse, France, 2017.
7. Sandri M, Campodoni E, Adamiano A, Panseri S, Montesi M, Sprio S, Tampieri A. *Hybrid magnetic nanocomposite supporting cell proliferation and tuning regenerative process*. Bioceramics29, Toulouse, France, 2017.
8. Campodoni E, Dozio SM, Panseri S, Montesi M, Tampieri A, Sandri M. *Bio-hybrid matrix-based aligned 3D porous dentin-like scaffold.* ESB - 27th European Conference on Biomaterials, Athens (Greece), 2017.
9. Campodoni E, Adamiano A, Dozio SM, Panseri S, Montesi M, Sprio S, Tampieri A, Sandri M.*Innovative hybrid and intrinsically magnetic nanobeads as drug delivery system.* SIB, Milano, Italy, 2017
10. Dellaquila A, Campodoni E, Sandri M, Pugno N, Tampieri A. *Mineralizing Spider Network: A New Promising Hybrid Biomaterial.* Conferenza di dipartimento CNR, Alghero, Italia, 2017.
11. Campodoni E, Ramìrez-Rodriguez GB, Elsabahy ARSM, Heggset EB, Mustafa K, Syverud K, Tampieri A, Sandri M. *Gelatin/Nanocellulose Polymeric Blends to Develop 3D Scaffolds for Tissue Regeneration*. SIB, Ischia, Italy, 2016.

12. Campodoni E, Dozio Sm, Heggset EB, Panseri S, Syverud K, Tampieri A, Sandri M. *Polymeric blend of gelatin and cellulose nanofibrils: a nanobiomaterial with controlled mechanical performances and degradability*. Materials.it 2016, Catania, Italy, 2016.
13. Campodoni E, Dozio SM, Panseri S, Montesi M, Tampieri A and Sandri M. *3D Porous Scaffolds with Oriented Microtubules designed for Dental Regeneration*. Biomineralization Gordon Conference, Girona, Spain, 2016.
14. Campodoni E, Ramìrez-Rodriguez GB, Elsabahy ARSM, Heggset EB, Mustafa K, Syverud K, Tampieri A, Sandri M. *Gelatin/Nanocellulose Polymeric Blends to Develop 3D Scaffolds for Tissue Regeneration*. National Young Researchers' Forum on Material Science and Technology, Ischia, Italy, 2016
15. Campodoni E, Adamiano A, Sandri M, Tampieri A. *Development of Innovative Hybrid Magnetic Nanobeads as Drug Delivery System.* International Conference on Nanotechnology in Medicine, Manchester UK, 2015.
16. Sandri M, Campodoni E, Adamiano A, Panseri S, Montesi M, Sprio S, Tampieri A. *Biomineralized magnetic hybrid nanocomposite supporting cell proliferation and tuning regenerative process.* Materials.it 2016, Catania, Italy, 2016.
17. Sandri M, Campodoni E, Sprio S, Vazquez B, Monticelli P, Tampieri A. *Biopolymeric porous material: Nature inspires a new generation of Heat and Moisture exchange device for medical applications.* NICE - 3rd International Conference on Bioinspired and Biobased Chemistry and Materials that is held in Nice, France, 2016.
18. Dozio SM, Panseri S, Montesi M, Campodoni E, Sandri M, Tampieri A. *3D cell cultures in porous scaffolds with oriented microtubules designed for dental regeneration*. TERMIS-EU Conference, Uppsala, Sweden. 2016.
19. Panseri S, Montesi M, Dozio SM, Campodoni E, Sandri M, Peruzzotti-Jametti L, Pluchino S, Tampieri A. *Collagen-based scaffold as a new tool for 3D neural stem cell culture.* TERMIS-EU Conference, Uppsala, Sweden. 2016.
20. Dozio SM, Panseri S, Montesi M, Campodoni E, Sandri M, Tampieri. *3D Cell Cultures in Porous Scaffolds with Oriented Microtubules Designed for Dental Regeneration.* Nanomedicine Conference, Viterbo, Italy, 2016.